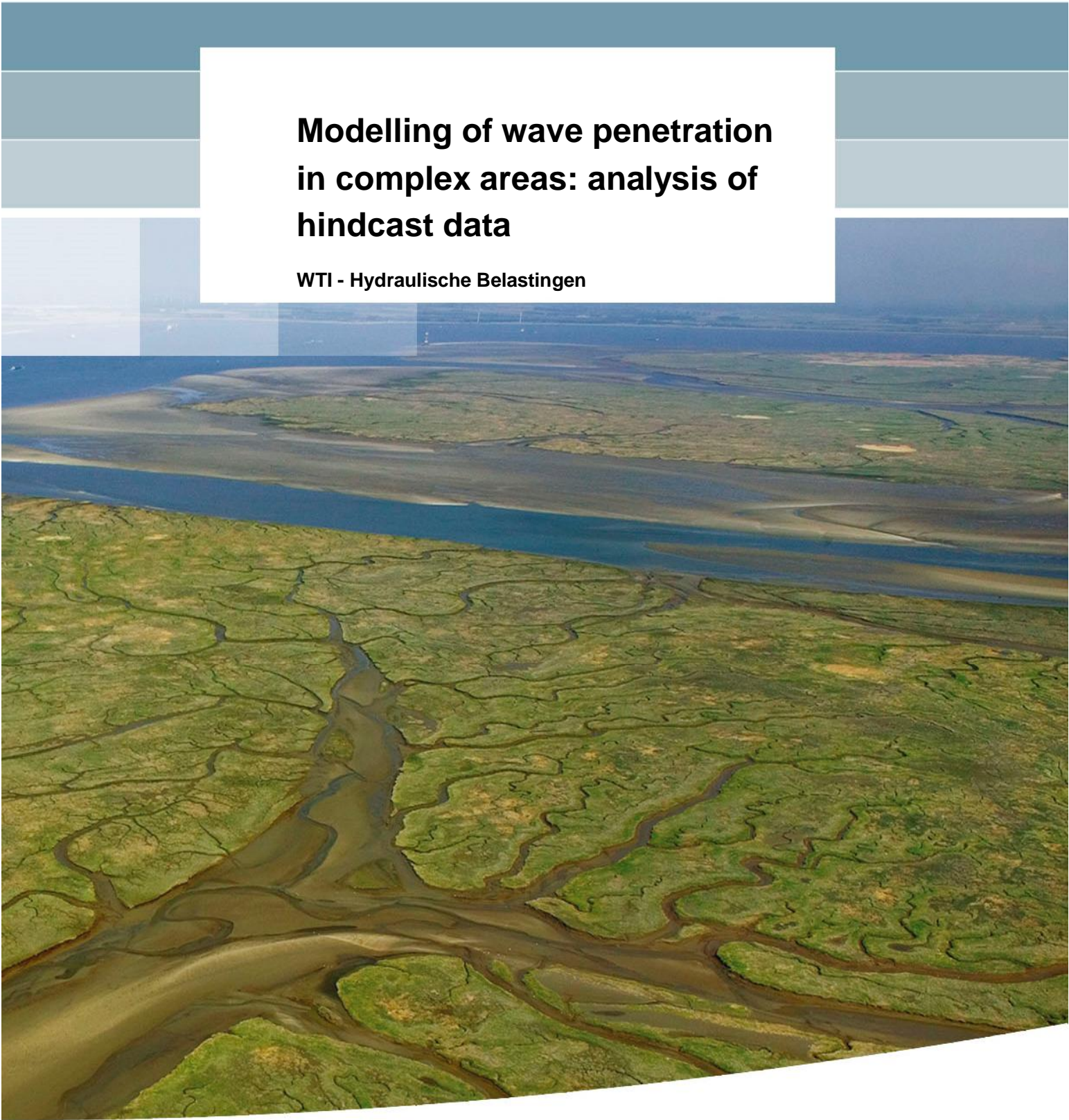# Modelling of wave penetration in complex areas: analysis of hindcast data

WTI - Hydraulische Belastingen

Deltares

Modelling of wave penetration in complex areas: analysis of hindcast data

WTI - Hydraulische Belastingen

Joana van Nieuwkoop
Jacco Groeneweg

1209433-007

Deltares

Title
Modelling of wave penetration in complex areas: analysis of hindcast data

Client	Project	Reference	Pages
Rijkswaterstaat – WVL	1209433-007	1209433-007-HYE-0006	66

Keywords
Wave penetration, wave modelling, Wadden Sea, Western Scheldt, SWAN, nonlinear wave interactions

Summary
For the WTI calculations of the Hydraulic Boundary Conditions, which are to be finalized by the end of 2015 and established by the Minister in 2017, wave statistics obtained at deeper water buoys need to be transformed to the toe of the dike using the wave action model SWAN. This transformation is particularly challenging in complex tidal inlet systems such as the Wadden Sea and the Western Scheldt in the Netherlands. Although significant model improvements – particularly in the propagation and bottom friction dissipation - have been made, one of the unresolved issues is that the penetration of North Sea waves into the tidal inlets is still underestimated by SWAN.

Previous studies showed that two-dimensional nonlinear interactions (and especially the sub-harmonic interactions) play a major role in the transmission of energy from flats into channels, and that this process may explain SWAN's under-prediction of wave energy penetration into a complex tidal inlet system. With this mechanism in mind, it was examined in this study under which conditions SWAN underestimates the wave energy when propagating into complex tidal inlet systems.

For this purpose, various existing hindcasts have been reanalysed; 30 hindcast moments in the Western Scheldt, 26 hindcast moments for the Amelander Zeegat and 11 hindcast moments for the Eastern Wadden Sea. Besides the 1.5D wave energy density spectra and spatial distributions of wave directions and water depth, use was made of observed 2D wave energy density spectra and radar information.

It was concluded that a mismatch between measured and computed swell energy is often already observed in the tidal inlet. Whether or not the low-frequency wave energy is underestimated by SWAN is to a large extent determined by the local geometry, such as the position and characteristics of channels and flats. For all three areas, some of the differences could be explained by the theory of the nonlinear interactions. In those cases the waves first propagated over the ebb-tidal delta or tidal flats and subsequently came across a channel. From the 2D spectra it was seen that the observed waves could enter or cross the channel, whereas the computed waves were refractively trapped to the channel edges.

The incident wave direction and the water level affect the strength of nonlinear wave interactions that result in directional broadening of the energy density spectrum, and therefore influence the amount of wave energy penetrating from tidal flats into and across tidal channels, and eventually towards the dike of the estuaries. However, not all cases where the low-frequency wave energy is underestimated by SWAN can be explained by the theory of nonlinear interactions; many other factors (that have not been investigated in this study) may influence the reliability of the SWAN results.

It is therefore impossible to define a generic concept to correct the SWAN results for the observed underestimation of low-frequency wave energy. The best way to deal with this problem at this moment is to indicate certain areas where the SWAN data are suspicious. At the coast of Zeeuws-Vlaanderen, the headland of the Wadden Sea islands and in front of the dikes in the Eems-Dollard estuary the SWAN results for the more energetic conditions, i.e. strong winds from the north-west to northern sector should be treated with care.

Deltares

Version	Date	Author	Initials	Review	Initials	Approval	Initials
1	Nov. 2014	Joana van Nieuwkoop Jacco Groeneweg		Ap van Dongeren		Marcel van Gent	
2	Dec. 2014	Joana van Nieuwkoop Jacco Groeneweg	JvN	Ap van Dongeren	AvD	Marcel van Gent	

State
final

Contents

Deltares

Samenvatting (summary in Dutch)

Als onderdeel van het Wettelijk Toetsinstrumentarium 2017 (WTI2017) worden Hydraulische Randvoorwaarden (HR) berekend. Deze zullen aan het einde van 2015 beschikbaar zijn en naar verwachting in 2017 door de Minister worden vastgesteld. De HR bestaat uit een combinatie van waterstanden en golfcondities onder maatgevende omstandigheden. Om de maatgevende golfcondities te bepalen wordt de golfstatistiek op dieper water vertaald naar de teen van de dijk met het golfmodel SWAN. Deze vertaling is vooral in complexe watersystemen als de Waddenzee en de Westerschelde uitdagend. In de afgelopen jaren zijn er vele modelverbeteringen in SWAN doorgevoerd, vooral op het gebied van voortplanting, bodemwrijving en diepte-geïnduceerd breken. Uit de diverse hindcasts is gebleken dat SWAN echter de doordringing van Noordzee golven (frequentiebereik van 0.03 Hz en 0.20 Hz) in de estuaria en zeegaten onderschat. Vooralsnog is dit probleem niet opgelost.

Voorgaande studies toonden aan dat 2D niet-lineaire wisselwerkingen (en in het bijzonder de subharmonische interacties) een belangrijke rol spelen in de transmissie van energie van de ondiepe platen naar de diepe geulen. Dit 2D mechanisme zou de onderschatting van laag-frequente energie in complexe getijdebekkens en estuaria kunnen verklaren. Met het bovenstaande mechanisme in het achterhoofd is in deze studie onderzocht voor welke situaties de golfenergie in SWAN onderschat wordt, wanneer golven zich in complexe getijdebekkens en estuaria voortplanten.

Met dit doeleinde zijn verschillende bestaande hindcast studies opnieuw geanalyseerd. Het gaat om 30 hindcast momenten in de Westerschelde, 26 hindcast momenten in het Amelander Zeegat en 11 hindcast momenten in de Oostelijke Waddenzee. Hierbij is niet alleen gebruik gemaakt van 1.5D golfspectra en ruimtelijke velden van golfrichting en water diepte, maar ook van 2D golfspectra en radar informatie.

Uit de analyse volgt dat de verschillen tussen gemeten en berekende laag-frequente energie vaak al te zien zijn in de buitendelta van een getijdebekken of estuarium. Hierbij speelt de lokale geometrie, zoals de ligging en vorm van platen en geulen, een belangrijke rol. In alle drie de onderzochte gebieden konden sommige verschillen tussen de gemeten en berekende golfhoogtes verklaard worden aan de hand van de hypothese van niet-lineaire wisselwerkingen. Uit de 2D golfspectra kon worden afgeleid dat de gemeten golven in sommige gevallen wel tot de geul kunnen doordringen, terwijl de berekende golven door refractie op de geulwand blijven hangen.

De hoek van golfinval en de waterstand kunnen de sterkte van de niet-lineaire wisselwerkingen (resulterend in verbreding van de richtingsruimte van het spectrum) bepalen en hebben daardoor invloed op de doordringing van golfenergie van platen naar geulen en uiteindelijk naar de dijken binnenin het zeegat of estuarium. Echter, niet alle gevallen waarbij de laag-frequente energie wordt onderschat, kunnen worden verklaard met de hypothese van de niet-lineaire wisselwerkingen. Tal van andere aspecten, die niet verder onderzocht zijn in deze studie, hebben invloed op de betrouwbaarheid van de SWAN resultaten.

Het is daarom onmogelijk om een generieke conclusie te trekken ten aanzien van de modelfout van SWAN met betrekking tot de onderschatting van laag-frequentie energie. Op dit moment kan alleen worden aangegeven voor welke gebieden deze modelfouten in SWAN waarschijnlijk optreden. Uit de analyse in deze studie kan worden afgeleid dat dit waarschijnlijk het geval is voor de SWAN resultaten voor de kust van Zeeuws-Vlaanderen, de landhoofden van de Waddenzee eilanden en voor de dijken in het Eems-Dollard estuarium, tijdens stormcondities met noordelijke tot noordwestelijke windrichtingen.

List of Tables

List of Figures

Deltares

1 Introduction

1.1 Framework

In compliance with the Dutch Water Act ("Waterwet, 2009") the strength of the Dutch primary water defences must be assessed periodically[1] for the required level of protection, which, depending on the area, varies from 250 to 10,000 year loads; as indicated in Figure 1.1. These loads are determined on the basis of Hydraulic Boundary Conditions (HBC). The HBC and the Safety Assessment Regulation ("Voorschrift op Toetsen op Veiligheid", VTV), play the crucial role in the assessment of the primary water defences. Until 2011, the safety assessment was based on the failure probability of a dike section. In the future, assessments will be based on the probability of flooding of a dike ring or dike ring trajectories. The corresponding normative return periods still have to be established, probably varying between 300 and 100,000 years. This means that not only the values in Figure 1.1 will change, but also the interpretation of the normative values, due to the probabilities of failure being different from the probability of exceedence of hydraulic loads presently used. The knowledge underlying the presently available HBC and VTV will be incorporated in the new instrumentation to assess the safety of dike rings, or at least parts of a dike ring. Most probably this new instrumentation will be Hydra-Ring (Deltares, 2011c, 2013b).
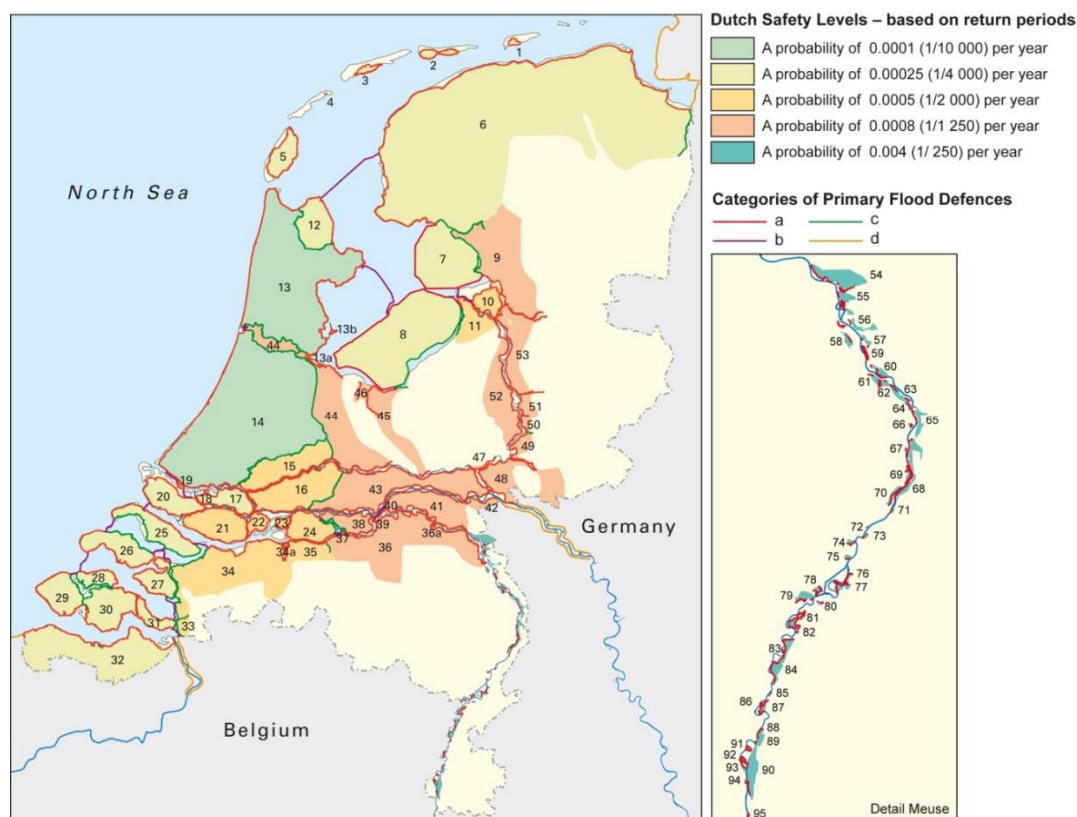
Figure 1.1   The safety standard of the Dutch primary water defences, as recorded in the Waterwet (2009). .

---

1.   *Previous assessments took place in 1996, 2001 and 2006. The date of the next assessment is 2017. According to the nieuwe Waterwet of January 1st, 2014 (https://zoek.officielebekendmakingen.nl/kst-33465-3.html) the assessment will be on a continuous basis for the period after 2017.*

With the aim of delivering legal assessment instruments to be used in the fourth assessment period, starting in 2017, DGRW is funding the long-term project WTI 2017, with Rijkswaterstaat – WVL as executive client for Deltares. The WTI 2017 program consists of seven content-based projects and four more generic projects, i.e. the horizontal resp. vertical clusters in Figure 1.2. Six of the seven content-based projects are related to strengths. As its name suggests the Hydraulic Loads project focusses on HBC in particular and on subjects related to hydraulic loads more in general.

The goal of the Hydraulic Loads project is twofold:
1. To determine Hydraulic Boundary Conditions for all water systems (new production runs only for river areas).
2. To fill in the most important knowledge gaps concerned to Hydraulic Loads in such a way that from 2017 on more reliable HBC for the Dutch primary sea and flood defences can be determined, either in the conventional approach of "probability of exceedence" or in the future approach of "probability of flooding".
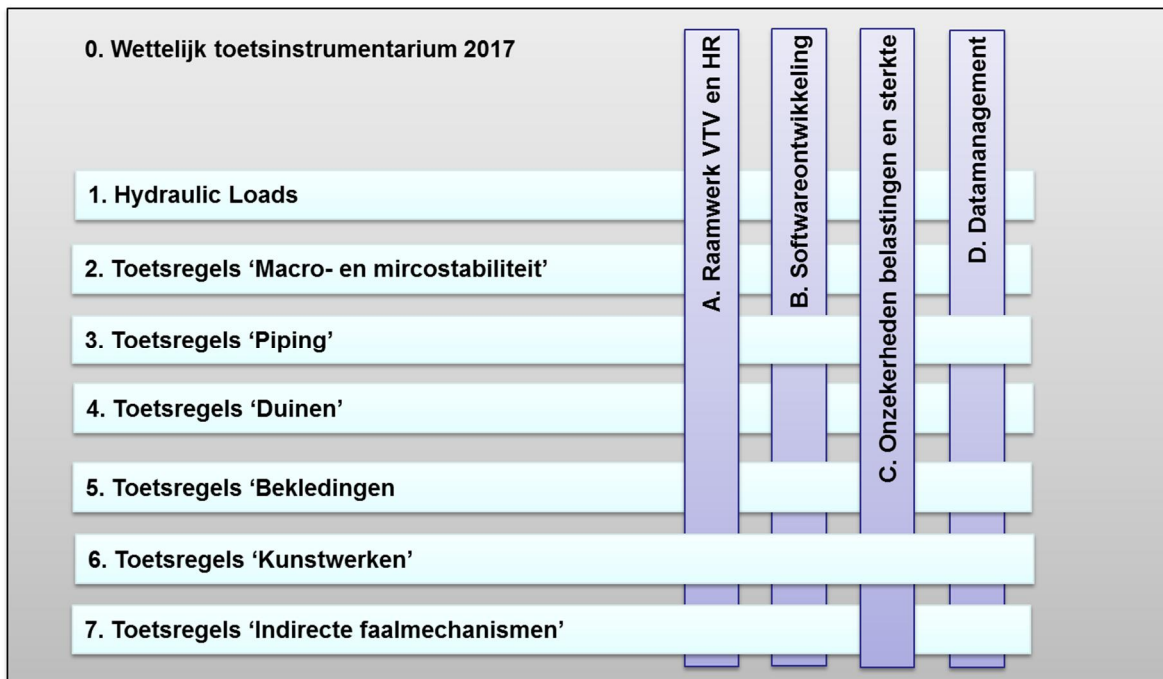
Figure 1.2   Organisation of the WTI 2017 project (mostly in Dutch).

In line with its two goals, the project is divided in two parts; one related to the determination of HBC and in particular to the production runs in the river areas, and the other is concentrating on filling the knowledge gaps in order to improve the quality of the HBC. The present report fulfils in part of the second goal.

The quality of the derived HBC depends on the adequate performance of a number of components in the so-called *HBC chain*. In this chain, statistics of waves, wind, water levels and river discharges and physical numerical model results from the input to probabilistic models (Hydra-Zoet and Hydra-K until 2011 and Hydra-Ring probably from 2017 on). These in turn provide the output of the HBC chain, namely the normative hydraulic loads, a combination of water level and/or wave height, wave period and wave direction per location, depending on the water system (coastal region, lakes or rivers) and on the failure mechanism under consideration.

Within the HBC chain, typically only one instant during a storm is considered, e.g. the instant at which the maximum water level is achieved in the region of the dike section of interest. For the determination of the required water defence's crest level this is an appropriate approach, since the maximum wave overtopping rate is typically obtained at the maximum water level. For failure mechanisms other than overtopping, the instant of the maximum water level does not necessarily lead to the critical load on the water defence. Furthermore, failure mechanisms such as dune retreat and erosion of revetments typically depend on the temporal, and also spatial, variation of the storm. In fact, the knowledge gaps in the various techniques and methods needed to derive the HBC pertain in most cases to the "time" and "space" dimensions. Regarding "space", it is worth noting that, for most water systems, wind fields are currently assumed to be spatially uniform in the computations of the HBC, which is unrealistic. The spatial uniformity assumption becomes even more unrealistic when temporal variations are accounted for.

The approach of the WTI – Hydraulic Loads project, presented already in Deltares (2011a), is based on improving models and methods in the three disciplines in which the knowledge gaps are clustered, namely:

• Statistical methods
• Numerical models (for instance wave models and flow models)
• Probabilistic models

Additional to these three disciplines a fourth discipline concerned with the determination of model uncertainties was added in Deltares (2013a). Within the new approach of probability of flooding of Hydra-Ring, uncertainties pertaining to model assumptions and statistical estimates are taken into account, whereas in WTI 2011 (the previous legal assessment instruments) only intrinsic uncertainties were considered.

The study reported here, whose motivation is given in the next section, focuses on the knowledge gap regarding "Numerical models".

1.2 Motivation

For the WTI calculations of the Hydraulic Boundary Conditions, which are to be finalized by the end of 2015 and established by the Minister in 2017, wave statistics obtained at deeper water buoys need to be transformed to the toe of the dike using the SWAN wave action model (Booij et al., 1999). This transformation is challenging in complex tidal inlet systems such as the Wadden Sea and the Western Scheldt in the Netherlands. For the wave model SWAN significant improvements have been made for the former areas (Van der Westhuysen et al., 2012, Zijlema et al., 2012). However, one of the unresolved issues in the Wadden Sea is that the penetration of North Sea waves (0.03 – 0.20 Hz) into the tidal inlets is still underestimated by the SWAN wave model.

The wave penetration into the Wadden Sea has been extensively studied in the past, but no full explanation for the underestimation has been found so far. The following has been found so far:

• A sensitivity analysis showed that the model-data agreement improves when the bottom friction is deactivated or its parameter value reduced (Zijlema et al., 2012), refraction on

the low-frequency waves is reduced, quadratic frequency-dependent wave breaking is applied and/or the water level is increased (Alkyon, 2009).

• Model computations with SWAN and the mild-slope-equation model PHAROS have shown that the effect of diffraction is local and hardly affects the amount of energy penetrating towards the mainland (Deltares/Alkyon, 2009).

• A comparison of SWAN results with laboratory experiments (Eslami et al., 2012) shows that SWAN does not overestimate the refraction of long waves when propagating from the deeper channel to the shallow flats.

However, in a comparison using laboratory data obtained for a port entrance study (unrelated to the WTI program) Groeneweg et al. (2014a) found that the Boussinesq-type model TRITON (Borsboom et al., 2000) correctly predicted that the wave height hardly decreased, when waves propagate obliquely across a flat into a channel. However, SWAN predicted a sharp decrease of wave height across the flat-channel slope, due to refraction at the channel-flat interface. Furthermore, Toledo (2013) showed that two-dimensional nonlinear wave triad interactions have great importance in oblique wave incidence problems. In these problems, sub-harmonic two-dimensional triad interactions play a significant role as they are capable of transferring energy from higher frequencies to lower ones in larger attack angles than the original incident wave input. By their nature, waves created by sub-harmonic waves have broader directionality comparing to the incident waves (Herbers et al, 1995) and thus could provide a mechanism by which energy is transferred over the flat-channel slope. This sub-harmonic energy transfer is not modelled in SWAN which only includes triad interaction transferring energy to higher harmonics. Furthermore, only wave energy transfer between wave components within the same direction is considered, thus a one-dimensional approach.

Groeneweg et al. (2014a, 2014b) showed that two-dimensional nonlinear interactions (and especially the sub-harmonic interactions) play a major role in the transmission of energy from flats into navigation channels, and that this process can explain SWAN's under-prediction of wave energy penetration into a complex tidal inlet system. With this mechanism in mind, it would be interesting to examine under which conditions SWAN underestimates the wave energy when propagating into complex tidal inlet systems. If a pattern can be found in the conditions under which SWAN is most likely to underestimate the low frequency energy, warnings could be given for which locations the reliability of the hydraulic boundary conditions might be less accurate.

1.3 Objectives

The aim of this study is to investigate under which conditions SWAN underestimates the low frequency wave energy when propagating into complex tidal inlet systems, like the Wadden Sea and Western Scheldt, paying special attention to the role of nonlinear interactions and refraction.

In this study we will indicate for which locations the reliability of the hydraulic boundary conditions might be less accurate because of the limited wave penetration in SWAN. It should be noted that no general correction value for the underestimated wave parameter values is given in this study. For a quantification of the uncertainties of the SWAN results reference is made to Deltares (2013c)

Modelling of wave penetration in complex areas: analysis of hindcast data

1.4 Approach

The approach is to reanalyse existing hindcasts, such as the 30 cases in the Western Scheldt (Witteveen+Bos, 2010), 11 cases in the Eastern Wadden Sea (Alkyon, 2008) and a large amount of available cases for the Amelander Zeegat. Hydrodynamic models (Delft3D or WAQUA) were used to predict the water levels and currents for the hindcasts. The model resolution of the different hindcast studies was based on the variation in bathymetry (and resulting variation in wave height). All hindcasts were done with the WTI settings, SWAN model version 40.72ABCDE, to be able to make a fair comparison. This version was also used for the WTI 2011 production runs. The WTI settings are:

- Quadruplet interactions using the DIA formulation by Hasselmann et al. (1985).
- JONSWAP formulation for bottom friction with a coefficient set to 0.038 m^2s^{-3} for fully developed wind-sea conditions in shallow water, as found by Bouws and Komen (1983).
- Depth-induced breaking under finite-depth wave growth conditions (Van der Westhuysen, 2009, 2010), model parameter settings: B = 0.96, β_{ref} = -1.3963, v = 500.
- Triad interactions using the LTA formulations by Eldeberky (1996).
- Wind generation and whitecapping based on Van der Westhuysen et al. (2007), but corrected for an underprediction of swell (Van der Westhuysen, 2007).
- Enhanced whitecapping dissipation on negative current gradients according to Van der Westhuysen (2011), model parameter setting C_{ds}"= 0.8.
- 80 iterations for complete convergence.
- The quadruplets are de-activated for Ursell numbers larger than 10. The threshold for fraction of breaking waves is set to 1.

In this reanalysis the focus is on the low-frequency energy. Model data will be analysed and compared to measurement data. For the Amelander Zeegat a more detailed analysis is done, as 2D measured spectra and wave radar data are available. Some basis concepts that will be used in this report are explained in appendix A.

Based on the reanalysis of the existing hindcasts an attempt is made to find a pattern in the conditions and the amount of propagation.

1.5 Outline of the report

The Western Scheldt hindcasts are the first hindcasts to be reanalysed in Chapter 2. Subsequently the Amelander Zeegat hindcasts are reanalysed in Chapter 3 and the Eastern Wadden Sea hindcasts in Chapter 4. Finally, conclusions and recommendations are presented in chapter 5.

Deltares

2 Western Scheldt

2.1 Introduction

The Western Scheldt estuary consists of an ebb tidal delta facing the North Sea to the Northwest and the Western Scheldt to the Southeast, see figure 2.1. A relatively straight channel cuts through the Scheldt mouth, oriented from west to east. A second channel follows the coastline of Walcheren. Due to the ebb tidal delta and the geometry of the Western Scheldt only a limited amount of low frequency wave energy penetrates into the Western Scheldt. Compared to the Wadden Sea, the geometry of the Western Scheldt delta is relatively simple and therefore a good first case to study the wave penetration.
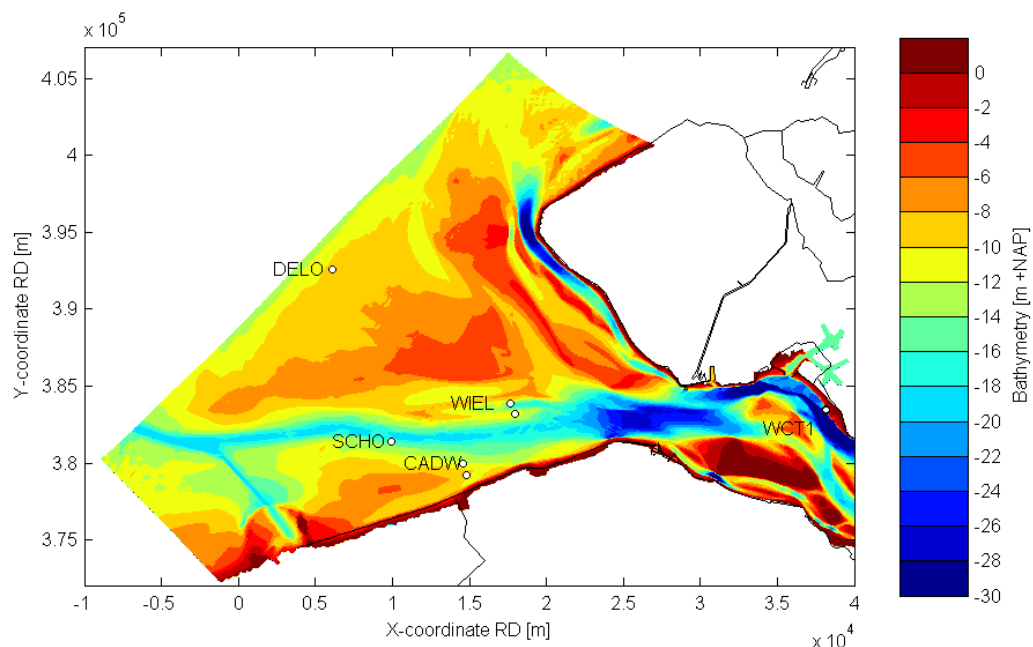
Figure 2.1   Bathymetry Western Scheldt estuary

The observed and modelled data of four different wave buoys were examined in this study: Deurlo (DELO), Scheur Oost (SCHO), Wielingen (WIEL) and Cadzand West (CADW). DELO and CADW are the only locations where the directionality of the waves was measured with a directional wave buoy and therefore these locations are used to provide directional information. Locations more inside the estuary, like the step gauge Westerschelde Container Terminal (WCT1), were not considered as the amount of low-frequency energy at these locations is very limited. Some measurement locations were relocated at a slightly different location during the period of 2002 to 2008, e.g. WIEL and CADW (see two locations indicated in Figure 2.1). The displacement of WIEL has some consequences for this analysis. Before 2006 the buoy was located on a flat near the southern channel (ca. -10 m +NAP), but moved north-westwards after 2006 to a deeper location, closer to the ebb tidal delta (ca. -15 m +NAP).

SWAN hindcasts of six different storms at 30 different moments in time for this area were performed, all by Witteveen+Bos (2010). Table 2.1 gives an overview of all hindcast

moments, including information on the wind velocity, wind direction and water level during those moments. All hindcast computations have been done with the WTI settings, described in Section 1.4.

Hindcast moment	U_{10} (m/s)	Udir (°N)	Water level (m NAP)
26/10/02, 02:00	18.69	257	1.55
27/10/02, 18:00	22.59	283	2.42
27/10/02, 19:30	20.12	288	1.92
20/12/03, 21:30	15.59	242	1.27
21/12/03, 06:30	18.18	256	-0.52
21/12/03, 08:00	18.61	268	0.16
21/12/03, 15:00	14.46	297	1.57
07/02/04, 01:00	14.86	241	1.36
07/02/04, 10:00	15.03	258	-1.00
08/02/04, 06:00	20.23	269	1.07
08/02/04, 07:00	21.11	276	0.36
08/02/04, 16:30	18.19	315	2.87
08/02/04, 18:00	18.07	317	1.96
12/02/05, 08:30	18.26	235	-0.93
12/02/05, 10:30	18.36	239	-2.08
13/02/05, 06:00	15.56	278	2.58
13/02/05, 08:30	15.45	283	0.33
14/02/05, 00:00	17.32	340	-0.47
14/02/05, 08:30	13.28	331	0.56
14/02/05, 13:30	14.94	318	-0.88
09/11/07, 01:30	16.49	327	3.45
09/11/07, 04:30	15.97	326	1.96
09/11/07, 07:30	18.64	322	0.73
09/11/07, 10:00	16.71	320	1.21
09/11/07, 14:00	14.98	326	2.97
09/11/07, 17:00	14.38	310	0.56
29/02/08, 22:30	18.88	235	-0.19
29/02/08, 23:30	19.31	238	-0.67
01/03/08, 03:30	19.85	247	0.06
01/03/08, 06:00	19.60	288	2.01

Table 2.1   Wind speed, wind direction and water level at 30 moments for which a hindcast is performed for the Western Scheldt estuary (see also Witteveen+Bos (2010)

2.2   Analysis

To identify patterns in the conditions for which SWAN underestimates the low-frequency energy, a figure for both SCHO and WIEL was made, where the depth was plotted versus the 1.5D peak wave direction and the computed measure for the low-frequency wave height H_{15} for every hindcast moment. See appendix A for an explanation of the 1.5D peak wave direction and the H_{15}.

Deltares

In Figures 2.2 and 2.4 the computed H_{15} (colored marker) is shown as a function of the depth on the y-axis and the 1.5D peak wave direction on the x-axis for SCHO and WIEL. A black circle indicates whether SWAN underestimates the measured H_{15}. For these moments the date is shown. Moments with a current larger than 0.5 m/s are marked with a star. The hindcast moments that are discussed in the text are marked with an arrow.

To help understand the patterns that are observed, Figure B.1 in appendix B shows the spatial distribution of the SWAN peak directions for four hindcast moments, near SCHO and WIEL. The first moment shows waves with wave direction mostly from 270 degrees, the second moment mostly from 290 degrees and the third and last moments mostly from 325 degrees. In addition, the observed and computed wave spectra of the locations DELO, SCHO and WIEL were plotted for each hindcast moment, with the observed and computed wave directions at DELO and CADW as a second plot, see Figures B.2-B.5.

Scheur Oost
Figure 2.2 shows that for part of the hindcast moments the waves propagated from westerly (270-300 degrees) directions towards SCHO. In the other part of hindcast moments the waves came from a north-westerly direction (~325 degrees). For many hindcast moments the low-frequency wave height at Scheur Oost (SCHO) is underestimated, especially for the more energetic moments (higher wave heights, more reddish colors). More low-frequency energy is coming from the north-westerly directions than from the west, probably because the storms from the Northwest have a larger swell component. Furthermore, during north-westerly storms the period of the highest storm surge coincides with large swell waves and therefore a correlation is seen between the water depth and the H_{15}.

For peak wave directions around 270-280 degrees, almost no cases with underestimation are observed. However, the low-frequency energy at those moments is very limited (less than 1 meter for most moments), see for example the 1D wave spectrum of hindcast moment 01-03-2008 3:30 (Figure B.2). Looking at the local bathymetry, it can be seen that the waves from the direction 270-280 degrees mainly propagate towards SCHO through the channel and the relatively deep area south of the channel, see Figure B.1a. The waves can propagate towards SCHO relatively unhindered and only some refraction around the channel is seen.

In the directional range between 280 and 300 degrees SWAN underestimates the low-frequency wave energy. This can be seen in for example Figure B.3, where the energy density and directional spectrum is presented for hindcast moment 27-10-2002 18:00. SWAN underestimates the measured low-frequency energy at this hindcast moment by 0.5 m. It should be noted that the computed energy density is already underestimated for DELO, which could mean that the low-frequency energy at wave boundary conditions is too low. However, the relative difference between the measured and computed spectrum is larger for SCHO than for DELO.

From hindcast moment 27-10-2002 18:00 in Figure B.1b it can be seen that wave energy from different directions arrives in SCHO. Probably part of the energy propagates through the channel, whereas part propagates over the shallow area to the south of SCHO. Although the offshore wave direction is ca. 300 degrees, no (or only a very limited amount of) energy reaches SCHO from the northern side of the channel. This is due to refraction on the ebb-tidal delta, which alters the wave direction. Unfortunately, no directional measurements are available for SCHO. This situation is quite complex, as wave energy propagates towards

SCHO from many different directions and therefore it is likely that differences are observed between the measured and computed H_{15}.

For wave directions larger than 315 degrees, the waves have to cross the ebb tidal delta first, then have to cross the channel to arrive at SCHO, see figure B.1d for hindcast moment 8-02-2004 18:00. Non-linear wave-wave interactions become more effective over the shallow ebb tidal delta and subsequently the crossing of a channel, supporting the hypothesis of Groeneweg et al. (2014a, 2014b) that these nonlinear interactions cause differences to occur between SWAN and the observations. A short description of the hypothesis is given in Section 1.2. The Ursell number ($Ur = HL^2/d^3$, where H is the wave height, L is the wave length and d is the depth) gives an idea how strong the nonlinear interaction are for this moment, see Figure 2.3. If Ur >>1, nonlinear interactions will be strong. Whereas, if Ur << 1, nonlinear interactions will not be effective. The figure shows that high values of the Ursell parameter (order 10) occur on the shallow ebb tidal delta, which is indicative of large non-linearities. Also refraction can be observed on the ebb-tidal delta and the edge of the channel. Figure B.5. shows that the energy at the peak frequency is strongly underestimated. On the other hand, the energy at frequencies between 0.12-0.2 Hz is overestimated by SWAN as the 1D approximation of the triads (three-wave interactions) in SWAN transfers too much energy from the peak of the spectrum to the second harmonics (around 0.16 Hz).

For wave directions larger than 315 degrees, there are four hindcast moments not marked for underestimation. When examining the related spectral plot, it can be seen that SWAN underestimates the peak in the frequency range of 0 – 0.15 Hz, but this is cancelled out by an overestimation of energy by SWAN (still in the range of 0 – 0.15 Hz) just before and/or after the peak, see figure B.4 for hindcast moment 9-11-2007 4:30. This explains why these four hindcast moments are not marked for underestimation.

No clear pattern is observed between the conditions where the current plays a role and where the low-frequency wave height is underestimated.
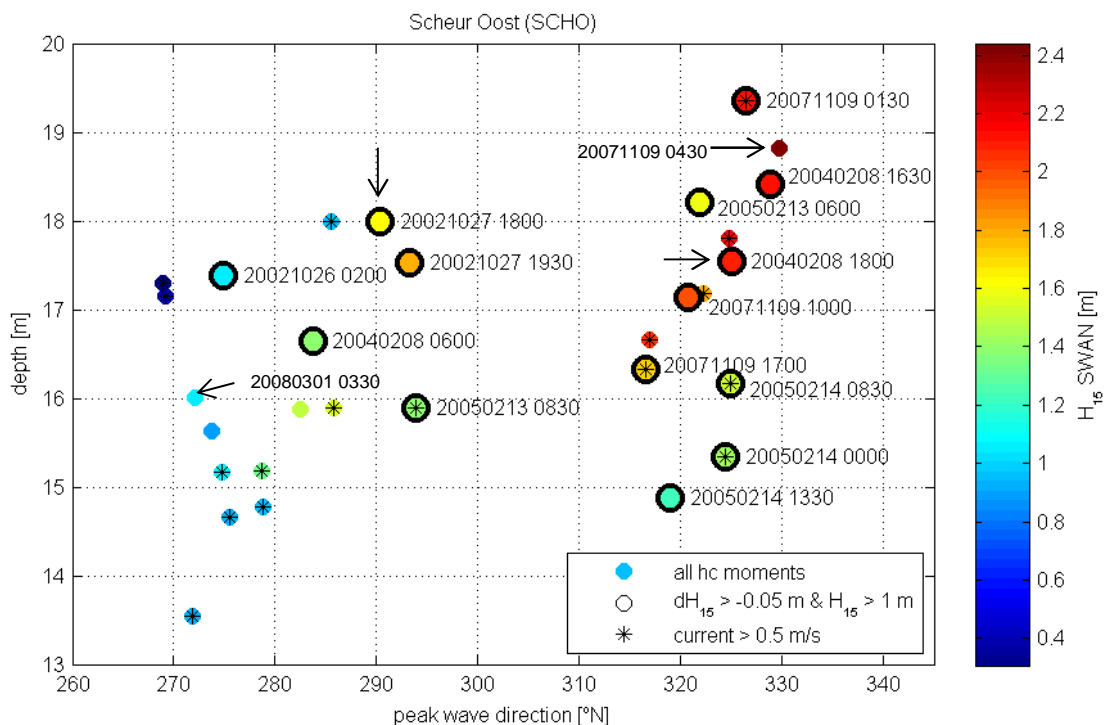
Figure 2.2   1.5D peak wave direction SWAN versus water depth at location SCHO. The H_{15} from SWAN is show as a coloured marker. A black circle indicates whether SWAN underestimates the measured H_{15}. Moments with a current larger than 0.5 m/s are marked with a star.
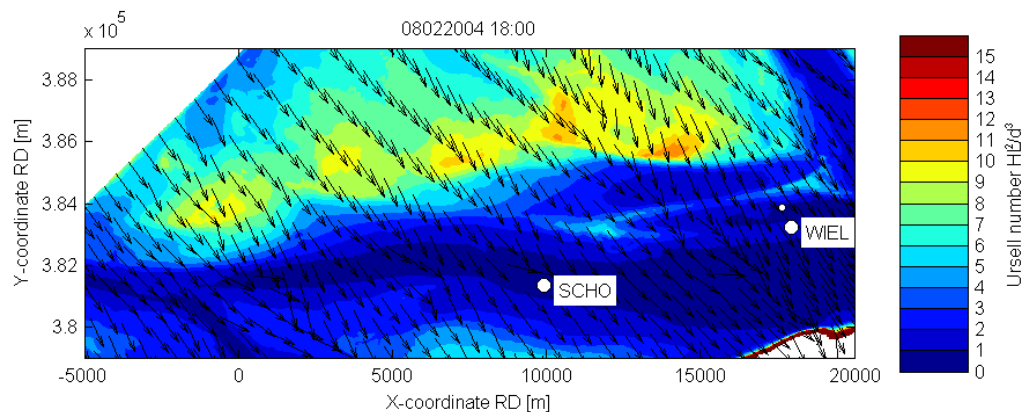
Figure 2.3   Spatial distribution of the SWAN peak wave directions and Ursell number (HL^2/d^3) for hindcast moment 08-02-2004 18:00.

Wielingen

Figure 2.4 shows the depth-direction scatter plot for Wielingen (WIEL). As WIEL was redeployed after 2006 at a deeper location, a split is made between the hindcast moments prior to 2006 (lower part of Figure) and after 2006 (upper part of Figure). Again the highest low-frequency waves come from northwesterly directions and a correlation between the water level and the amount of low-frequency wave energy that reaches WIEL is seen.

No underestimation of the computed H_{15} is observed for almost all cases with directions smaller than ca. 270 degrees for both locations of WIEL. From these wave directions the waves do not have to cross any tidal flats, as can be seen in figure B.1a for hindcast moment

01-03-2008 3:30. Therefore waves can propagate to WIEL relatively undisturbed, with only some refraction on the channel sides, which is well-predicted by SWAN.

Striking are the apparent differences between the two locations for wave directions larger than 270 degrees. At WIEL prior to 2006 (lower panel), the H_{15} is underestimated by SWAN for most of the moments with wave directions larger than 270 degrees e.g. see Figure B.3 and B.5 for hindcast moments 27-10-2002 18:00 and 08-02-2004 18:00, respectively. On the contrary, it appears from Figure 2.4 that the underestimation of H_{15} at WIEL after 2006 (top panel) only occurs for wave directions larger than 310 degrees. However, at a number of hindcast moments (during the November 2007 storm) the wave energy peak is also underestimated by SWAN for peak wave directions larger than 270 degrees and smaller than 310 degrees, see for example Figure B.4. This underestimation of the spectral peak is counteracted by a severe overestimation of the computed energy on the right side of the spectral peak (still within the range of 0 – 0.15 Hz), possibly caused by the 1D triad formulation in SWAN, which overestimates the transfer of energy form the peak frequency to the second harmonic. Also Figure B.1.c and B.1.d show that a similar wave pattern is seen for hindcast moment 09-11-2007 4:30 and for hindcast moment 08-02-2004 18:00.
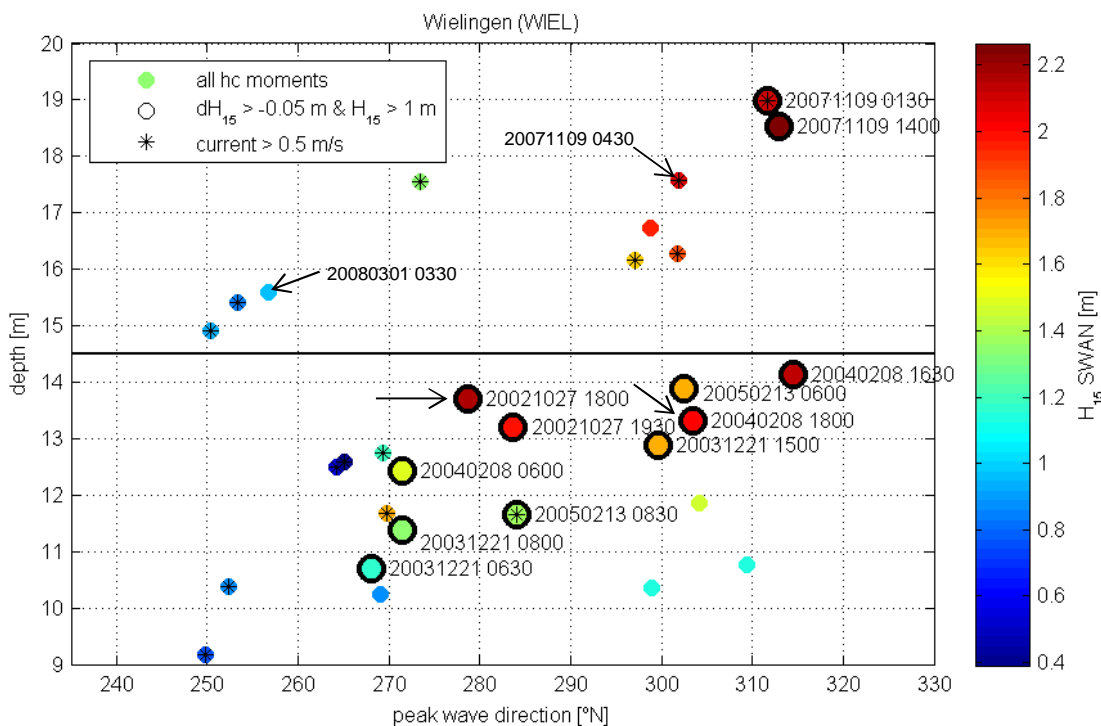
Figure 2.4   1.5D peak wave direction SWAN versus water depth at location WIEL: Lower Figure is WIEL prior to 2006, upper figure is WIEL after 2006. A black circle indicates whether SWAN underestimates the measured H_{15}. Moments with a current larger than 0.5 m/s are marked with a star.

2.3 Conclusions

Conclusions Scheur Oost and Wielingen
The most important conclusions from the analysis are:
- No underestimation of H_{15} was seen for almost all cases when the waves come from the West. This is when the wave direction is parallel to the channel and waves propagating towards SCHO and WIEL do not change much. Additionally, the H_{15} for westerly directions is very low, both in the observations as in SWAN.
- SWAN underestimates the low-frequency energy at SCHO and WIEL, when waves come from north to north-westerly directions.
- From the spatial plots it was concluded that refraction over the ebb-tidal delta and/or on the channel edges plays an important role for the north-westerly wave directions.
- For the north to north-westerly directions, where the waves propagate over the shoal, we observe that the computed low-frequency energy is often underestimated at SCHW and WIEL. This can be explained by the hypothesis of Groeneweg et al. (2014b), see also Section 1.2.

Consequences for locations near the coast of the Western Scheldt
Based on the analysis we performed at the measurement locations, we can briefly summarize the consequences for locations near the coast of the Western Scheldt. The conditions for which low-frequency energy is likely to be underestimated near the coast of the Western Scheldt are the north-westerly wave directions. Based on the analysis for SCHO and WIEL we could state that the impact of the underestimation of low-frequency energy by SWAN is probably highest at the coast of Zeeuws-Vlaanderen and is not very likely at the coast of Walcheren and inside the Western Scheldt.

Deltares

3 Amelander Zeegat

3.1 Introduction

The Amelander Zeegat is part of the Dutch Wadden Sea. The Amelander Zeegat has been extensively studied in several wave hindcast studies in the period 2004 – 2013 (see WL & Alkyon 2007, Alkyon 2007a,b, Royal Haskoning 2008, Witteveen+Bos 2008, Deltares 2008 and Deltares 2014), making use of recent measurement campaigns. Figure 3.1 shows the bathymetry of the Amelander Zeegat of the 2004 hindcast and the contourlines of the bathymetry of the 2013 hindcast. Large differences can be seen in the bathymetry, especially for the location of the channels. The main channel, which is north south oriented, is still roughly at the same location, except for the northern part of the channel. This part was bending towards the west in 2004, whereas in 2013 the orientation is more northwards. Furthermore, a west-east oriented channel has been developping, connecting the western side of the ebb-tidal delta to the main channel.

In this study, we use the data of the wave buoys located near the ebb-tidal delta and the main channel. These are locations AZB21, AZB31 and AZB32. At first, location AZB42 was also analysed, but as the low-frequency energy at this location was very low compared to the other locations, it has not been studied further. Figure 3.1 shows the locations of the measurement locations AZB21, AZB31 and AZB32. In the period 2004 to 2013 the buoy locations of some of the buoys have changed considerably. Buoy AZB21 moved further northwards; to make sure it was still located in the channel. In the period 2004-2005 AZB31 was located on the eastside of the channel, roughly at the location of buoy AZB32, being placed there for redundancy. Therefore the buoy information over this period will be added to the buoy data of AZB32. Buoy AZB31 was moved to the tidal flats on the west side of the channel in 2007 and eventually in 2013 the buoy was located inside the main channel. Buoy AZB32 was deployed in 2004 and stayed roughly at the same location.
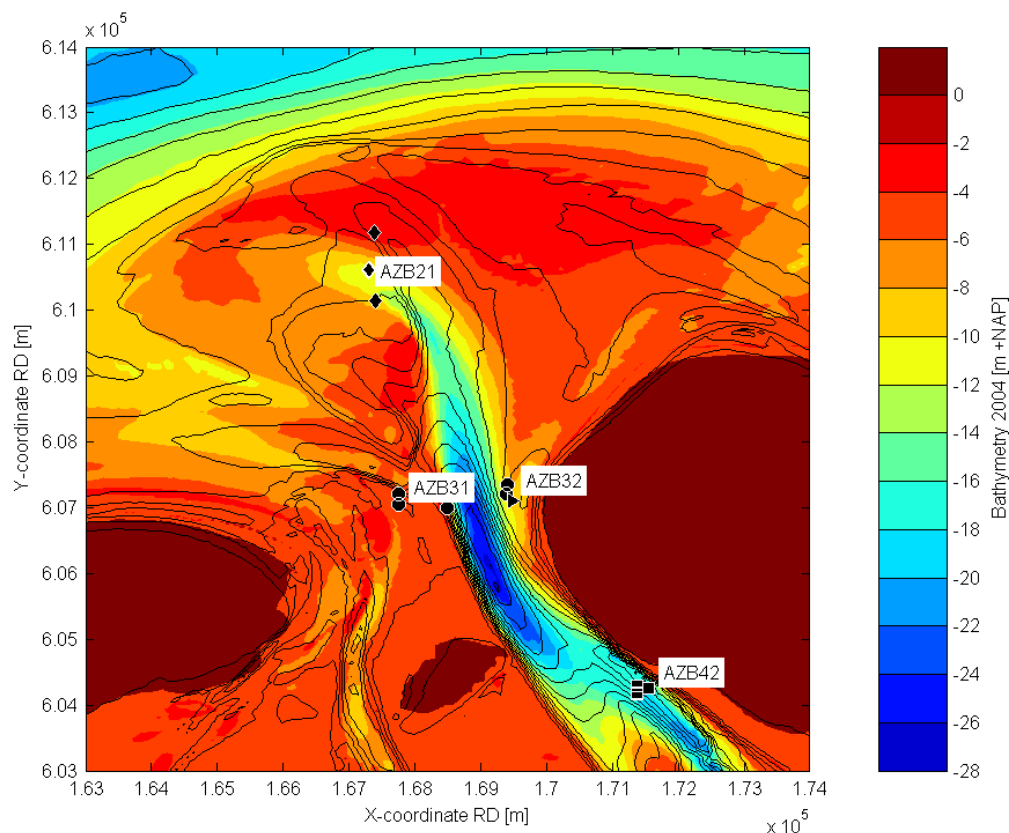
Figure 3.1   Bathymetry 2004 with bathymetry of 2013 (black contour lines). Locations AZB21: diamond marker;
AZB31: circle marker; AZB32 triangle marker; AZB42 square maker.

Tabel 3.1 gives an overview of the different hindcast moments that have been analysed in this study. The hindcast moments from 2004 to 2007 have been reported in Deltares (2011b). The results of these hindcasts were stored in the SWIVT database (SWAN Instrument for Validation and Testing, Wenneker et al. 2009). As mentioned in Section 1.4 the results were obtained by running SWAN with WTI settings. These settings have also been applied in the December 2013 hindcast, but without the Ursell limiter (see Section 1.4).

Hindcast moment	U10 (m/s)	Udir (°N)	WI (m NAP)	umax (m/s)	Tidal phase
08/02/2004, 20:00	13.5	314	1.0	2.3	flood
08/02/2004, 22:30	16.6	325	2.6	0.9	high w
09/02/2004, 01:30	16.3	328	1.8	1.7	ebb
16/12/2005, 10:00	20.0	277	1.0	2.0	flood
16/12/2005, 23:30	15.9	331	2.3	1.0	ebb
17/12/2005, 10:30	15.4	339	2.0	0.5	high w
11/01/2007, 13:00	19.5	228	1.0	0.7	high w
11/01/2007, 22:00	17.9	275	0.9	0.6	flood
11/01/2007, 22:40	18.8	279	1.3	0.7	flood
18/01/2007, 12:20	21.1	233	0.8	1.3	ebb
18/01/2007, 14:00	20.2	263	0.6	1.0	low w

18/01/2007, 17:20	20.3	267	1.4	1.1	flood
18/01/2007, 20:40	18.9	274	2.8	1.1	high w
18/03/2007, 10:00	13.8	279	1.7	0.4	high w
18/03/2007, 14:40	18.1	266	0.7	1.2	low w
18/03/2007, 15:40	17.9	271	0.6	0.8	low w
18/03/2007, 17:00	17.1	268	1.2	1.1	flood
18/03/2007, 19:20	16.3	268	3.0	1.3	flood
09/11/2007, 04:50	17.3	322	1.2	1.3	flood
09/11/2007, 09:20	18.4	326	2.7	0.7	high w
09/11/2007, 11:00	18.5	328	1.7	1.3	ebb
05/12/2013, 22:00	22.9	322	3.20	0.5	HW slack
06/12/2013, 00:00	24.6	303	3.26	1.1	HW ebb
06/12/2013, 06:00	21.5	306	1.68	0.3	LW flood
06/12/2013, 08:00	20.7	299	2.64	0.7	Flood
06/12/2013, 10:00	21.3	310	3.20	0.3	HW slack
06/12/2013, 13:00	18.6	296	2.21	1.5	ebb
06/12/2013, 15:00	18.1	310	1.30	1.7	ebb
06/12/2013, 18:00	15.0	305	0.26	0.7	LW ebb

Table 3.1   Wind speed, wind direction, water level and maximum current speed at 29 moments for which a hindcast is performed for the Amelander Zeegat

3.2   Analysis

As in the previous chapter, the computed low-frequency significant wave height was plotted as a function of the total water depth and the 1.5D peak wave direction of SWAN for every hindcast moment and location, in order to identify patterns in the conditions that SWAN underestimates the low-frequency energy. For most hindcast moments in the Amelander Zeegat the peak frequency in the studied spectra is smaller than 0.1 Hz, whereas in the Western Scheldt the peak frequency was often higher than 0.1 Hz. This means that the second harmonic component in the studied spectra of the Amelander Zeegat is observed at a frequency close to 0.15 Hz. As the second harmonic might provide additional uncertainties, the low-frequency significant wave height for the Amelander Zeegat is limited to the frequency range 0 to 0.10 Hz, and is denoted as H_{10}. More information about the 1.5D peak wave direction and the H_{10} can be found in appendix A.

The scatterplots are shown in Figures 3.2, 3.4, 3.5 and 3.7 for AZB21, AZB31 (location 2007 and 2013) and AZB32. In these plots the computed H_{10} (colored marker) as a function of the depth on the y-axis and the 1.5D peak wave direction on the x-axis for AZB21, AZB31 and AZB32 are shown. A black circle indicates that SWAN underestimates the low-frequency energy in the frequency range of 0 to 0.10 Hz. As for the Western Scheldt, moments with a current larger than 0.5 m/s are marked with a star.

To help understand the patterns that are observed, the spatial distribution of the peak directions computed with SWAN have been plotted for every hindcast moment, see appendix C, Figures C.1 – C.14. Wave radar information is available for the hindcast of December 2013 and the dominant wave direction of the radar has been plotted on top of the spatial plots for these hindcast moments. It should be noted that the radar picks up the longer waves up to 0.2 Hz far better than the shorter waves due to the rather low rotation speed of 2.85 seconds per cycle. Therefore, the dominant wave direction is mainly based on the lower frequencies, which is useful for this study. Gautier and Groeneweg (2012) conclude from comparing the

radar directional patterns with SWAN results that the radar seems to be reliable, though in specific areas differences can occur.

In addition, the observed and computed wave spectra at the measurement locations were plotted for each hindcast moment, with the observed and computed wave directions for every location as a second plot (see Figures C.15-C.18). As all three measurement buoys are directional waveriders, the pitch, roll and heave of the buoys was used to derive 2D-spectra with the Maximum Entropy Method (see Wenneker and Smale, 2013 for a description of the method). This was done only for the December 2013 hindcast, as the pitch, roll and heave data were readily available. For the Maximum Entropy Method the raw measured time series were split into time windows of 20 minutes each. The SWAN 2D spectrum nearest in time was sought to compare with the measured 2D spectrum. The time match is not exactly identical (often 10 min. difference). The matching time is shown in the title of the 2D spectrum. The 2D spectra (including the 1D spectrum) for 2013 are shown in Figure C.19 for AZB31 and C.20 for AZB32.

Buoy AZB21, location 2005 – 2007
The scatterplot for AZB21 (Figure 3.2) shows that SWAN underestimates the low-frequency energy for all hindcast moments, where the 1.5D peak wave direction is smaller than 318 degrees. See for example the spectral plots for hindcast moment 18-03-2007 14:40 and 18-03-2007 19:20. For these moments the H_{10} is relatively low. The hindcast moments with peak wave directions larger than ca. 320 degrees, have a much larger H_{10}, which is correlated with a high water level. It seems that for AZB21, the water level determines how much low-frequency energy propagates towards this location and whether it is underestimated by SWAN. However, no clear influence of the current can be observed.

With the help of the spatial fields of hindcast moments 18-03-2007 14:40 and 18-03-2007 19:20 (Figure C.2 and Figure C.4) this pattern is studied in more detail. The water level at 18-03-2007 14:40 is very low, which results in a water depth at the ebb tidal delta of less than 2 meters. This means that many waves break on the ebb tidal delta and that the amount of energy that reaches AZB21 from the north/northwest is limited. However, the waves that bend around the ebb tidal delta due to refraction, reach AZB21. These waves have a westerly direction, but limited low-frequency energy. The spatial fields of hindcast moment 9-11-2007 9:20 show that during higher water levels, the waves can propagate more easily over the ebb tidal delta. During this moment the peak wave direction is north-northwest.

However, for water depths between 12 and 13 meters and peak wave direction between 310 and 330 degrees, SWAN underestimates the H_{10} during some hindcast moments (e.g. 18-03-2007 17:00), whereas for other hindcast moments no underestimation is observed (e.g. storms December 2005 and November 2007, not marked). A difference between the hindcast moments is seen when looking at the wave direction at AZB11 (not shown), as this wave buoys lies further offshore and is not influenced by bathymetry effects: the storms, for which H_{10} is underestimated, come from a west to north-westerly direction, whereas the waves during the December 2005 and November 2007 storms come from a north-west to northerly direction. See for example Figures C.3 at hindcast moment 18-03-2007 17:00 and C.5 at hindcast moment 9-11-2007 4:50. For north-westerly wave directions, part of the wave energy propagates towards AZB21 from a more westerly direction, as it was refracted on the western part of the ebb-tidal delta. This is not the case for storms from a more northerly direction. Subsequently, the hypothesis of Groeneweg et al. (2014a, 2014b) could explain why one moment is underestimated by SWAN whereas the other moment is not. A short description of the hypothesis is given in Section 1.2. The spatial distribution of the Ursell number($U=HL^2/d^3$) gives an indication of how strong the nonlinear interactions are during this moment, see

Figure 3.3. If U >>1, nonlinear interactions will be strong. Whereas, if U << 1, nonlinear interactions will not be effective. The figure shows that high values of the Ursell parameter (order 30) occur on the shallow ebb tidal delta and tidal flats, which is indicative of large non-linearities.

Figure 3.2   1.5D peak wave direction SWAN versus water depth at location AZB21. A black circle indicates that SWAN underestimates the low-frequency energy in the frequency range of 0 to 0.10 Hz. The moments with a current larger than 0.5 m/s are marked with a star.
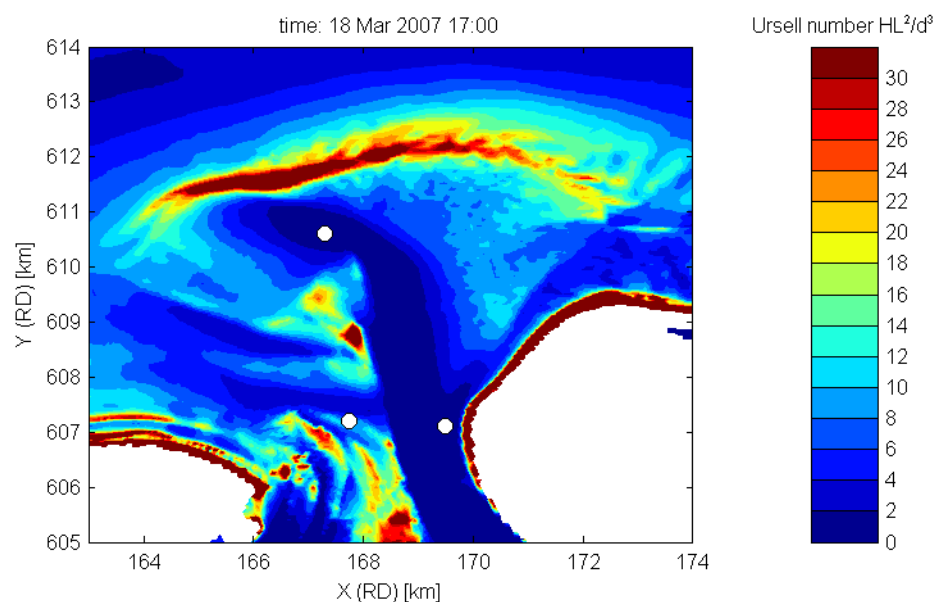
Figure 3.3   Spatial distribution of the SWAN peak wave directions and Ursell number (HL^2/d^3) for hindcast moment 18-03-2007 17:00.

Buoy AZB31, location 2007

For buoy AZB31 at the 2007 location, the pattern is similar to the pattern which was seen for AZB21. Again, an influence of the 1.5D peak wave direction and the water depth is observed. SWAN is more likely to underestimate the H_{10} for peak wave directions of less than 315 degrees. Furthermore, waves from directions larger than 315 degrees are likely to be higher and the wave direction further offshore is of influence.

The bathymetry of the Amelander Zeegat, in combination with the conclusions of Groeneweg et al. (2014a, 2014b) provide an explanation why SWAN underestimates the low-frequency energy for wave directions smaller than 315 degrees. Just north of AZB31 (location 2007) lies a channel, which has a west/ north-westerly orientation, as can be seen in the Figures C.1 – C.6. Refraction hampers waves from directions smaller than 315 degrees to pass into and across the channel in both reality as in SWAN, as the angle that the waves make with the channel, is larger than the frequency dependent critical angle for refraction. It is likely that in reality non-linear interactions, that are not present in SWAN, have broadened the directional wave spectrum, while the waves propagated over tidal flats in front of the channel. This way, an amount of energy can pass the channel in reality as the wave direction of a part of the waves has become smaller than the critical angle for refraction. This explains that in reality energy is present that SWAN cannot predict and hence the low-frequency wave energy in SWAN is underpredicted.

For wave directions larger than 315 degrees, the angle that the waves make with the channel is larger than the frequency dependent critical angle for refraction. Therefore, the low-frequency energy can enter the channel for both SWAN and the measurements.

Figure 3.4   *1.5D peak wave direction SWAN versus water depth at location AZB31 2007. A black circle indicates that SWAN underestimates the low-frequency energy in the frequency range of 0 to 0.10 Hz. The moments with a current larger than 0.5 m/s are marked with a star.*

Buoy AZB31, location 2013
In contrast to the location of AZB31 between 2005 and 2007, the buoy lies inside the main channel during 2013. No clear pattern between the water depth, the peak wave direction and the H_{10} is seen for buoy AZB31 at the 2013 location, see Figure 3.5. To examine this location in more detail, 2D spectra and spatial plots in combination with radar measurements of the December 2013 have been studied.
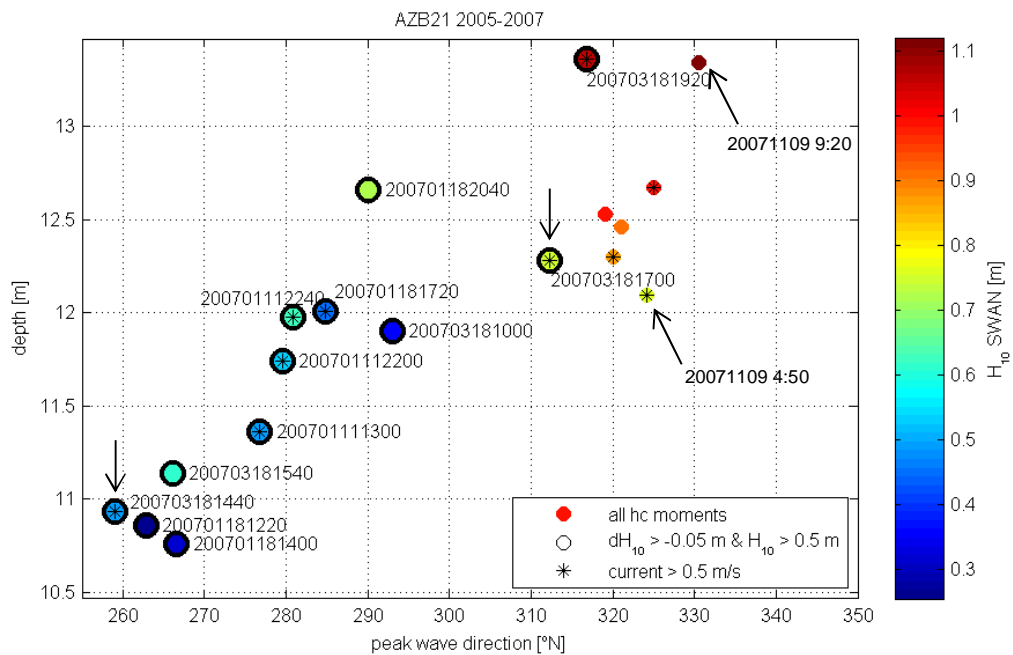

Figure 3.5   *1.5D peak wave direction SWAN versus water depth at location AZB31 2013. A black circle indicates that SWAN underestimates the low-frequency energy in the frequency range of 0 to 0.10 Hz. The moments with a current larger than 0.5 m/s are marked with a star.*

Figure C.19 shows the measured and computed 2D spectra for four hindcast moments at AZB31. Large differences can be observed between the measured and computed 2D spectra for hindcast moment 5-12-2013 22:00. The directional spread in the low-frequency energy is larger for the observed spectrum than for the computed spectrum. The measurement shows that waves propagate towards the wave buoy from the west, whereas no wave energy from wave directions smaller than 300 degrees is observed in the computed 2D spectra. The radar data in the spatial plot of hindcast moment 5-12-2013 22:00 show that this westerly wave energy comes from the tidal flat west of the channel, see Figure 3.6, which is a detail of Figure C.7. Most likely, the computed wave energy propagating over the tidal flat is refractively hampered to enter the channel as the waves turn towards the shoals.
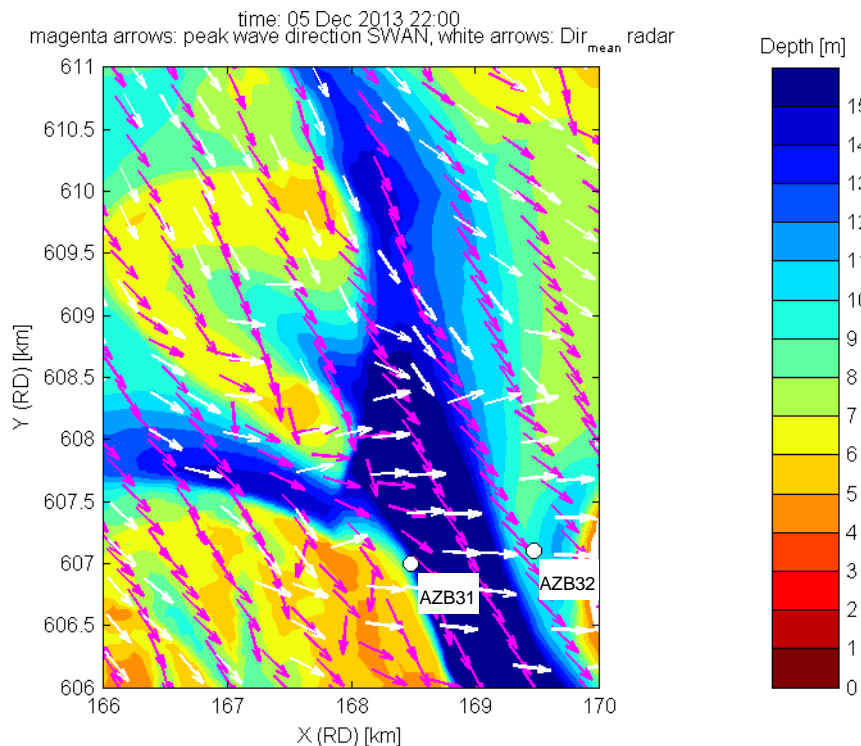
Figure 3.6 Spatial distribution SWAN peak wave directions (pink arrows) and radar dominant wave directions
   (white arrows) at hindcast moment 5-12-2013 22:00.

Although the difference between the measured and computed H_{10} is not large (except for 05-12-2013 22:00), the 2D spectra show significant differences for all hindcast moments shown in figure C.19. When comparing the spectra of 5-12-2013 22:00 with the spectra of 6-12-2013 10:00 no large differences between the two moments can be observed, other than the energy magnitude. In fact, all hindcast moments of the December 2013 storm, show that energy is underestimated at certain frequencies. However, for the hindcast moments that were not marked in the scatterplot, this underestimation is cancelled by a slight overestimation of energy at other frequencies in the low-frequency band of 0 to 0.10 Hz. Averaging over this frequency band leads to observed H_{10} values that are higher than or similar to the computed ones.

Buoy AZB32, including AZB31 for 2004 and 2005
No clear pattern between the water depth, the peak wave direction and the H_{10} is seen for buoy AZB32 in Figure 3.7. The computed low-frequency energy is not often underestimated, in contrast to the other locations that were studied. The 1D-spectral plots even show that the computed H_{10} is often overestimated, see for example Figure C.18 at hindcast moment 9-11-2007 9:20.
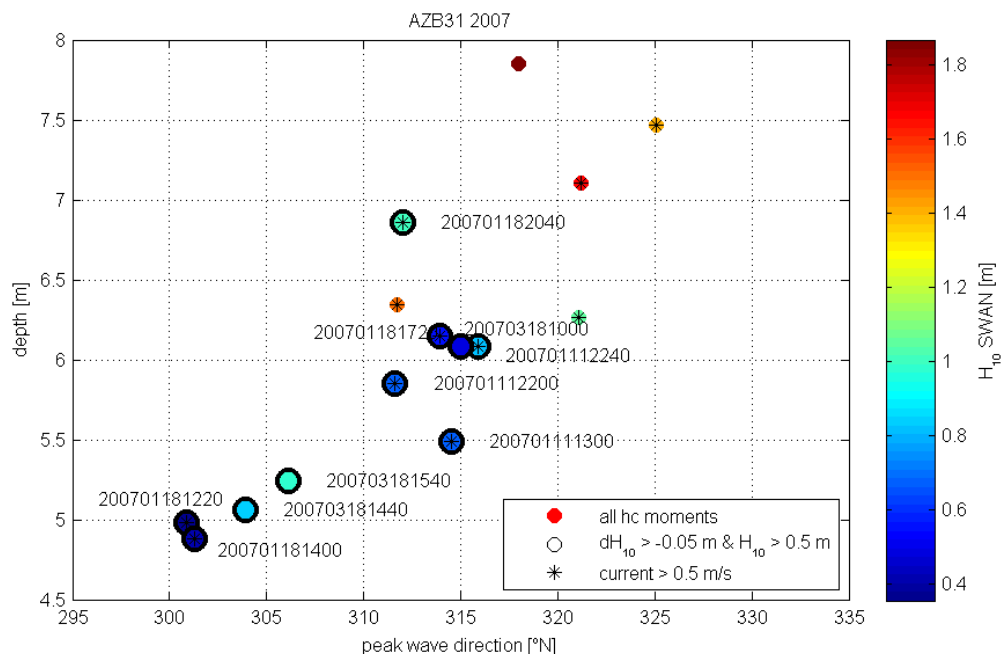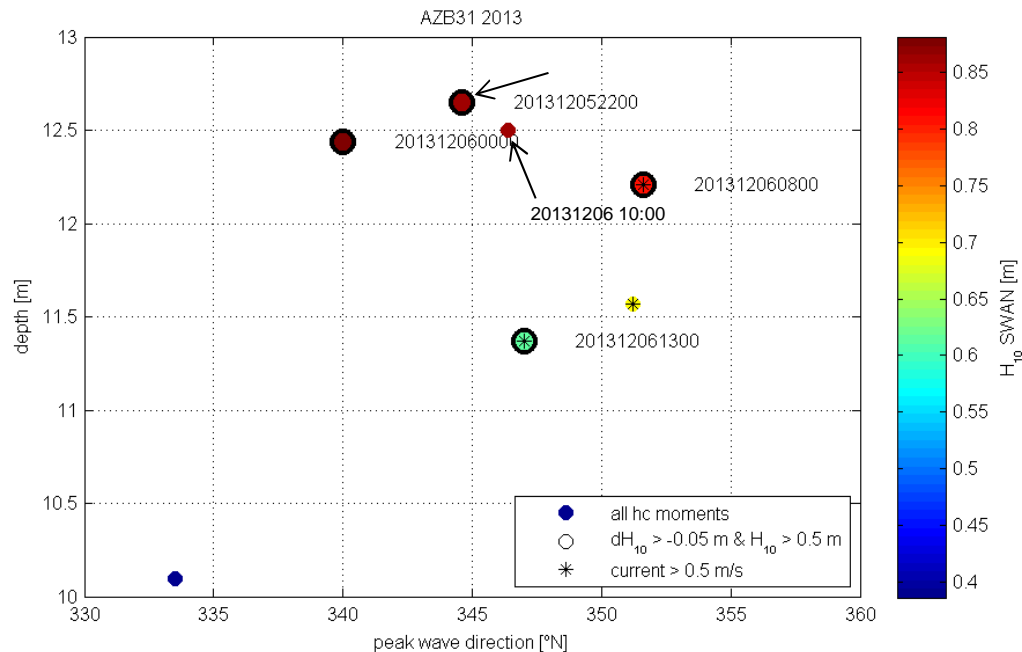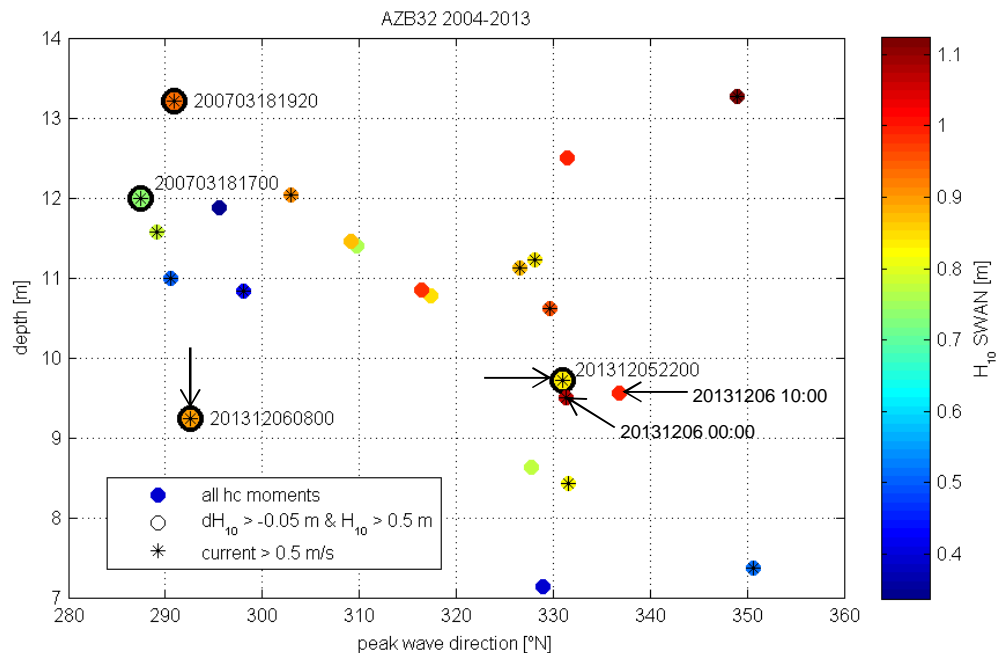
Figure 3.7   1.5D peak wave direction SWAN versus water depth at location AZB32 2004-2013. A black circle indicates that SWAN underestimates the low-frequency energy in the frequency range of 0 to 0.10 Hz. The moments with a current larger than 0.5 m/s are marked with a star.

Only four hindcast moments are marked for underestimation of the H_{10}. Two of these moments are from the December 2013 hindcast and therefore their 2D spectra can be analyzed from Figure C.20. At 05-12-2013 22:00 the observed spectrum in the frequency range between 0 – 0.1 Hz is directionally broader than the computed spectrum. In the observed spectrum a larger amount of wave energy from westerly waves are seen. For hindcast moment 6-12-2013 8:00 the observed energy is even more spread in the range 0 – 0.1 Hz. In this case SWAN is missing low-frequency wave energy from northerly directions.

The 2D spectral plots also make clear that SWAN severely overestimates the energy from northerly directions for most hindcast moments in the wind sea frequency range. This may be the waves propagating over the eastern part of the ebb tidal delta. It is beyond the scope of this study to explain why this happens for the wind sea. For hindcast moments 06-12-2013 00:00 and 06-12-2013 10:00, the wave energy from the northerly directions also includes low-frequency wave energy. As a result, SWAN overestimates the wave for those moments. An explanation for this is sought in the spatial distributions of the wave direction.

The spatial distribution of the wave direction for hindcast moment 5-12-2013 22:00 shows a remarkable difference between the measured radar data and the computed SWAN results (Figure C.7). The radar shows that the waves are travelling through the east-west oriented channel towards location AZB32, whereas Figure C.7 suggests that the waves in SWAN propagate mainly through the north-south oriented channel. However, it can be concluded from Figure C.20 that this is not the direction of the low-frequency energy (0-0.1 Hz). The computed low-frequency energy comes also from the east-west oriented channel. This example shows that the wave directions shown in the spatial plots are not always indicative for what happens with the low-frequency energy. It therefore is also hard to say why SWAN predicts low-frequency energy from a northerly direction for some hindcast moments.

Striking is that for all four moments, where the computed H_{10} is underestimated, strong currents are present. Table 3.2 shows the current magnitude and direction for all moments. At a depth between 7 and 14 meters, the propagation speed of the waves at 0.1 Hz is between 8 and 11 m/s. The current velocity is at most ca. 14% of the propagation speed. Therefore, wave blocking will probably not occur. For the hindcast moments marked for underestimation, with a peak wave direction of ca. 290 degrees, the current direction is from the north. However, for hindcast moment 05-12-2013 22:00, the current is from the south. Therefore, no clear relation could be found between these hindcast moments and the current.

Hindcast moment	Current velocity [m/s]	Current direction [^{o}N]
20070318 17:00	1.1	354
20070318 19:20	1.0	0
20131205 22:00	0.5	178
20131206 08:00	0.7	1

Table 3.2   Current speed and direction at 4 moments in 2013

3.3   Conclusions

Studied locations
A large number of storms has been analysed for different locations inside the Amelander Zeegat. For some locations (AZB21 and AZB31 location 2007) a clear dependency of the computed underestimation of H_{10} was observed on the water depth, the peak wave direction and the offshore wave direction. Here, there exists a strong correlation between the underestimation of H_{10} and the geometry. For example for AZB31 the effect of the critical angle of refraction for the west to east oriented channel is clearly seen.

For buoy AZB31 at the 2013 location only data from one storm was available. For this location, 2D wave spectra of the measurements and SWAN were very helpful in explaining the observed underestimation of H_{10} by SWAN. From the 2D wave spectra it was deduced that in SWAN no wave energy propagates from the tidal flat (west of location AZB31) into the main channel, whereas there was a westerly directed component in the observed 2D spectra. This conclusion is confirmed by the radar data in the spatial plots. This effect is due to the refraction of the directionally-narrower spectra in SWAN.

Finally, for location AZB32, no clear patterns could be observed. The observed 2D spectra show that the directional spectrum for the lower frequencies is broader than in SWAN. Whereas SWAN shows for some moments a clear peak for low-frequency energy coming from the North, this peak is not observed in the measurements. However, the main problem for this location seems to be that the low-frequency energy is overestimated by SWAN for most hindcast moments.

Consequences for the Amelander Zeegat
From the analysis in the previous section it can be concluded that it is very difficult to predict a pattern for the underestimation of low-frequency energy for SWAN for the whole Amelander Zeegat. The patterns that were seen for the studied locations seem to be very location specific. Near the ebb-tidal delta (for example buoy AZB21), the underestimated H_{10} is often caused by the ebb-tidal delta during low water levels or by the channel geometry. It was seen that the directional spreading of computed directional spectra is smaller than observed for the lower frequencies, and this causes differences when refraction occurs. These conclusions support the findings of Groeneweg et al. (2014a, 2014b), which is described in Section 1.2.

From the findings for wave buoys AZB31 and AZB32 it can be concluded that inaccuracies in the computed H_{10} are likely to occur at the headlands of the island of Ameland, as the amount of low-frequency energy penetrating towards the Ameland coast is high and sometimes large differences in observed and computed low-frequency wave energy were seen at AZB31 and AZB32.

For locations further into the Amelander Zeegat it becomes very complex. However, the amount of low-frequency energy that propagates into the Wadden Sea is very limited in the computed as well as the measured data, e.g. see location AZB42. The conditions at locations further into the Amelander Zeegat are dominated by local wind sea. For the storms that have been analysed in this study, inaccuracies in the propagation of low-frequency waves are not very likely to influence the results of SWAN at dike locations inside the Wadden Sea. However, this cannot be necessarily concluded for normative conditions, as the water level is much higher then.

4 Eastern Wadden Sea

4.1 Introduction

The Eastern Wadden Sea includes several tidal inlets between the islands of Ameland, Schiermonnikoog and Borkum. In this study we focus on the most easterly inlet, the Ems-Dollard estuary, as most wave measurements are available for this inlet. In contrast to the other tidal inlets of the Wadden Sea, the Ems-Dollard estuary is relatively open; a deep channel cuts through the ebb-tidal delta, connecting the North Sea with the river Ems, see Figure 4.1. This channel is dredged regularly to benefit shipping. However, the open geometry of the Ems-Dollard estuary makes the area more prone to flooding from surges and waves.
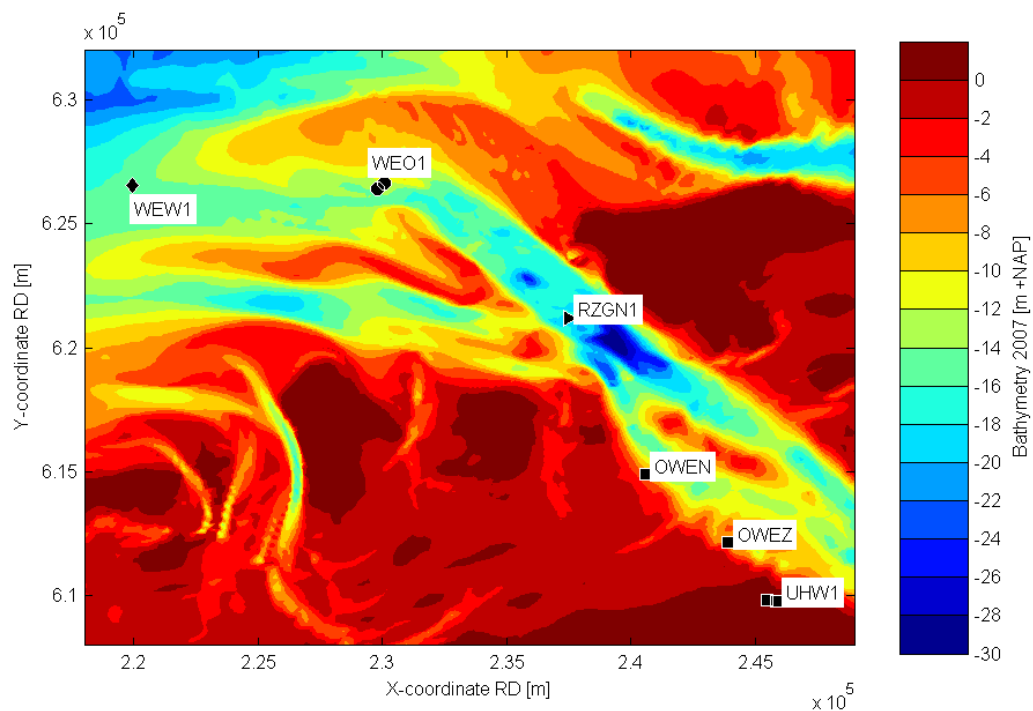
Figure 4.1   Bathymetry Ems-Dollard estuary

Two hindcast studies have been carried out for this area: the November 2007 storm by Alkyon (2008) and the December 2013 storm by Deltares (2014). Table 4.1 shows the moments that were hindcasted, with a summary of the conditions during these moments. The hindcast moments for the November 2007 storm are moments from the SWIVT database (SWAN Instrument for Validation and Testing, Wenneker et al. 2009) and have been computed by Deltares (2011b) with the WTI settings, as described in chapter 1. The December 2013 hindcast has also been done with the WTI settings, but without the Ursell limiter.

During the November 2007 storm, the waves were monitored at WEO1 and UHW1, whereas during the December 2013 storm, wave measurements were taken at all six locations WEW1, WEO1, RZGN1, OWEN, OWEZ and UHW1, see Figure 4.1. Because of its location, WEW1 is not much affected by the geometry of the tidal inlet. Also, buoys OWEN and OWEZ are less

interesting, as they are both located outside the tidal channel and this means that the low-frequency energy that reaches these locations is very limited. The same holds for UHW1, but its location close to the dike could give an indication of the differences between observations and SWAN results at the dikes of Groningen. Therefore, the main focus in this study is on the wave buoys WEO1, RZGN1 and UHW1. Some small displacement can be seen in Figure 4.1 for the buoys WEO1 and UHW1 between 2007 and 2013. As the displacement is small, the data from both hindcast studies are combined.

Hindcast moment	U_{10} (m/s)	Udir (°N)	Water level (m NAP)	umax (m/s)
08/11/2007, 19:20	13.1	319	1.3	0.7
09/11/2007, 06:20	17.3	326	1.9	0.7
09/11/2007, 07:00	19.9	326	2.3	0.8
09/11/2007, 07:20	19.4	327	2.5	0.7
09/11/2007, 09:00	18.2	332	3.1	0.3
09/11/2007, 09:10	18.3	332	3.1	0.2
09/11/2007, 09:30	18.4	332	3.1	0.2
09/11/2007, 09:40	18.4	332	3.1	0.2
09/11/2007, 10:20	18.7	332	3.0	0.3
09/11/2007, 11:00	18.9	333	2.8	0.5
09/11/2007, 13:40	19.5	333	1.3	1.1
05/12/2013, 20:00	19.3	295	1.9	1.0
05/12/2013, 22:00	22.9	322	2.9	0.5
06/12/2013, 00:00	24.6	303	3.5	0.3
06/12/2013, 04:00	21.3	296	1.6	1.6
06/12/2013, 07:00	18.9	307	1.6	0.5
06/12/2013, 09:00	20.7	298	2.6	0.9
06/12/2013, 12:00	20.3	301	2.4	0.5
06/12/2013, 14:00	17.0	318	1.4	1.3

Table 4.1   Wind speed, wind direction, water level and maximum current speed at 19 moments for which a hindcast is performed for the Eastern Wadden Sea

4.2   Analysis

As in the previous chapter, the computed H_{10} was plotted as a function of the total water depth and computed 1.5D peak wave direction for every hindcast moment and location to identify patterns in the conditions for which SWAN underestimates the low-frequency energy. The scatterplots are shown in Figures 4.2,4.4 and 4.5 for WEO1, RZGN1 and UHW1. As in the two previous chapters, a black circle indicates whether SWAN underestimates the low-frequency energy in the frequency range 0 to 0.10 Hz. Moments with a current larger than 0.5 m/s are marked with a star.

To help understand the patterns that are observed, the spatial distributions of the SWAN computed peak directions have been plotted for every hindcast moment, see Figures D.1 and D.2 in appendix D. In addition, the observed and computed wave spectra at the measurement locations were plotted for each hindcast moment, with the observed and computed wave directions for every location as a second plot, see Figures D.3 to D.5. As WEO1 and RZGN1 are directional waveriders, the pitch, roll and heave of the buoys was used to derive 2D-spectra with the Maximum Entropy Method (see Deltares, 2012 for a description of the

method), see Figures D.6 and D.7. This was done only for the December 2013 hindcast, as the pitch, roll and heave data were readily available. To study the differences in directionality further, the wave energy density at the low-frequency peak was plotted against the wave directions, see Figures D.8 to D.11. Here, only wave energy peaks in the frequency range between 0 to 0.1 Hz were considered.

Buoy WEO1
From Figure 4.2 no clear pattern can be identified between the depth and the computed peak wave direction and magnitude of H_{10}. For most hindcast moments the H_{10} is considerable, with often a magnitude of ca. 3 metres. From the November 2007 storm three consecutive moments, were examined, with very similar wave directions and water depths, but different comparisons of low-frequency wave energy, see Figures D.3 to D.5:
• 09-11-2007 09:00, the measured and computed low-frequency energy is comparable;
• 09-11-2007 09:40, SWAN overestimates the measured low-frequency energy;
• 09-11-2007 10:20, SWAN underestimates the measured low-frequency energy.

Striking is that the 1D SWAN spectra are roughly the same for all three moments. However, the amount of measured wave energy is different. Also, the measured and computed mean wave directions are comparable for the three hindcast moments. It is hard to say what causes the differences between SWAN and the measurements only based on the 1D spectra.
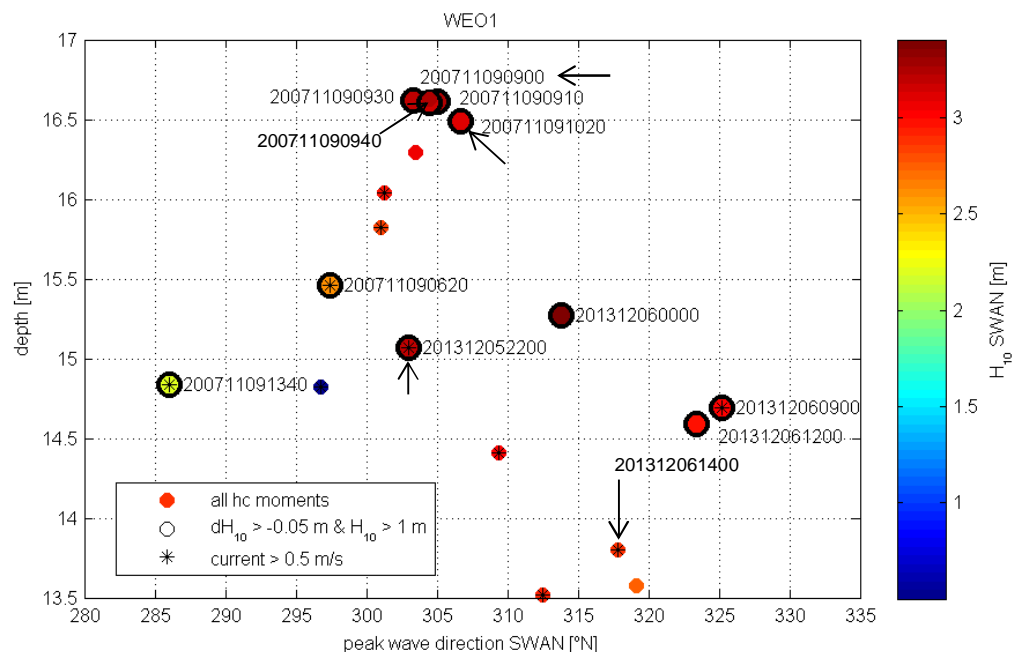
Figure 4.2   1.5D peak wave direction SWAN versus water depth at location WEO1

As 2D spectra are available for the December 2013 hindcast, two additional hindcast moments have been studied; 5-12-2013 22:00 and 6-12-2013 14:00. For hindcast moment 5-12-2013 22:00 the H_{10} is severely underestimated by SWAN, see the 1D spectrum at the top of Figure D.6. However, the 2D measured and computed spectra seem to be very similar in shape. By plotting the wave energy at the low-frequency peak against its directional distribution, a difference in wave energy is observed between SWAN and the measurement for wave directions between 260 and 320 degrees, see Figure D.8. With the help of the channel and flat geometry (Figure D.1), it is seen that the waves from this sector traverse the

western part of the ebb-tidal delta and propagate up the channel. Both in SWAN and in the measurements there is refraction on the ebb-tidal delta and the waves will turn towards the ebb-tidal delta. In addition, non-linear interactions become important over the ebb-tidal delta and tend to broaden the spectrum. As a consequence, part of the wave energy is propagating into the channel. In SWAN the energy density spectrum will not be broadened by non-linear wave interactions. Nevertheless, part of the difference at the peak of the distribution is already caused offshore, as this is also seen for location WEW1 (not shown).

At hindcast moment 6-12-2013 14:00 the 1D observed and computed spectra are very similar and no computed underestimation of H_{10} is observed, see Figure D.6 (bottom row). The computed 2D spectra shows two peaks in the frequency range 0 to 0.1 Hz, in contrast to the observed 2D spectrum. Figure D.9 shows this observation more clearly at the peak frequency. The directional distribution of SWAN shows one peak at ca. 270 degrees and one peak at 335 degrees. So wave energy in SWAN propagates from the channel towards WEO1 and directly over the ebb-tidal delta. The directional distribution of the measurement shows only one peak at ca. 320 degrees with a smooth spreading on both sides. The evenly distributed energy might be an artefact of the Maximum Entropy method, which was assumed to make the 2D wave spectrum. However, it is likely that due to non-linear interactions on the ebb-tidal delta, that are not present in SWAN, a broader and different directional distribution is created. The spatial distribution of the Ursell number ($U=HL^2/d^3$) gives an indication of how strong the nonlinear interactions are during this moment, see Figure 4.3. If U >>1, nonlinear interactions will be strong. Whereas, if U << 1, nonlinear interactions will not be effective. The figure shows that high values of the Ursell parameter (order 30) occur on the shallow ebb tidal delta and tidal flats, which is indicative of large non-linearities.
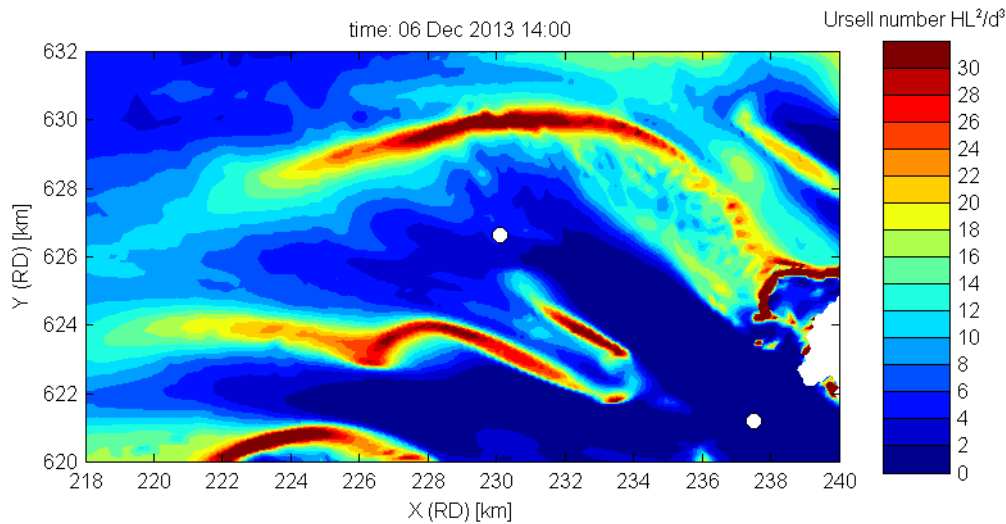
Figure 4.3   Spatial distribution of the SWAN peak wave directions and Ursell number (HL^2/d^3) for hindcast moment 06-12-2013 14:00.

Buoy RZGN1
No wave measurements for buoy RZGN1 were available for the November 2007 storm, so only the eight hindcast moments of the December 2013 storm are shown in Figure 4.4. For two hindcast moments the computed H_{10} is underestimated. Based on this overview, two hindcast moments have been studied further; 6-12-2013 00:00 and 6-12-2013 12:00.

Figure 4.4   1.5D peak wave direction SWAN versus water depth at location RZGN1

For hindcast moment 6-12-2013 00:00 only small differences are observed in the low-frequency range of the measured and observed 1D spectra, see second row of Figure D.7. The computed second peak is severely overestimated, similar to what has been seen for bu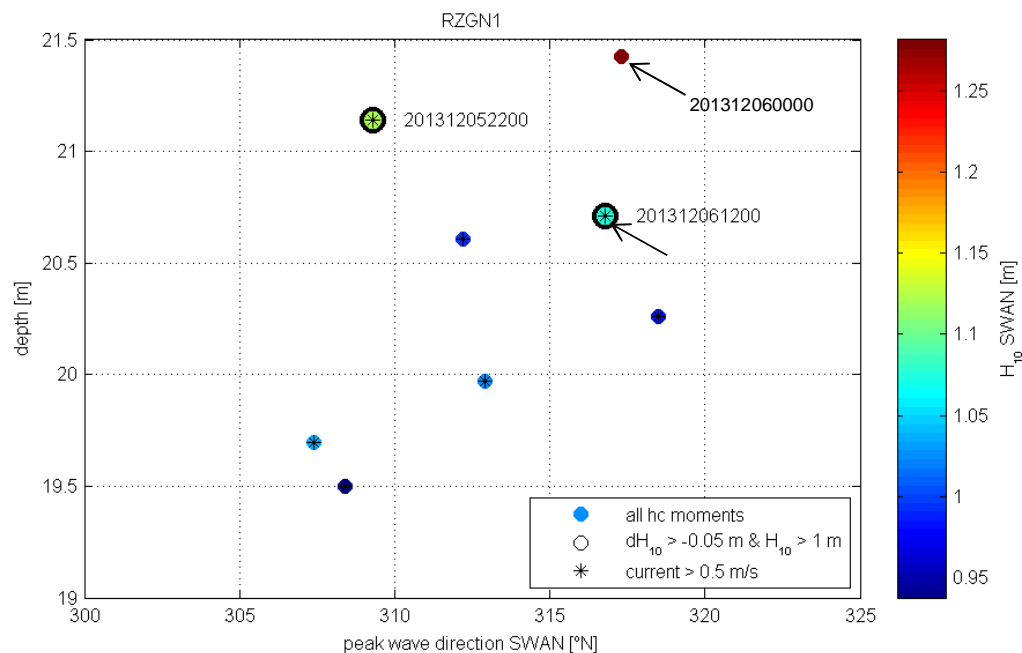oy AZB32 in the Amelander Zeegat. However, this is outside the frequency range from 0-0.1 Hz. For both the measured and the computed 2D spectrum one peak is seen in the frequency range between 0 to 0.1 Hz, see Figure D.7. However, Figure D.10 shows that the wave energy peak for SWAN is at ca. 305 degrees, whereas the observed wave energy peak is at ca. 290 degrees. From the spatial plot in Figure D.2 it can be seen that the main part of the wave energy in SWAN comes from the channel (and crossed the ebb-tidal channel to the north/northeast of RZGN1 before). As the wave direction is parallel to the channel, the energy propagates through the channel. However, the measured peak direction shows that most energy comes from the shallow flat northwest of RZGN1. With the theory of Groeneweg et al. (2014b), briefly explained in Section 1.2, it can be explained that for the observation the directional distribution has become broader on the flats and ebb-tidal delta due to non-linear interactions. Therefore, waves can propagate into the channel from the flat to the northwest of RZGN1.

At hindcast moment 6-12-2013 12:00 the computed low-frequency wave energy is severely underestimated (Figure D.7, third row). From the 2D wave spectra it can be seen that the directional peaks of both SWAN and the observations are from a similar direction (ca. 310 degrees) and the directional spreading is also similar but not identical, see Figures D.7 and D.11. The computed directional distributions seem to be missing wave energy in the peak for the directions in the range 305 to 330 degrees and on the left flank of the distribution for the directions in the range 280 to 305 degrees. The spatial fields of Figure D.2 show that the waves from the latter directional range have crossed the tidal flat northwest of RZGN1 and the difference is probably the same as for hindcast moment 6-12-2013 00:00. The difference at the peak of the distribution remains unexplained.

Buoy UHW1

Figure 4.5 shows that the H_{10} is underestimated by SWAN for many hindcast moments. Striking is that for the November 2007 storm all hindcast moments have been marked for underestimation, as already noticed in the hindcast study by Alkyon (2008), whereas for the December 2013 storm only half of the moments were marked, see also Table 4.2. Figure 4.5 and Table 4.2 show also that much more low-frequency energy penetrated into the tidal inlet for the November 2007 storm than for the December 2013 storm. A likely explanation for this difference is that November 2007 came from a more northwesterly direction with higher water levels than the December 2013 storm and therefore low-frequency waves could penetrate deeper into the tidal inlet via the channels.

The observed and computed wave energy density spectra in the range 0 to 0.1 Hz are very similar for hindcast moments 5-12-2013 22:00, 6-12-2013 00:00 or 6-12-2013 9:00, whereas the low-frequency energy at hindcast moment 6-12-2013 12:00 is clearly underestimated. All these hindcast moments have an H_{10} of 16 centimetres or more. The H_{10} at RZGN1 during the moment 6-12-2013 12:00 was already underestimated by SWAN, so this could mean that the difference in H_{10} was caused already in the channel. Unfortunately, no directional information is available for UHW1 for this storm, which could possibly explain the differences between the hindcast moments.
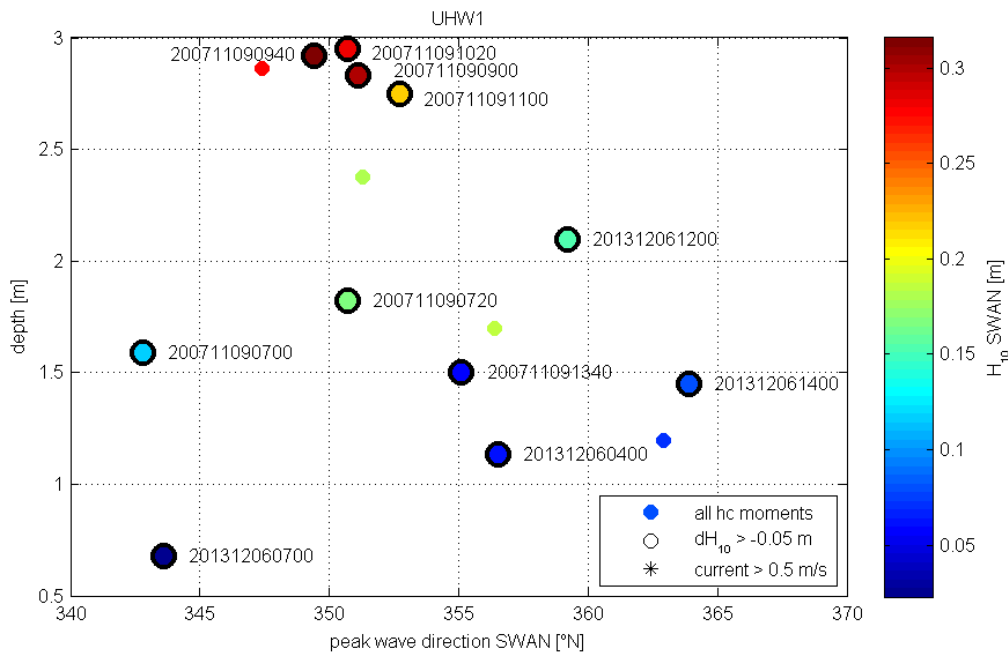

Figure 4.5   1.5D peak wave direction SWAN versus water depth at location UHW1

Date and time	H_{10} SWAN [m]	H_{10} obs [m]	Difference [m]	Rel. difference [%]
08/11/2007, 19:20	0.01	-	-	-
09/11/2007, 06:20	0.05	-	-	-
09/11/2007, 07:00	0.12	0.22	-0.10	-46
09/11/2007, 07:20	0.16	0.23	-0.07	-29
09/11/2007, 09:00	0.30	0.43	-0.13	-30
09/11/2007, 09:10	0.31	-	-	-
09/11/2007, 09:30	0.32	-	-	-
09/11/2007, 09:40	0.32	0.48	-0.16	-34
09/11/2007, 10:20	0.28	0.42	-0.14	-33
09/11/2007, 11:00	0.22	0.34	-0.12	-37
09/11/2007, 13:40	0.06	0.20	-0.16	-72
05/12/2013, 20:00	0.07	0.07	0	-4
05/12/2013, 22:00	0.18	0.21	-0.03	-13
06/12/2013, 00:00	0.28	0.27	+0.01	4
06/12/2013, 04:00	0.06	0.17	-0.11	-63
06/12/2013, 07:00	0.02	0.08	-0.04	-70
06/12/2013, 09:00	0.19	0.19	0	1
06/12/2013, 12:00	0.16	0.27	-0.11	-42
06/12/2013, 14:00	0.08	0.19	-0.11	-58

Table 4.2   Difference H_{10} computed and observed. Differences of more than 10 cm are marked orange.

4.3 Conclusions

Studied locations
Two storms have been analysed for the Eastern Wadden Sea. In this analysis the main focus was on the Eems Dollard estuary. No clear dependency of the computed underestimation of H_{10} was observed on the water depth or the peak wave direction. Furthermore, with only the 1D spectra and the spatial plots, no conclusions could be drawn.

However, the 2D wave spectra of the December 2013 storm were very helpful in understanding the observed underestimation of H_{10} by SWAN for both locations WEO1 as RZNG1. From the 2D wave spectra it was deduced that the directional wave energy distribution at the wave buoys is often different in the observed spectra than in SWAN.

For this north-westerly storm, a large part of wave energy computed by SWAN crosses the ebb-tidal delta and then enters the channel from a north to north-westerly direction. Some influence of refraction is observed in the wave direction but not much directional spreading is seen. SWAN simulates that part of the wave energy enters the channel mouth to the west of the ebb-tidal delta and bends around the delta due to refraction. This wave energy has a westerly direction.

In the observations however, the directional distribution of the wave energy has only one peak with an evenly distribution on both sides. However, some of the differences in directional wave distribution between the measured and computed wave energy can be directly related to features in the geometry and the resulting effect of nonlinear wave interactions. As explained in Groeneweg et al. (2014b) nonlinear wave interactions cause directional broadening of the wave energy spectrum. As a consequence, more wave energy will be able to enter the channel. For example, the wave energy that propagates over the tidal flat west of RZGN1 is able to reach RZGN1 in the measurements and not in the SWAN computations. Non-linear interactions that cause the directional broadening are not modelled in SWAN.

Consequences for the Eems Dollard estuary
In the analysis of the Eems Dollard estuary it was seen that low-frequency wave energy for north to north-westerly storms is able to penetrate into the estuary quite deeply due to the open geometry of the estuary. Buoy UHW1 was located very close to the coast and it could be seen that a H_{10} of about 50 centimetres does occur during certain storms. Striking was that the more north-westerly November 2007 storm could penetrate better into the estuary than the more northerly December 2013 storm. Furthermore, during the November 2007 storm the H_{10} was underestimated for all hindcast moments, whereas this was not the case during the December 2013 storm.

Differences can probably be explained by the difference in incident wave direction, but also by a difference in water levels. Refraction on the ebb-tidal delta or tidal flats is different for different wave angles and different water levels. Moreover the wave direction can be smaller or larger than the critical angle for refraction and therefore determine the amount of penetration of energy into or across a channel. Also the water level influences the pattern when the low-frequency waves are underestimated, since for lower water levels the nonlinear interactions are stronger. Additionally, a lower water level causes also more refraction on the ebb-tidal delta and therefore wave energy penetrates the inlet from a different wave direction than the incident wave direction.

5 Conclusions, discussion and recommendations

5.1 Conclusions

For the Western Scheldt delta, the Amelander Zeegat and the Eastern Wadden Sea, for many instances a mismatch between measured and computed swell energy is observed in the tidal inlet gorge. Whether or not the low-frequency wave energy is underestimated by SWAN is to a large extent determined by the local geometry. For all three areas, cases were found where differences could be explained by the hypothesis of Groeneweg et al. (2014a,b). This hypothesis is further discussed in Section 5.2. In those cases the waves first propagated over the ebb-tidal delta or tidal flats and subsequently came across a channel. From the 1D and 2D spectra it was seen that the observed waves could enter or cross the channel, whereas the computed waves were refractively trapped to the channel edges.

Western Scheldt

For the Western Scheldt the most important conclusions from the analysis are that no underestimation of the low-frequency energy, in terms of H_{15}, was seen for almost all cases when the waves come from the West, as the wave direction is parallel to the channel. However, SWAN underestimates the low-frequency energy at SCHO and WIEL, when waves come from north to north-westerly directions. From the spatial plots it was concluded that refraction over the ebb-tidal delta and/or on the channel edges plays an important role for the north-westerly wave directions. Additionally, for the north to north-westerly directions, where the waves propagate over the shoal, we observed that the computed low-frequency energy is often underestimated at SCHO and WIEL. This can be explained by the hypothesis of Groeneweg et al. (2014b). In reality the wave energy spectrum broadens directionally due to nonlinear wave interactions and waves attack the channel under angles that are not refractively trapped. SWAN does not contain a mechanism that leads to directionally broader wave spectra, as discussed in Section 5.2.

Amelander Zeegat

In the Amelander Zeegat there exists a strong correlation between the underestimation of H_{10} and the geometry (channel orientation and location of tidal flats). A clear dependency of the computed underestimation of H_{10} was observed on the water depth, the peak wave direction and the offshore wave direction, especially for some locations (AZB21 and AZB31, as located in 2007). For buoy AZB31, as located in 2013 in the main channel, 2D wave spectra of the measurements and SWAN showed that no wave energy propagates from the tidal flat (west of location AZB31) into the main channel, whereas there was a westerly directed component in the observed 2D spectra. This effect is due to the refraction of the directionally-narrower spectra in SWAN, see Groeneweg et al. (2014b) and the discussion in Section 5.2. Finally, for location AZB32, no clear patterns could be observed. The main problem for this location seems to be that the low-frequency energy is overestimated by SWAN for most hindcast moments.

Eastern Wadden Sea

The conclusions for the Eems Dollard estuary in the Eastern Wadden Sea are that no clear dependency of the computed underestimation of H_{10} was observed on the water depth or the peak wave direction. The 2D wave spectra of the December 2013 storm showed that the directional wave energy distribution at the wave buoys is often different in the observed spectra than in SWAN. Some of the differences in directional wave distribution between the measured and computed wave energy can be directly related to features in the geometry and

the resulting effect of nonlinear wave interactions (as explained in Groeneweg et al. (2014b) and briefly in Section 5.2). As a consequence, more wave energy will be able to enter the channel. For example, the wave energy that propagates over the tidal flat west of RZGN1 is able to reach RZGN1 in the measurements and not in the SWAN computations.

5.2 Discussions on the observed patterns

Groeneweg et al. (2014a, 2014b) provided an explanation for the observation that observed waves can enter or cross the channel, whereas the computed waves are refractively-trapped to the channel edges. In reality the 2D nonlinear interactions broaden the directional range of the energy density spectrum in situations where the waves propagate over an ebb-tidal delta or tidal flats. In particular subharmonic wave interactions between the second harmonic and basic component generate a wave component of the same frequency as the primary component but at a wider angle of approach. As a consequence, the energy density spectra become directionally broader and this leads to wave components propagating towards the channel under different angles. The directional broadening of the spectrum therefore results in more energy at angles smaller than the frequency dependent critical angle for refraction and thus more wave energy is transmitted into and across channels. However, SWAN only accounts for co-linear three-wave interactions to the higher harmonics. This 1D approach does not have the ability to broaden the directional range of the energy density spectrum.

Various aspects affect the amount of wave energy penetrating from tidal flats into and across tidal channels, and eventually towards the dike of the estuaries. The incident wave direction (and thus wind direction) is clearly of influence in this process. Refraction on the ebb-tidal delta or tidal flats is different for different wave angles. Moreover the wave direction can be smaller or larger than the critical angle for refraction and therefore determine the amount of penetration of energy into or across a channel. Also the water level influences the pattern when the low-frequency waves are underestimated. For lower water levels the nonlinear interactions are stronger. Additionally, a lower water level causes also more refraction on the ebb-tidal delta and therefore wave energy penetrates the inlet from a different wave direction than the incident wave direction. On the other hand, a lower water depth leads to more dissipation of the low-frequency energy, due to bottom friction and wave breaking.

However, not all cases where the low-frequency wave energy is underestimated by SWAN can be explained by the theory of Groeneweg et al. (2014a, 2014b). In some cases differences between observations and computations are already encountered at the offshore wave boundary (see Western Scheldt and Eastern Wadden Sea). In addition, for some cases strong currents could have influenced the spectral shape. Of course also other inaccuracies in the SWAN numerics and physics, which have not been identified in this study, could have played a role.

5.3 Discussions on the wave conditions near the flood defences

For the storms that have been analysed in this study, the low-frequency wave energy penetration was limited for the Western Scheldt and the Amelander Zeegat. For both areas, a large amount of low-frequency wave energy is dissipated on the ebb-tidal delta. For those areas the impact of the underestimation of low-frequency energy by SWAN is probably highest at the coast adjacent to the inlet (e.g. the coast of Zeeuws-Vlaanderen or the headland of Ameland). While for the measured storms, the amount of low-frequency energy penetration was small, this is not necessarily the case for normative conditions, as the water level is much higher then, and the mainland coast may be subject to low-frequency waves.

The Eems Dollard estuary is very open and it was seen that a large amount of low-frequency wave energy could penetrate towards the coast in the measured storm conditions, and even more so for normative conditions. For the dikes of Groningen and inside the Eems Dollard channel, it is very likely that the low-frequency wave energy is underestimated for north to north-westerly storms. Only for these storms the water levels are high enough for swell waves to reach the mainland.

5.4 Recommendations

Clearly SWAN underestimates the swell wave penetration into estuaries. Since there are many factors that determine the reliability of the SWAN results in the database that is used for the determination of Hydraulic Boundary Conditions, it is impossible to define a generic concept to correct the SWAN results for the observed underestimation of low-frequency wave energy. The best option is to indicate certain areas where the SWAN output data are suspicious. At the coast of Zeeuws-Vlaanderen, the headland of the Wadden Sea islands and in front of the dikes in the Eems-Dollard estuary the SWAN results for the more energetic conditions, i.e. strong winds from the north-west to northern sector should be treated with care. Unfortunately north-west to northern wind directions lead to normative conditions and are therefore relevant for the Hydraulic Boundary Conditions and resulting safety assessment.

As was also recommended in Groeneweg et al. (2014a, 2014b) the formulations for three-wave interactions in SWAN should be adapted as soon as possible. This is however a tedious task that requires the effort from institutions like Delft University of Technology.

The 2D measured spectra and radar data proved to be very useful in the analysis and understanding of wave penetration into tidal inlets. It is recommended to make more use of these possibilities in the future.

While storms are rare, the information they provide is very valuable. There is no other source of reliable data for large storm conditions. We therefore recommend continuing the measurement program in the Wadden Sea and Zeeland estuaries.

Deltares

6 References

Alkyon (2007a). Analysis SWAN hindcast tidal inlet of Ameland. Storm events of 8 February 2004 and 2, 8 January 2005. ref A1725R4, February 2007.

Alkyon (2007b). Analysis SWAN hindcast tidal inlet of Ameland. Storms of 17 December 2005 and 9 February 2006. ref A1725R5, February 2007.

Alkyon (2008). SWAN hindcast in the Eastern Wadden Sea and Eems-Dollard estuary, storm of 9 November 2007. ref A2191, December 2008.

Alkyon (2009). Analysis of wave penetration into the eastern Wadden Sea. Alkyon report A2302, June 2009.

Booij, N., R.C. Ris and L.H. Holthuijsen. 1999. A third generation wave model for coastal regions, Part I, Model description and validation, J. Geophys. Res., 104, C4, 7649-7666.

Borsboom, M.J.A., N. Doorn, J. Groeneweg and M.R.A. van Gent (2000). A Boussinesq-type model that conserves both mass and momentum. In Proc. 27th Int. Conf. on Coastal Engng, Sydney, 148-161.

Bouws, E. and G. J. Komen (1983). On the balance between growth and dissipation in an extreme, depth-limited wind-sea in the southern North Sea. J. Phys. Oceanogr., 13, 9, 1653-1658.

Deltares/Alkyon (2009). Wave propagation through tidal inlet systems. Deltares report 1200114-002-HYE-0006, October 2009.

Deltares (2011a). Projectplan 2011 SBW – Hydraulische Belastingen. Deltares rapport 1203757-000-HYE-0007, Februari 2011.

Deltares (2011b). Improvements in spectral wave modelling in tidal inlet seas: overview of results of the SBW-Waddenzee project 2006-2010. Deltares report 1202119-006-HYE-0003, May 2011.

Deltares (2011c). Hydra-Ring Design Document, version 2.2. Technical report, Deltares (A. Markus, H. Steenbergen and R. Brinkman).

Deltares (2012). Twee-dimensionale golfspectra. SBW Informatiebehoefte, Veldmetingen en Data. Deltares report 1206019-003-HYE-0008, September 2012.

Deltares (2013a). Projectplan cluster Hydraulische Belastingen, Deltares report 1207807-000-HYE-0001, Januari 2013.

Deltares (2013b). Hydra-Ring Scientific Documentation. Technical report, Deltares (F. Diermanse, K. Roscoe, J. Lopez de la Cruz, H. Steenbergen and A. Vrouwenvelder).

Deltares (2013c). Quantifying uncertainties of SWAN results. Deltares report 1206011-002HYE-0001. February 2013.Deltares (2014). SWAN hindcasts Wadden Sea, December 2013. Tidal inlet of Ameland and eastern Wadden Sea. Deltares report 1209433-007-HYE-0005 - draft, July 2014.

Eldeberky, Y. (1996). Nonlinear transformation of wave spectra in the nearshore zone. Ph.D. thesis, TU Delft, 203 pp.

Eslami S. A., A. van Dongeren, P. Wellens (2012). Studying the effect of linear refraction on low-frequency wave propagation (physical and numerical study). In Proceedings of the International Conference on Coastal Engineering, Santander.

Gautier, C. and J. Groeneweg (2012). The use of spatial radar observations in wave hindcasts. Coastal Engineering Proceedings, [S.l.], n. 33, p. waves.42, oct. 2012. ISSN 2156-1028.

Groeneweg, J., M. van Gent, J. van Nieuwkoop and Y. Toledo (2014a). Wave propagation into coastal systems with complex bathymetries. Submitted for publication.

Groeneweg, J., J. van Nieuwkoop and Y. Toledo (2014b). On the modelling of swell wave penetration into tidal inlets. In Proceedings of the International Conference on Coastal Engineering, Seoul, Korea.

Hasselmann, S., K. Hasselmann, J. A. Allender, and T. P. Barnett (1985). Computations and parameterizations of the nonlinear energy transfer in a gravity-wave spectrum. Part 2: parameterization of the nonlinear transfer for application in wave models, J. of Phys. Oceanogr. 15, 1378-1391.

Herbers, T. H. C., S. Elgar, and R. T. Guza (1995), Generation and propagation of infragravity waves, J. Geophys. Res., 100 (C12), 24863–24872, doi:10.1029/95JC02680.

Royal Haskoning (2008). Hindcast tidal inlet of Ameland storms January and March 2007. Royal Haskoning Report 9T5842.A0, October 2008.

Toledo, Y. (2013). The oblique parabolic equation model for linear and nonlinear wave shoaling. J. Fluid Mech. 715, 103-133. Toledo, Y. and Y. Agnon (2012). Stochastic evolution equations with localized nonlinear shoaling coefficients. *European Journal of Mechanics B/Fluids*, vol. 34, 13–18.

Van der Westhuysen, A. J., M. Zijlema, and J. A. Battjes (2007). Nonlinear saturation-based whitecapping dissipation in SWAN for deep and shallow water. Coastal Engineering 54, 151-170.

Van der Westhuysen, A. J. (2007). Advances in spectral modelling of wind waves in the nearshore. PhD thesis. Fac. of Civ. Eng., Delft Univ. of Technology, Delft, The Netherlands, 207pp.

Van der Westhuysen, A. J. (2009), Modelling of depth-induced wave breaking over sloping and horizontal beds. 11th International Workshop on Wave Hindcasting and Forecasting 2009 (pp 1-10).

Van der Westhuysen, A. J. (2010), Modeling of depth-induced wave breaking under finite depth wave growth conditions. Journal of Geophysical Research, Vol. 115, C01008, 2010.

Van der Westhuysen, A. J. (2011). Spectral modeling of wave dissipation on negative current gradients. *Submitted to J. Geophys. Res.*

Van der Westhuysen, A. J., A. R. van Dongeren, J. Groeneweg, G. Ph. van Vledder, H. Peters, C. Gautier and J. C. C. van Nieuwkoop (2012). Improvements in spectral wave modeling in tidal inlet seas. *J. Geophys. Res.*, **117**, doi:10.1029/2011JC007837.

Wenneker, I., Kieftenburg, A.T.M.M. Westhuysen, A.J. van der and L. Verhage (2009). SWIVT, an instrument for validation and testing of SWAN . Coastal Engineering 2008: proceedings of the 31st international conference (Hamburg, 13 August - 5 September 2008), vol. 1 ; p. 509-520

Wenneker, I., Smale A. (2013). Measurement of 2D wave spectra during a storm in a tidal inlet. Coastal Dynamics 2013: proceeding of the 7th international conference (Bordeaux, 24-28 June 2013), p. 1905-1914.

Witteveen+Bos (2010): Hindcast verification of SWAN in the Western Scheldt. ref DT311-1, March 24 2010.

Witteveen & Bos (2008). Hindcast of the 8 and 9 november 2007 storm for the tidal inlet of Ameland. DT293-2/winb/011, November 2008.

WL & Alkyon (2007). Storm hindcast for Wadden Sea, Hindcasts in inlet systems of Ameland and Norderney and Lunenburg Bay. WL | Delft Hydraulics Report H4918.20, September 2007

Zijlema, M., van Vledder, G. Ph., Holthuijsen, L. H (2012). Bottom friction and wind drag for wave models. Coastal Engineering Volume 65, July 2012, Pages 19–26

A Important concepts

Low frequency significant wave height
The low frequency significant wave height is the significant wave height, related to the energy at frequencies smaller than an upper frequency bound. The upper frequency bound is chosen by examining the most occurring peak frequency at a certain study area. As the energy of second harmonic interactions could interfere with the conclusions, the upper bound is chosen in a way that the upper bound is lower than the frequency of the second harmonic. Depending on the area an upper frequency bound of 0.10 Hz (Wadden Sea) or 0.15 Hz (Western Scheldt) is chosen. The low frequency significant wave height (H_{lf}) is calculated as follows:

$$H_{lf} = 4\left(\int_0^{lfl} E(f)df\right)^{1/2} \quad eq.\,A.\mathbf{1}$$

Where lfl is the low frequency limit, which is 0.10 or 0.15 Hz in this report, E(f) is the one-dimensional frequency spectrum and f the frequency.

Peak wave direction
In this report three different concepts are used to define the wave direction of the low-frequency waves. These concept are illustrated by an example, see Figure A.1.
*   1.5D peak wave direction
    The 1.5D peak wave direction is defined as the direction at the frequency where the 1.5D wave energy spectrum reaches its maximum. In the 1.5D wave energy spectrum the variance density, mean direction and directional spreading are given for each frequency bin, see Figure A.1.

    The advantage of the 1.5D peak wave direction is that the frequency peak is often close to 0.1 Hz for the locations that where considered. For locations further into the tidal inlet, where local generated waves become more important than the incoming swell or when triads transfer a large amount of energy to the second harmonic, the results, where this peak wave direction is involved, should be interpreted with care. For this frequency the mean wave direction is taken. As the energy is usually spread over different directions, the mean seems to be more reliable than the peak. Figure A.1 illustrates this well. However, it should be considered in this analysis that the wave energy could be present at two distinct energy peaks. The 1.5D peak wave direction does not give a useful answer in this case.

*   SWAN peak wave direction
    The peak wave direction according to the definitions of SWAN is the direction where the directional distribution $E(\theta) = \int E(\omega, \theta)d\omega$ is maximum, see Figure A.1. Here E(ω,θ) is the two-dimensional variance density spectrum, with ω the angular frequency and θ the direction. This parameter is one of the output options in SWAN and is available in the different SWAN hindcasts.
    As we are interested in the low-frequency energy, the SWAN peak wave direction has the drawback that it takes the peak where the sum of wave energy over all frequencies is highest. This means that if a large windsea component is present, this can influence the results. Furthermore, if the directional distribution is not very uniform, the SWAN

peak wave direction does not give a good picture of the direction, as is seen in Figure A.1.

- Dominant wave direction
  The dominant wave direction is the direction of the energy bin with maximum energy as function of direction and frequency ($E(\omega, \theta)$). In the case of Figure A.1 it is the same as the SWAN peak wave direction. However, it can happen that one wave energy peak exists at one direction, that is larger than all other peak, but that the sum of wave energy at a different direction is larger than this peak. In that case, the SWAN peak wave direction does present better where most wave energy is. In general, this parameter has the same drawbacks as the 1.5D peak wave direction and the SWAN peak wave direction combined.

From this overview it can be conclused that none of these parameters are perfect ways to characterize from which direction the wave energy is coming. This should be kept in mind when analysing the results.
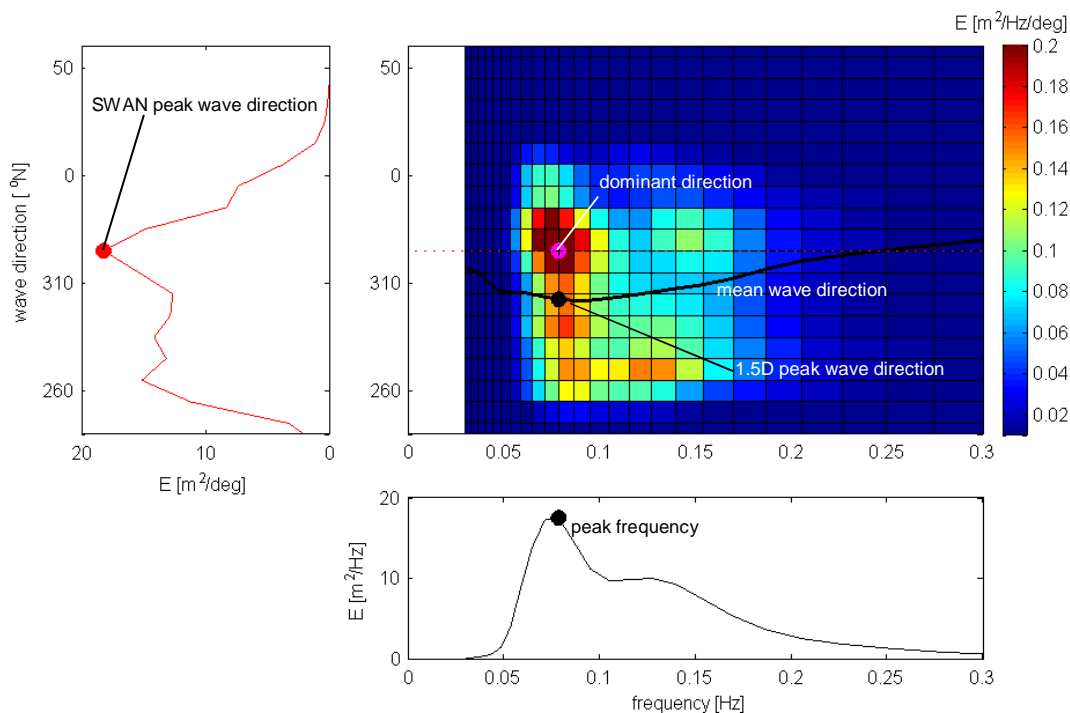
Figure A.1 Illustration of different ways to define the wave direction. The main figure shows the 2D wave energy density spectrum with the mean wave direction as a function of frequency on top. The directional distribution of this spectrum is show in the left figure; the frequency distribution is shown in the bottom figure. The 1.5D peak frequency and wave direction are indicated with a black dot, the SWAN peak wave direction is indicated with a red dot and the dominant wave direction with a pink dot.

B Figures Western Scheldt
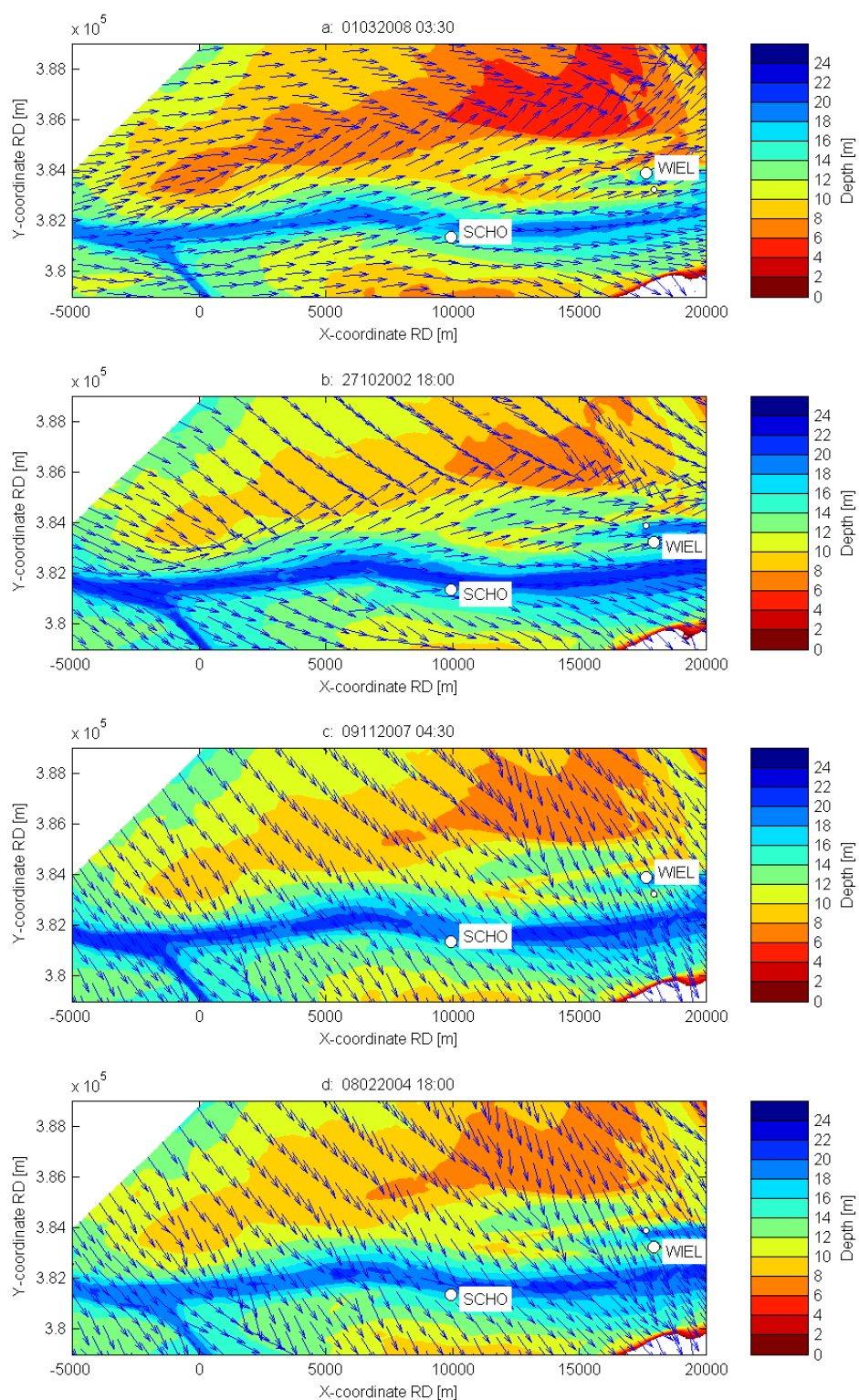
Figure B.1 Spatial distribution of the SWAN peak wave directions and total water depth for hindcast moments: a) 01-03-2008 03:30, b) 27-10-2002 18:00, c) 09-11-2007 04:30.
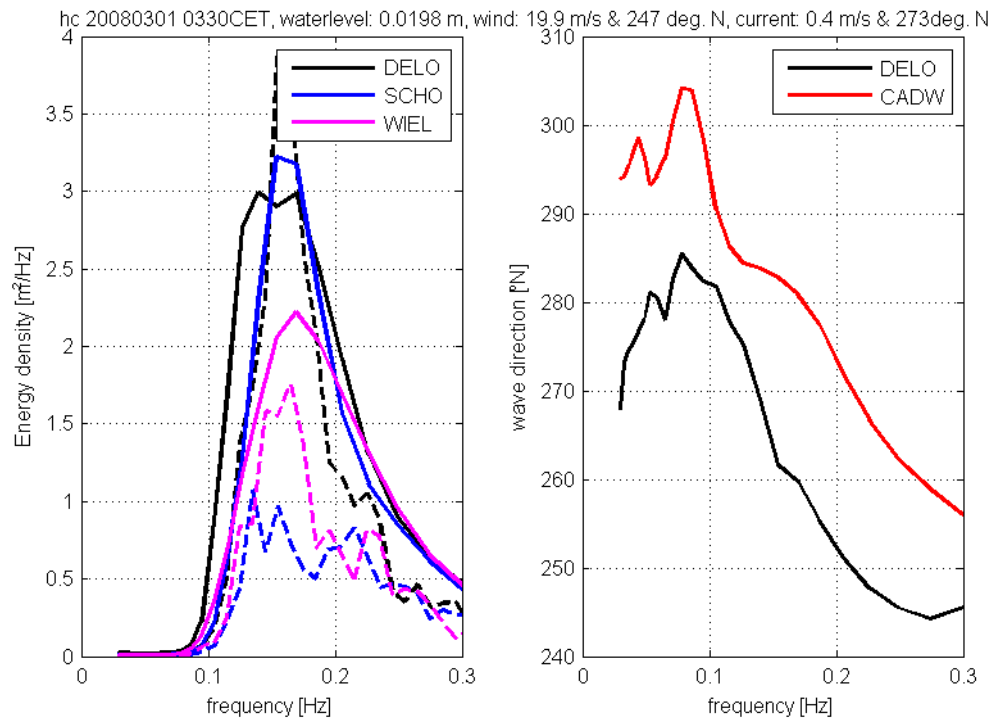
Figure B.2   1D spectrum and wave direction of DELO, SCHO, WIEL and CADW for 01-03-2008 03:30, SWAN results are shown with the solid lines, observations with the dashed lines
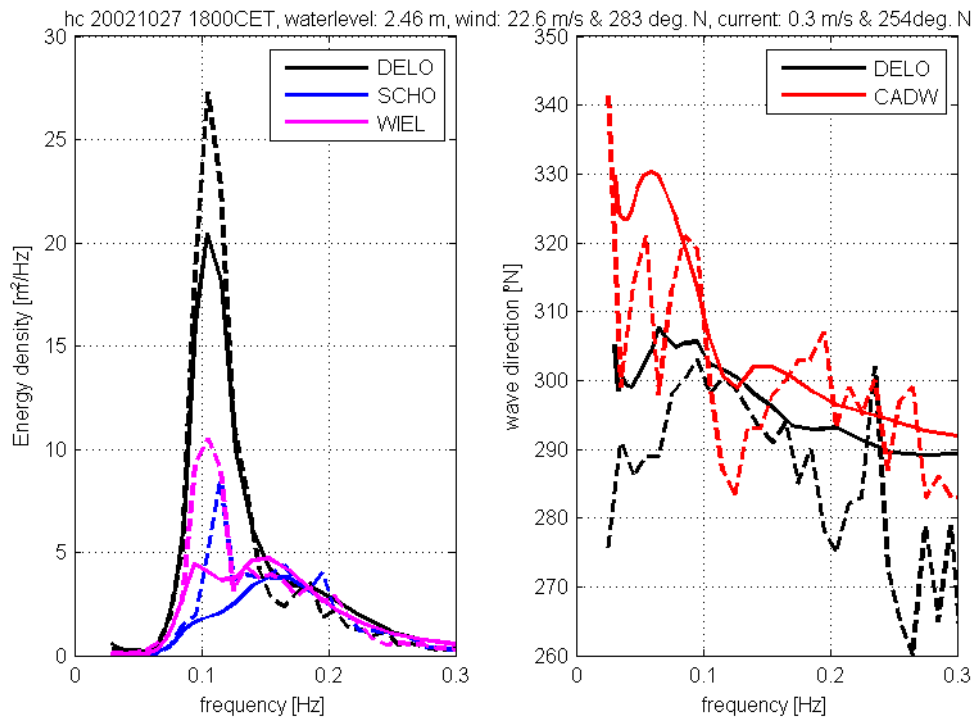
Figure B.3   1D spectrum and wave direction of DELO, SCHO, WIEL and CADW for 27-10-2002 18:00, SWAN results are shown with the solid lines, observations with the dashed lines
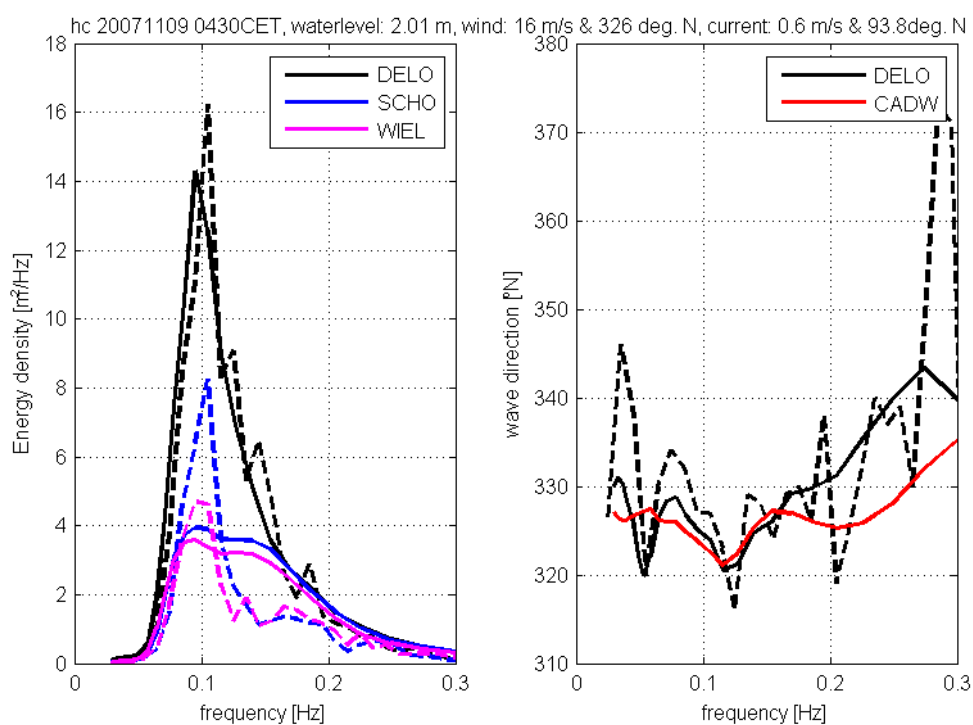
Figure B.4   1D spectrum and wave direction of DELO, SCHO, WIEL and CADW for 09-11-2007 4:30, SWAN results are shown with the solid lines, observations with the dashed lines
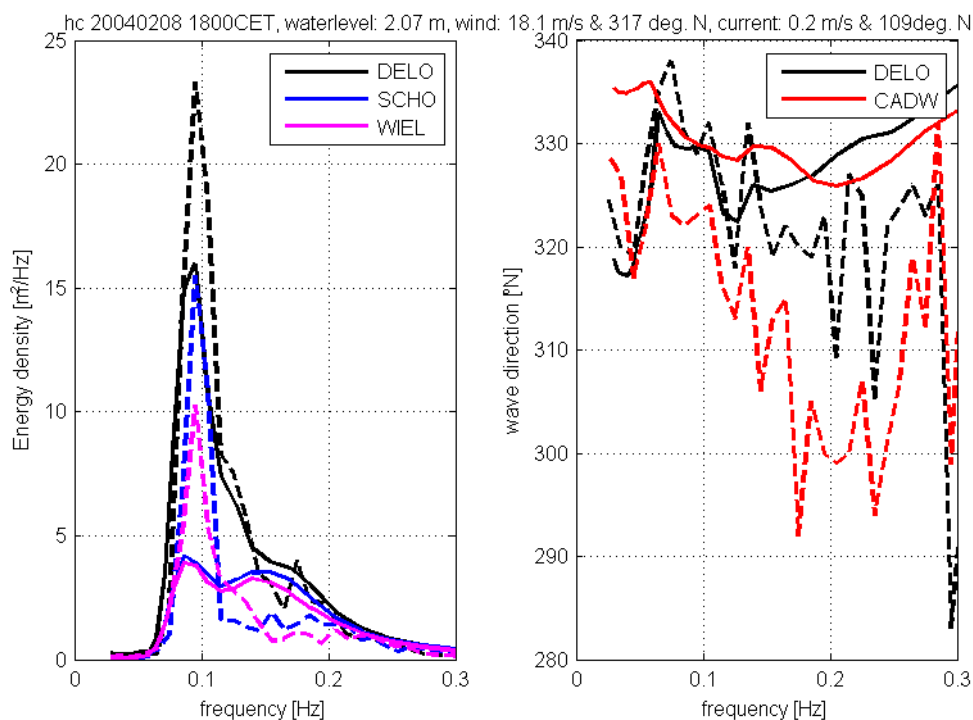
Figure B.5   1D spectrum and wave direction of DELO, SCHO, WIEL and CADW for 08-02-2004 18:00, SWAN results are shown with the solid lines, observations with the dashed lines

C Figures Amelander Zeegat
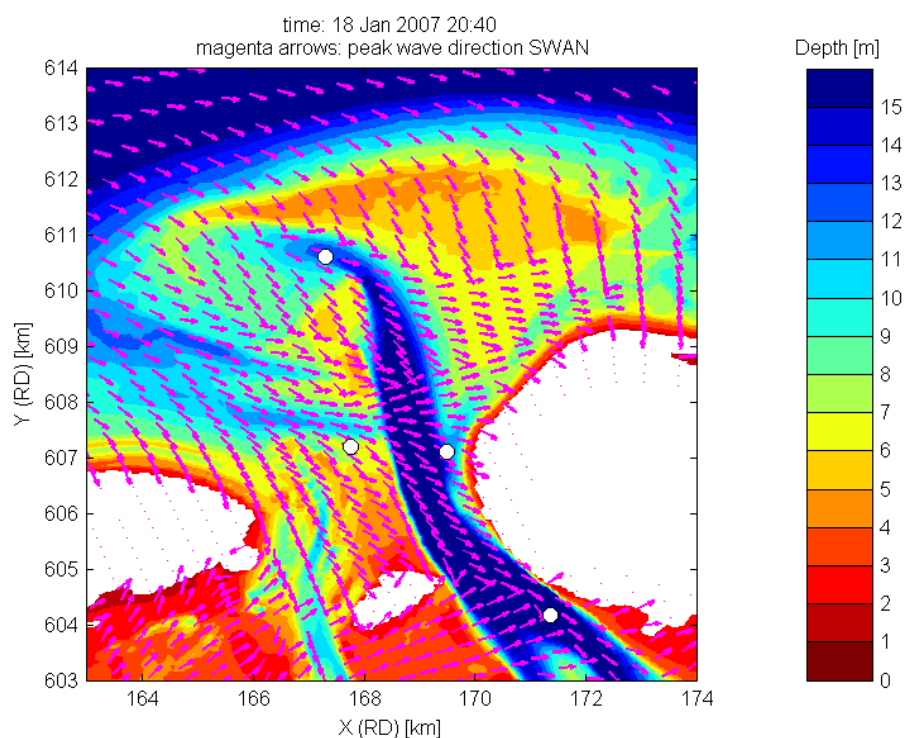
Figure C.1 Spatial distribution of the SWAN peak wave direction (pink arrows) and total water depth for hindcast moment 18-01-2007 20:40, incident wave direction (SWAN peak wave direction at AZB11): 285 °N.
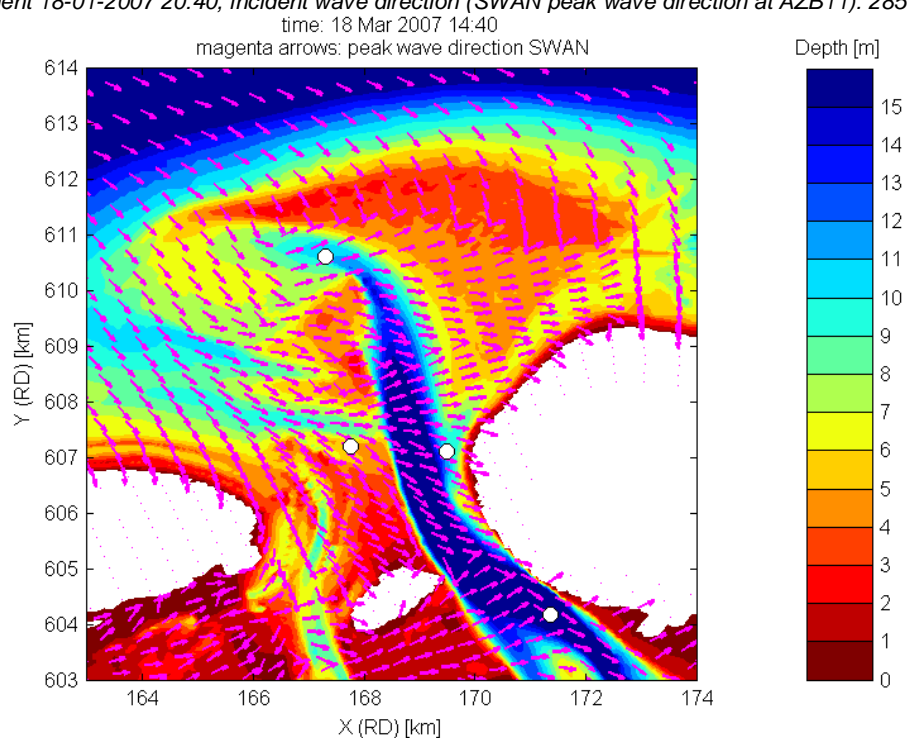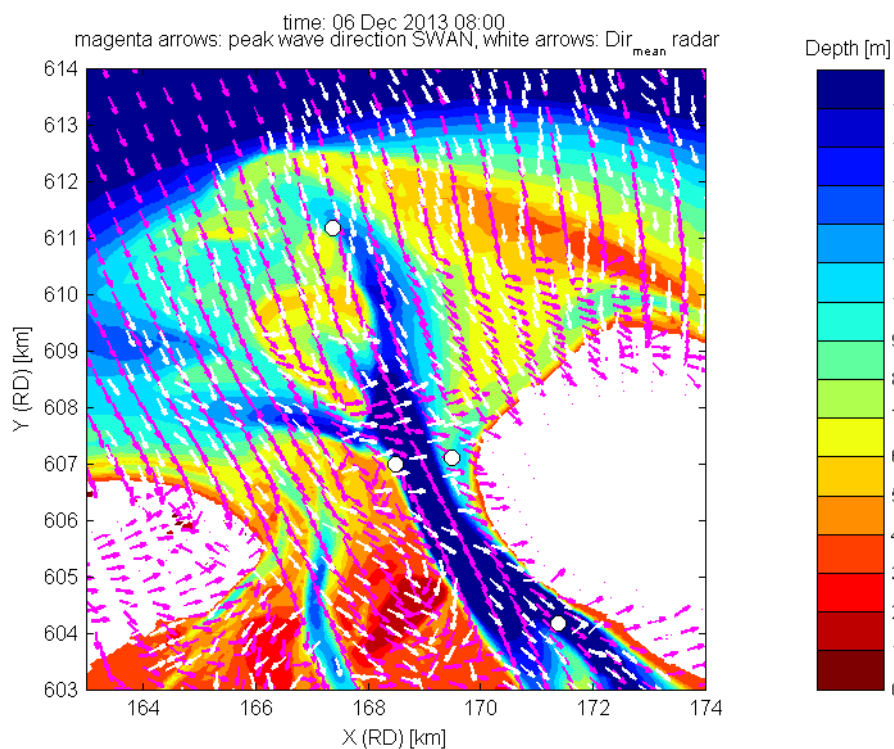

Figure C.2 Spatial distribution of the SWAN peak wave direction (pink arrows) and total water depth for hindcast moment 18-03-2007 14:40, incident wave direction (SWAN peak wave direction at AZB11): 290 °N.
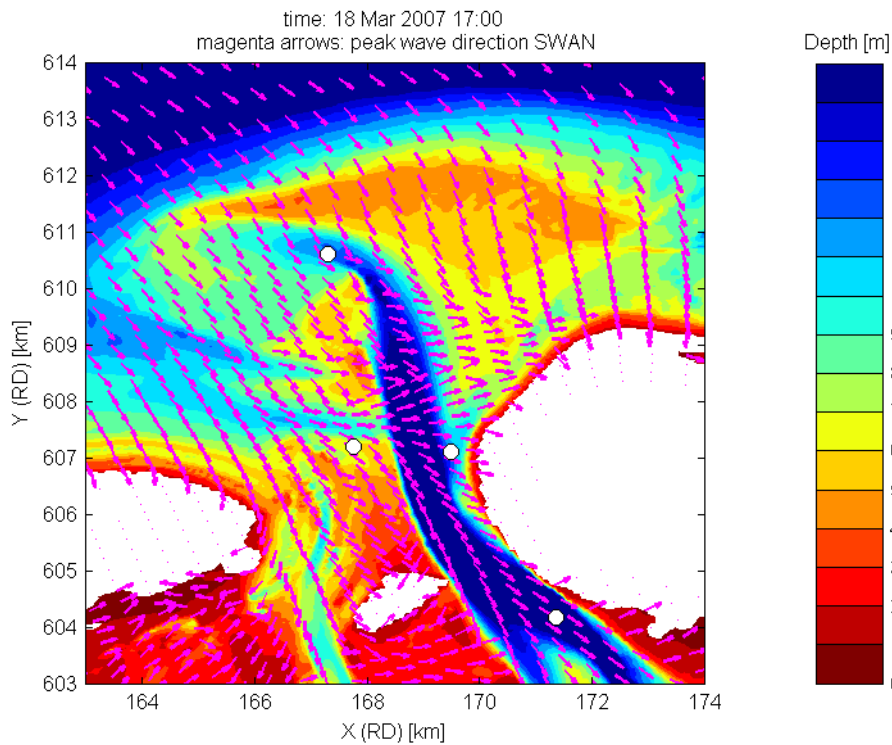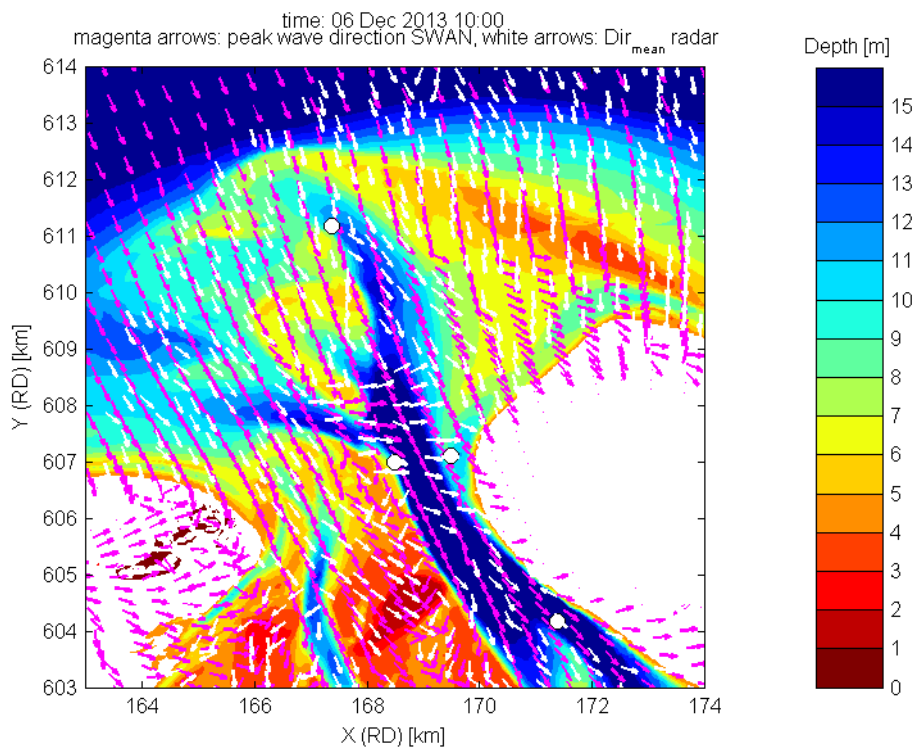
*Figure C.3 Spatial distribution of the SWAN peak wave direction (pink arrows) and total water depth for hindcast
moment 18-03-2007 17:00, incident wave direction (SWAN peak wave direction at AZB11): 297 °N.*
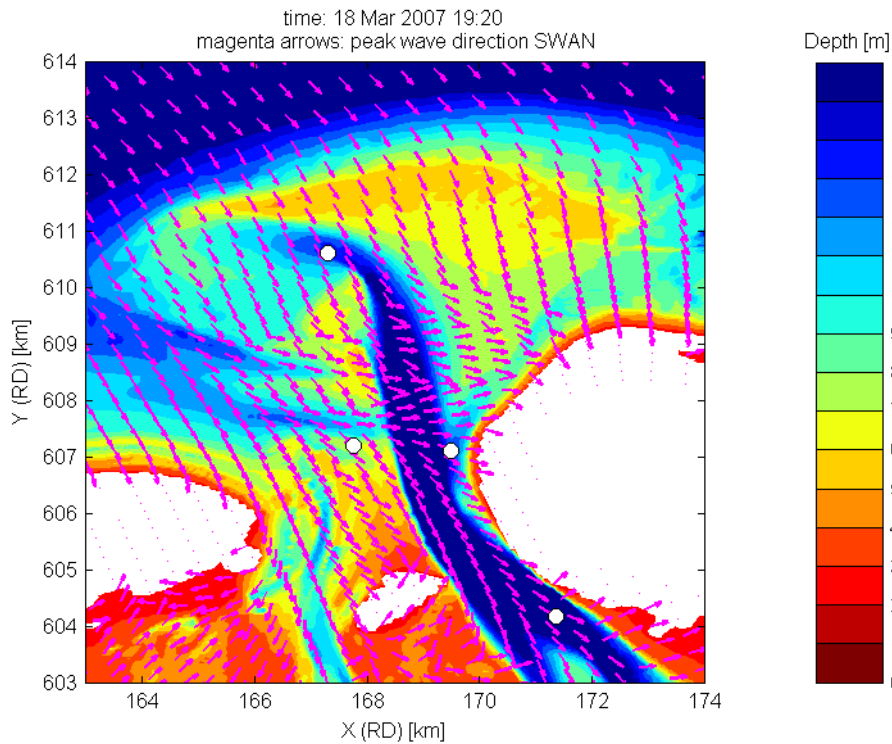
*Figure C.4 Spatial distribution of the SWAN peak wave direction (pink arrows) and total water depth for hindcast
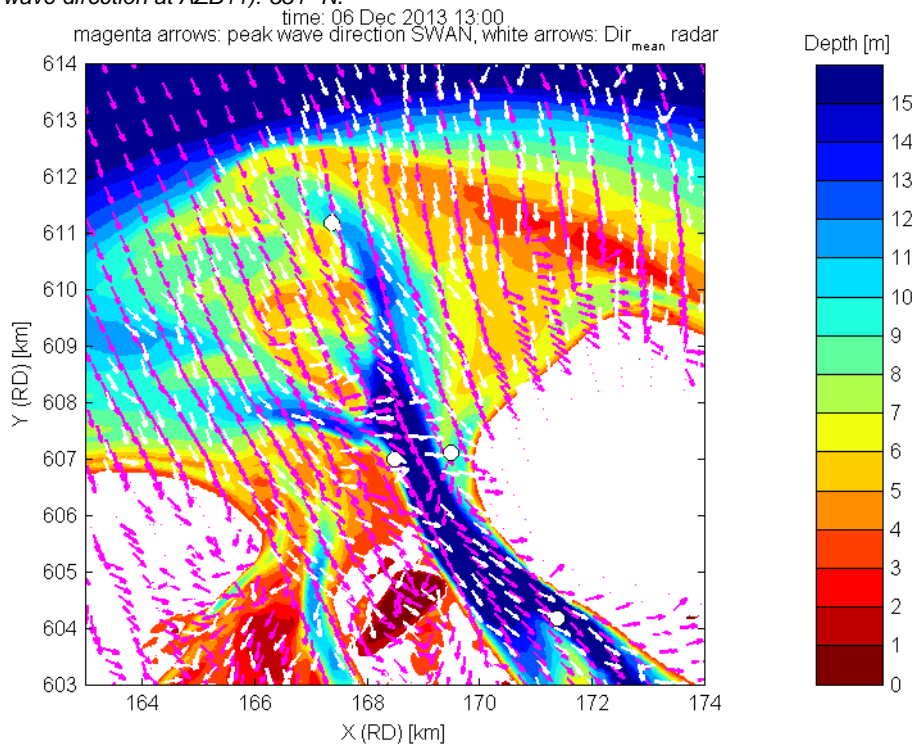moment 18-03-2007 19:20, incident wave direction (SWAN peak wave direction at AZB11): 301 °N.*
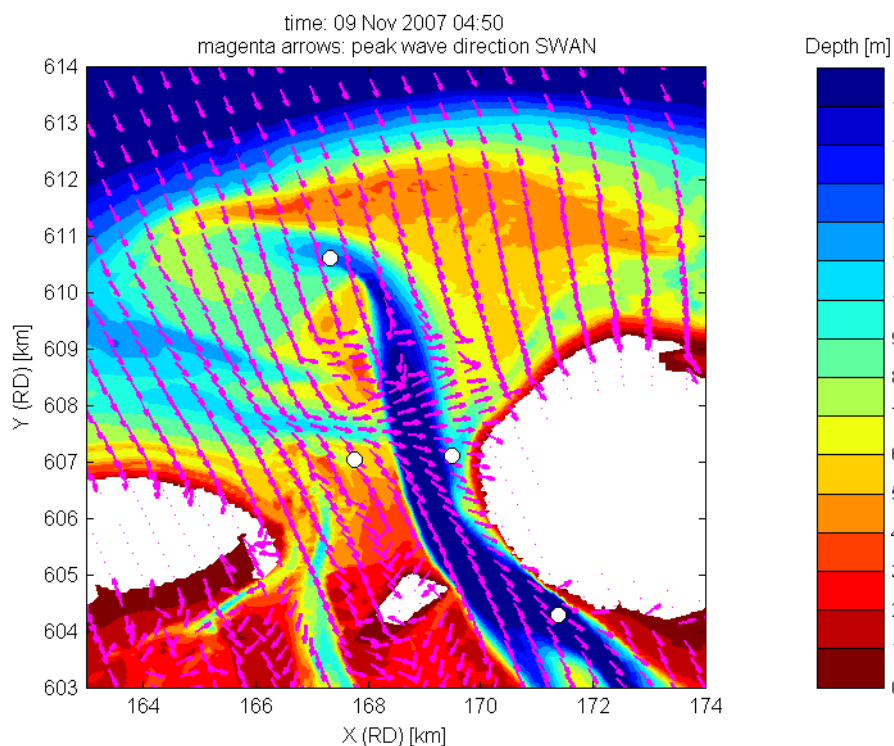
Figure C.5 Spatial distribution of the SWAN peak wave direction (pink arrows) and total water depth for hindcast moment 9-11-2007 4:50, incident wave direction (SWAN peak wave direction at AZB11): 329 ^{o}N.
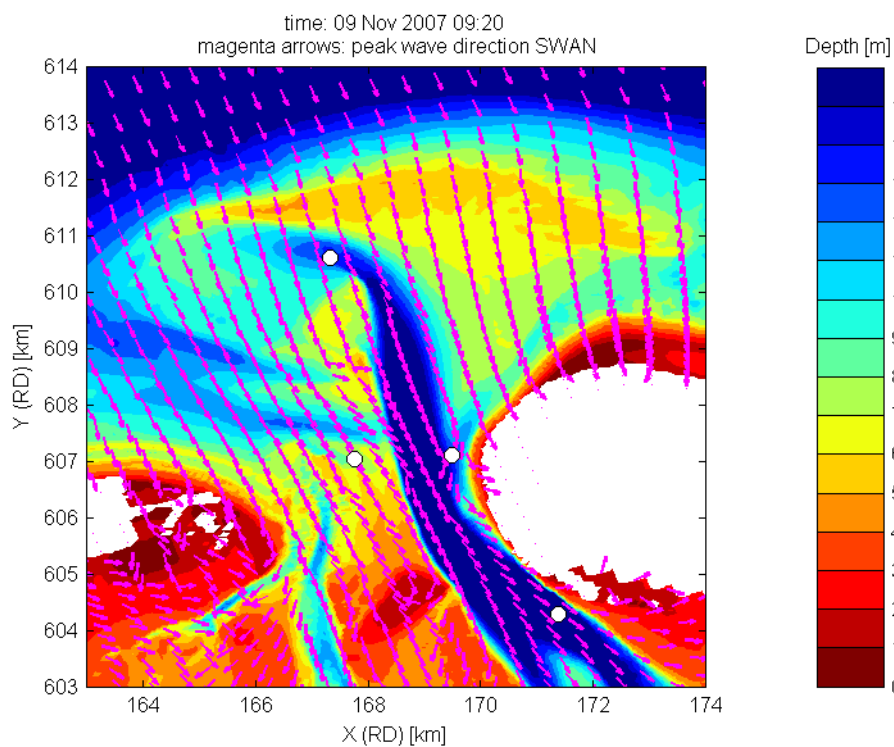
Figure C.6 Spatial distribution of the SWAN peak wave direction (pink arrows) and total water depth for hindcast moment 9-11-2007 9:20, incident wave direction (SWAN peak wave direction at AZB11): 335 ^{o}N.
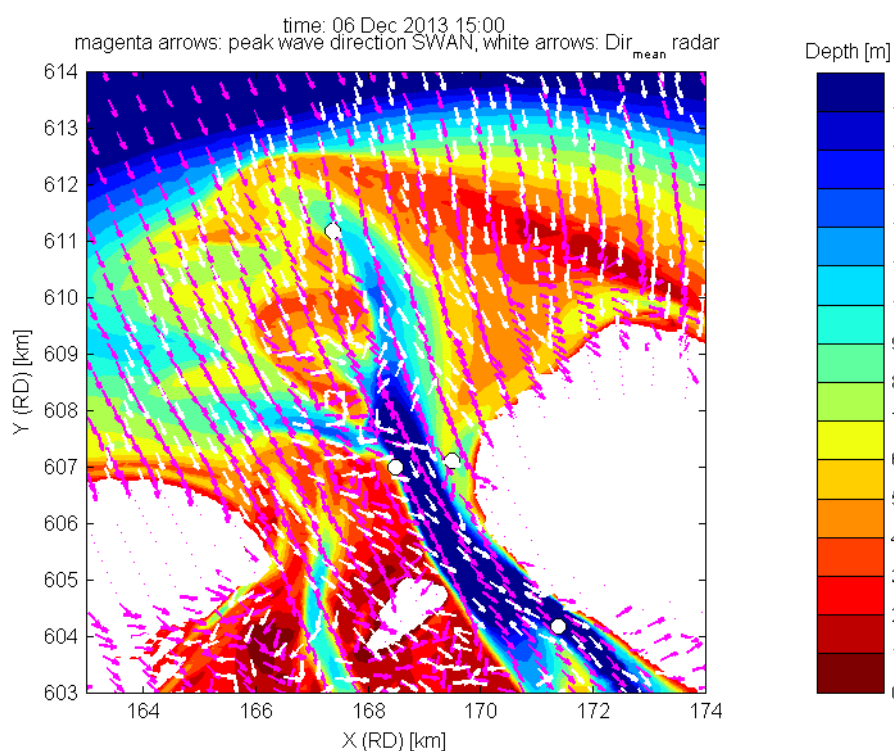
ffffffffff

fff

fff

ffffffffffffff

fffff
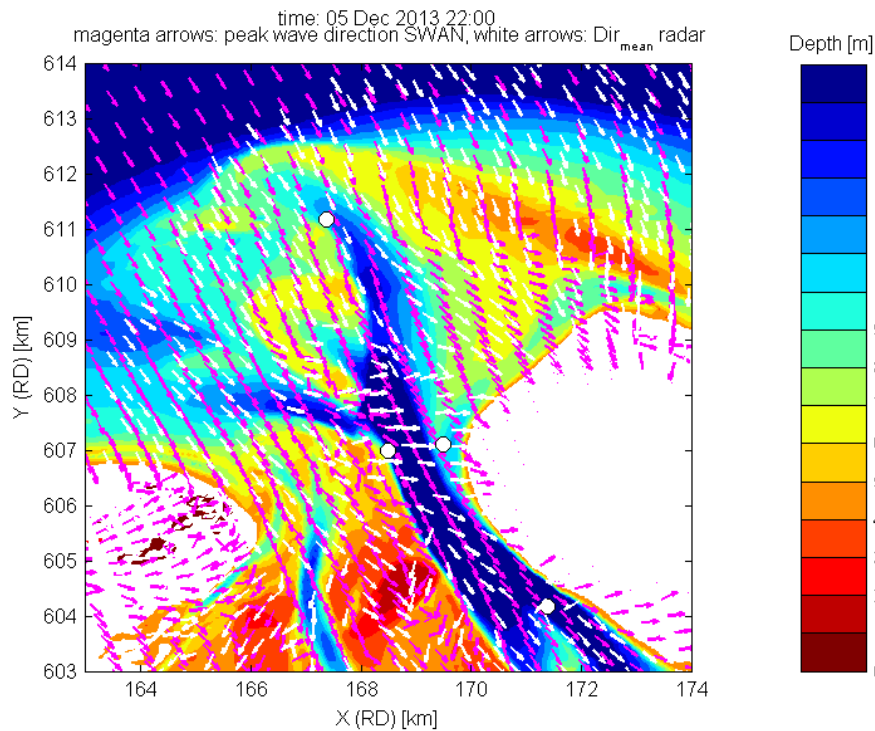
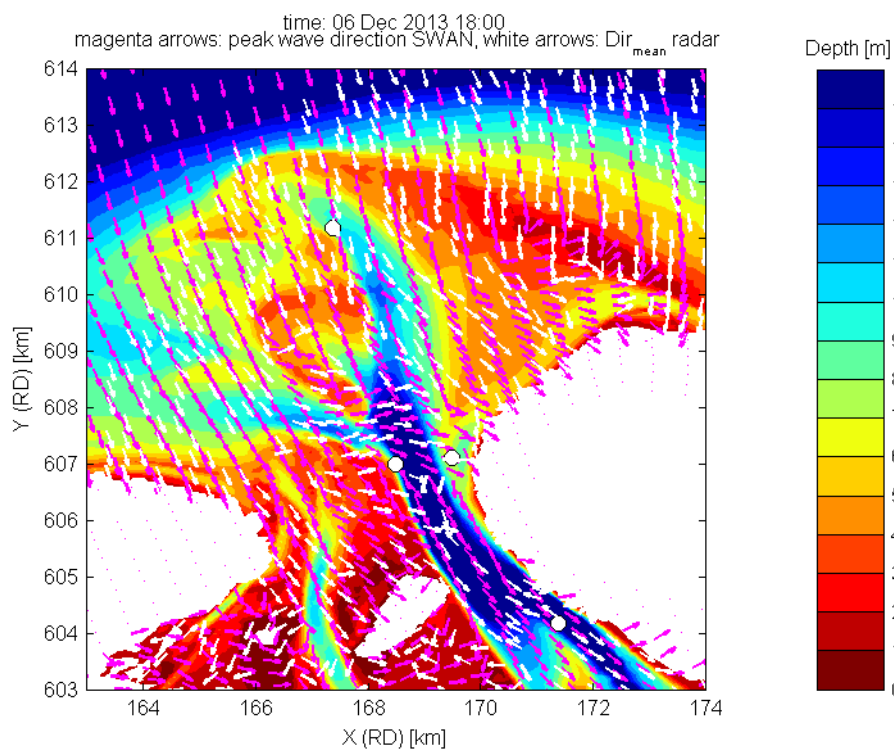Figure C.7 Spatial distribution of the SWAN peak wave direction (pink arrows), the radar dominant wave directions (white arrows) and total water depth for hindcast moment 5-12-2013 22:00, incident wave direction (SWAN peak wave direction at AZB11): 319 °N.
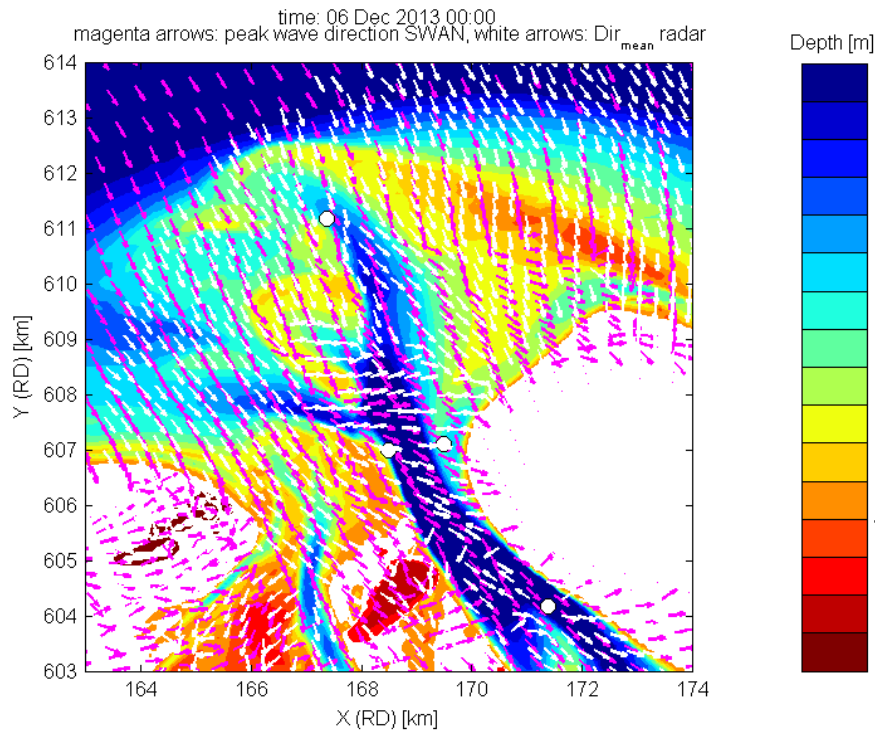
Figure C.8 Spatial distribution of the SWAN peak wave direction (pink arrows), the radar dominant wave directions (white arrows) and total water depth for hindcast moment 6-12-2013 00:00, incident wave direction (SWAN peak wave direction at AZB11): 325 °N.
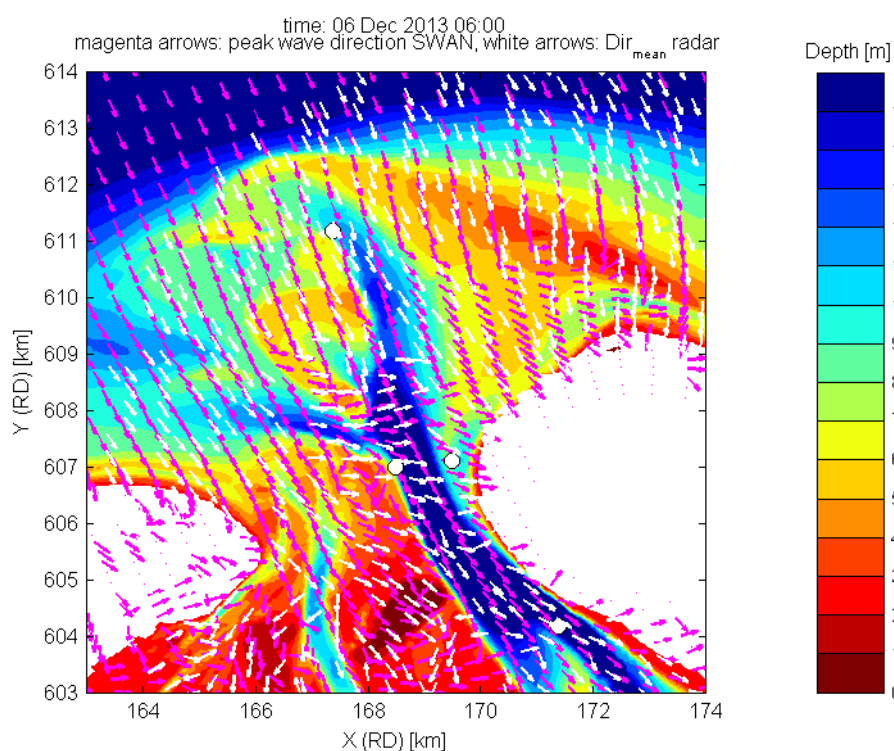
Figure C.9   Spatial distribution of the SWAN peak wave direction (pink arrows), the radar dominant wave directions (white arrows) and total water depth for hindcast moment 6-12-2013 06:00, incident wave direction (SWAN peak wave direction at AZB11): 329 ^{o}N.

Figure C.10 Spatial distribution of the SWAN peak wave direction (pink arrows), the radar dominant wave directions (white arrows)and total water depth for hindcast moment 6-12-2013 08:00, incident wave direction (SWAN peak wave direction at AZB11): 332 ^{o}N.

Figure C.11 Spatial distribution of the SWAN peak wave direction (pink arrows), the radar dominant wave directions (white arrows) and total water depth for hindcast moment 6-12-2013 10:00, incident wave direction (SWAN peak wave direction at AZB11): 331 °N.

Figure C.12 Spatial distribution of the SWAN peak wave direction (pink arrows), the radar dominant wave directions (white arrows) and total water depth for hindcast moment 6-12-2013 13:00, incident wave direction (SWAN peak wave direction at AZB11): 334 °N.

Modelling of wave penetration in complex areas: analysis of hindcast data

Figure C.13 Spatial distribution of the SWAN peak wave direction (pink arrows), the radar dominant wave directions (white arrows) and total water depth for hindcast moment 6-12-2013 15:00, incident wave direction (SWAN peak wave direction at AZB11): 333 °N.

Figure C.14 Spatial distribution of the SWAN peak wave direction (pink arrows), the radar dominant wave directions (white arrows) and total water depth for hindcast moment 6-12-2013 18:00, incident wave direction (SWAN peak wave direction at AZB11): 336 °N.
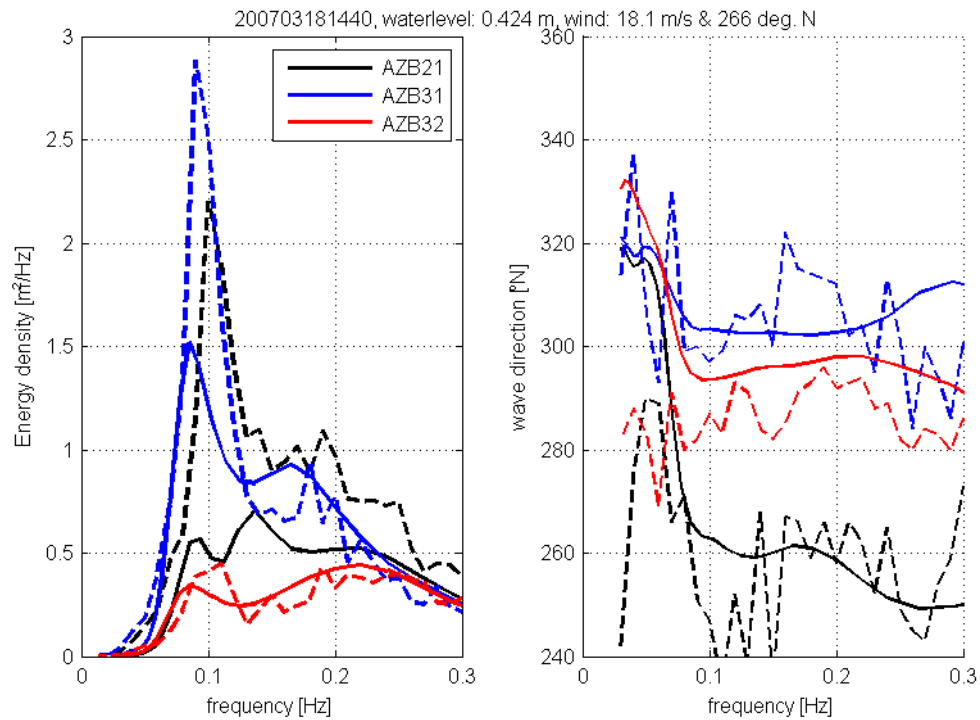
Figure C.15 1D spectrum and wave direction of AZB21, AZB31 and AZB32 for 18-03-2007 14:40, SWAN results are shown with the solid lines, observations with the dashed lines.
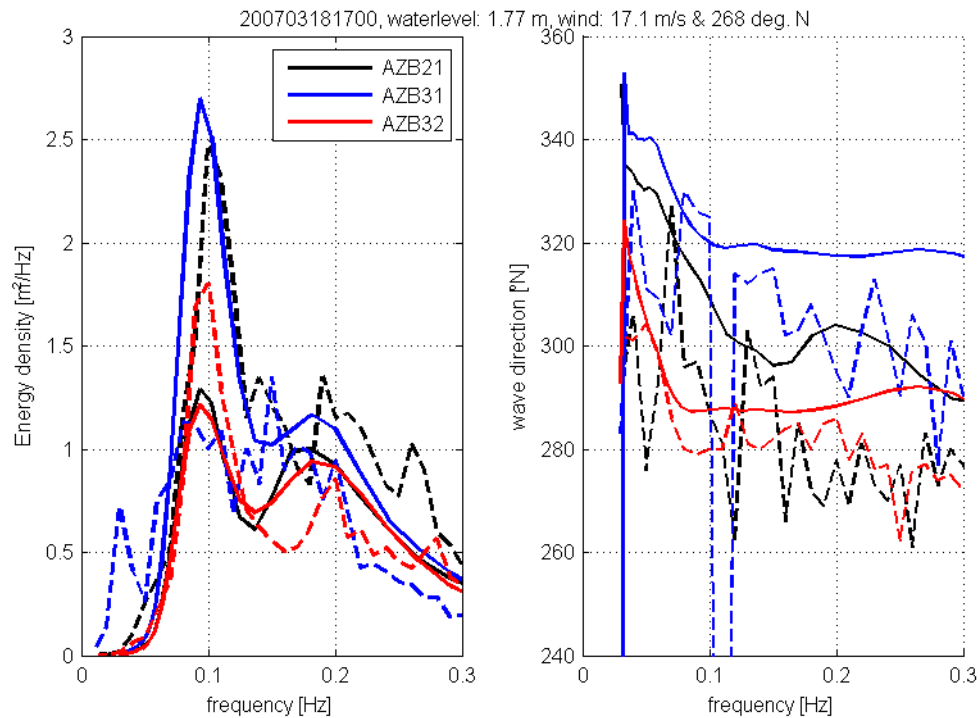
Figure C.16 1D spectrum and wave direction of AZB21, AZB31 and AZB32 for 18-03-2007 17:00, SWAN results are shown with the solid lines, observations with the dashed lines.
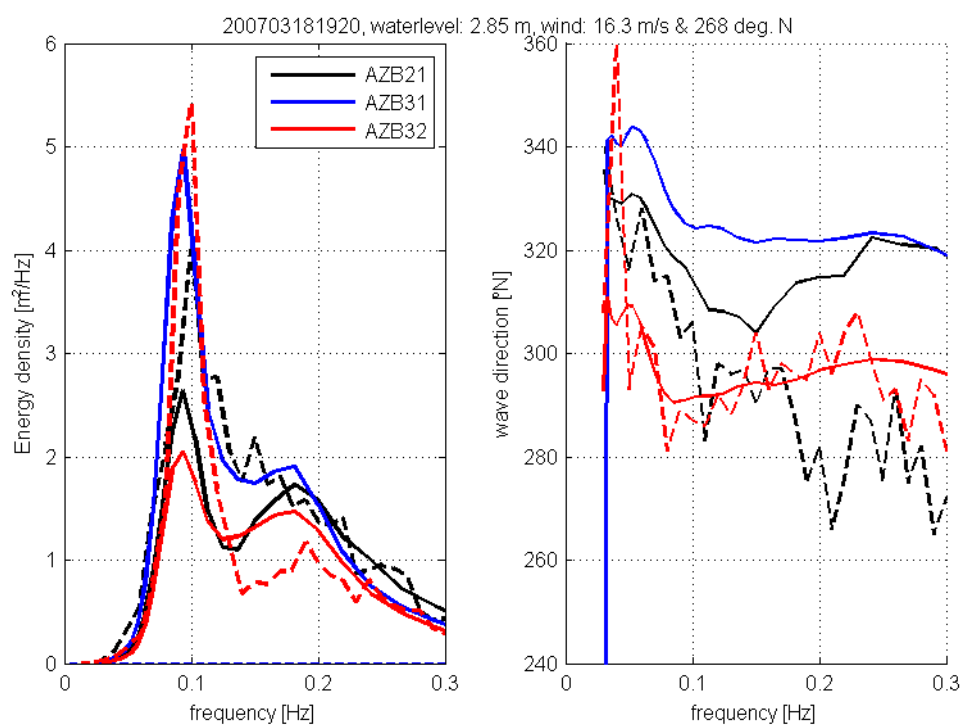
Figure C.17 1D spectrum and wave direction of AZB21, AZB31 and AZB32 for 18-03-2007 19:20, SWAN results are shown with the solid lines, observations with the dashed lines.
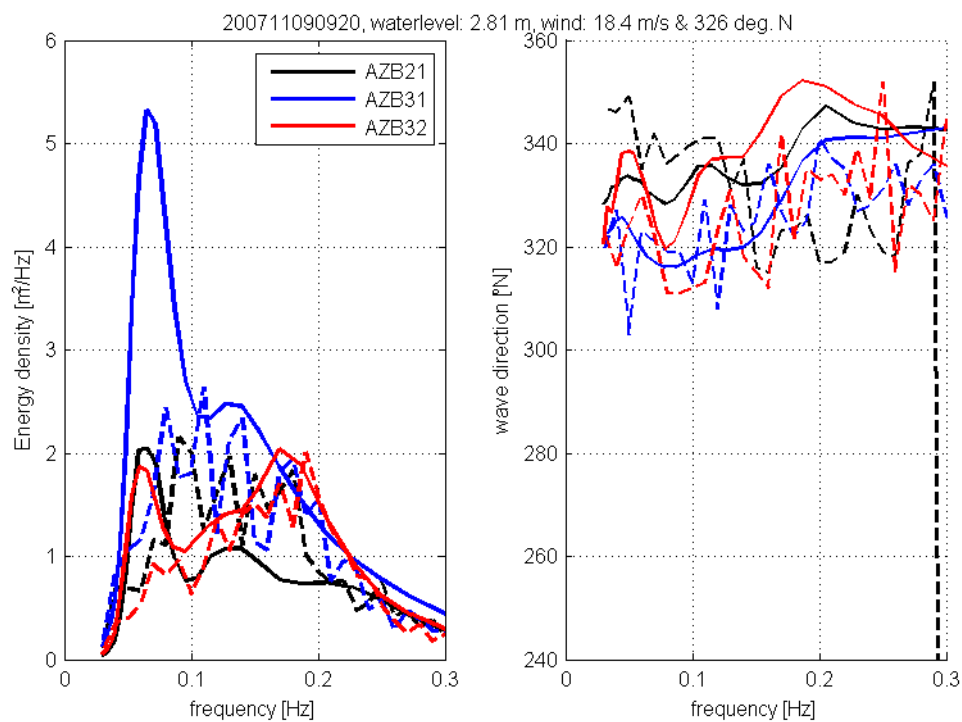
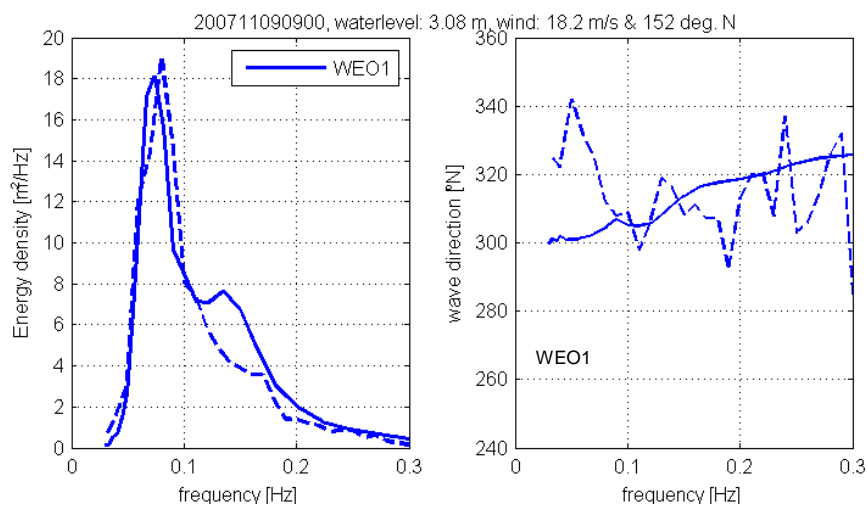*Figure C.18 1D spectrum and wave direction of AZB21, AZB31 and AZB32 for 09-11-2007 9:20, SWAN results are shown with the solid lines, observations with the dashed lines.*
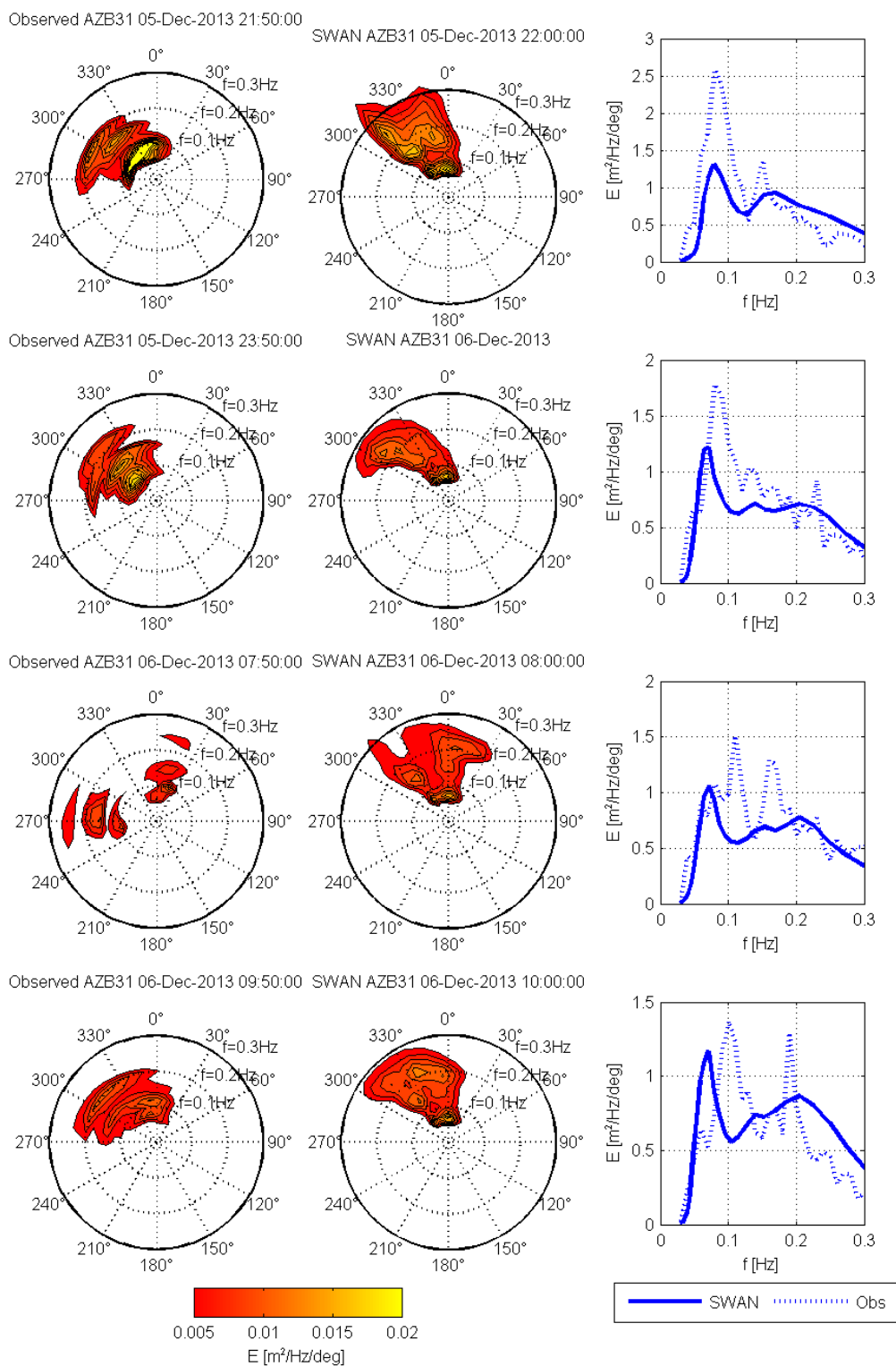
Figure C.19 2D & 1D wave energy density spectra at AZB31 for hindcast moments 1) 5-12-2013 22:00, 2) 6-12-2013 00:00, 3) 6-12-2013 8:00 and 4) 6-12-2013 10:00; first column shows the observed 2D spectrum, second column the SWAN 2D spectrum and third column the 1D spectrum comparison (SWAN solid line, observed dashed line).
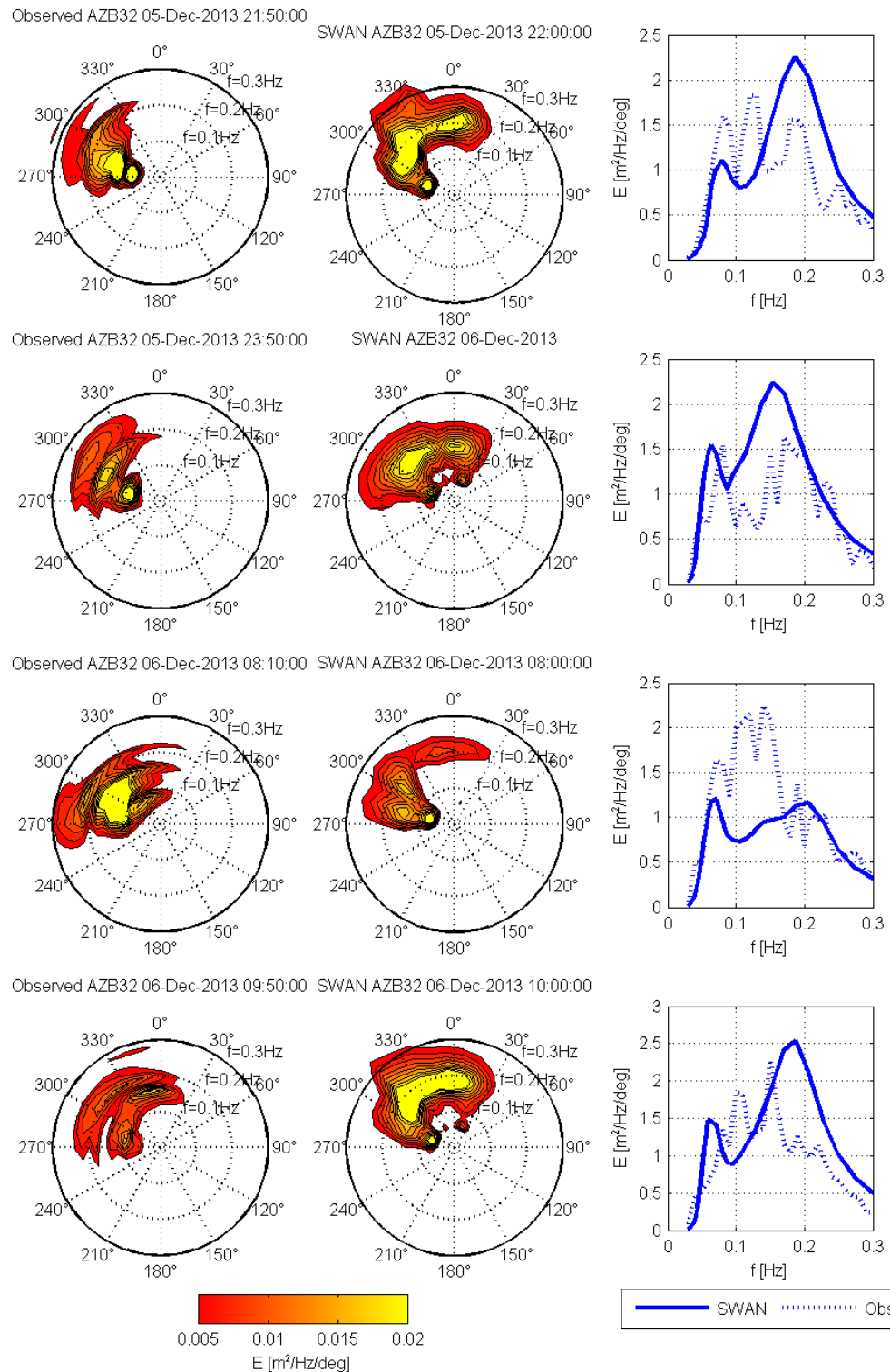
Figure C.20 2D & 1D wave energy density spectra at AZB32 for hindcast moments 1) 5-12-2013 22:00, 2) 6-12-2013 00:00, 3) 6-12-2013 8:00 and 4) 6-12-2013 10:00; first column shows the observed 2D spectrum, second column the SWAN 2D spectrum and third column the 1D spectrum comparison (SWAN solid line, observed dashed line).

D Figures Eastern Wadden Sea
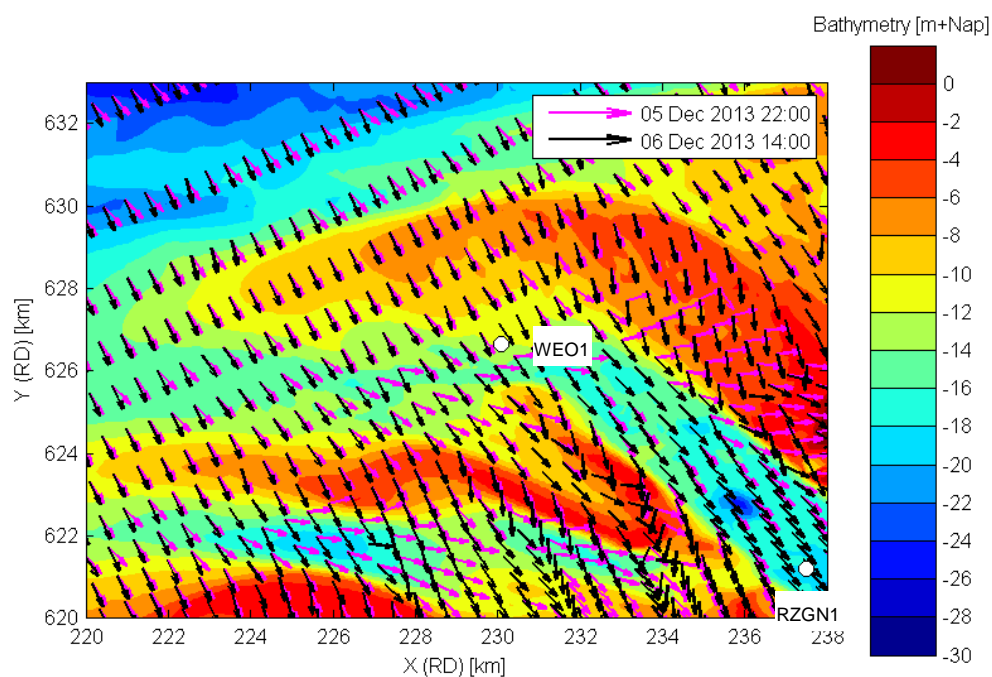
Figure D.1   Spatial distribution of the SWAN peak wave direction and total water depth for hindcast moments 5-12-2013 22:00 (pink arrows) and 6-12-2013 14:00 (black arrows).
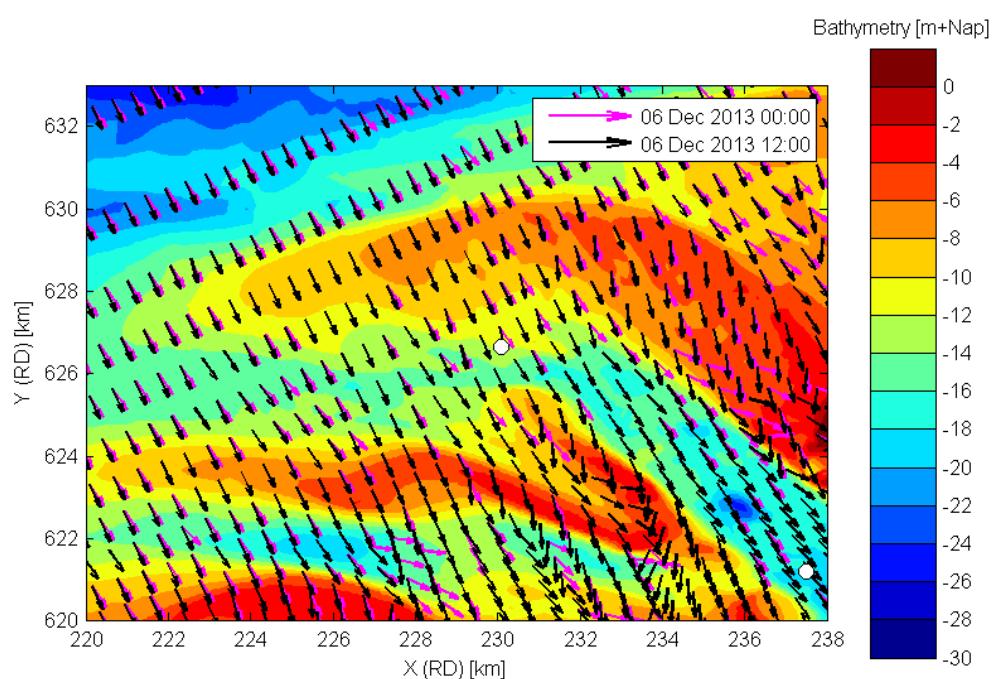
Figure D.2   Spatial distribution of the SWAN peak wave direction (pink arrows) and total water depth for hindcast moments 6-12-2013 00:00 (pink arrows) and 12:00 (black arrows).

Figure D.3   1D spectrum and wave direction of WEO1 for 09-11-2007 9:00, SWAN results are shown with the solid lines, observations with the dashed lines.
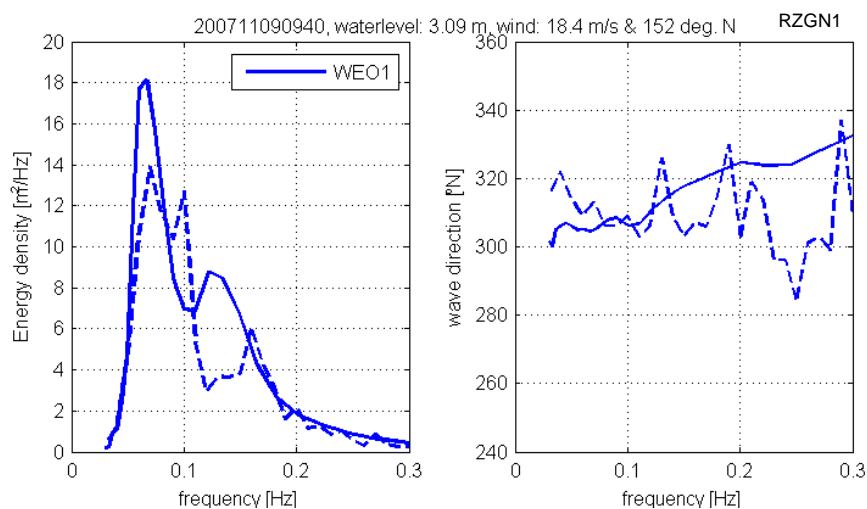
Figure D.4   1D spectrum and wave direction of WEO1 for 09-11-2007 9:40, SWAN results are shown with the solid lines, observations with the dashed lines.
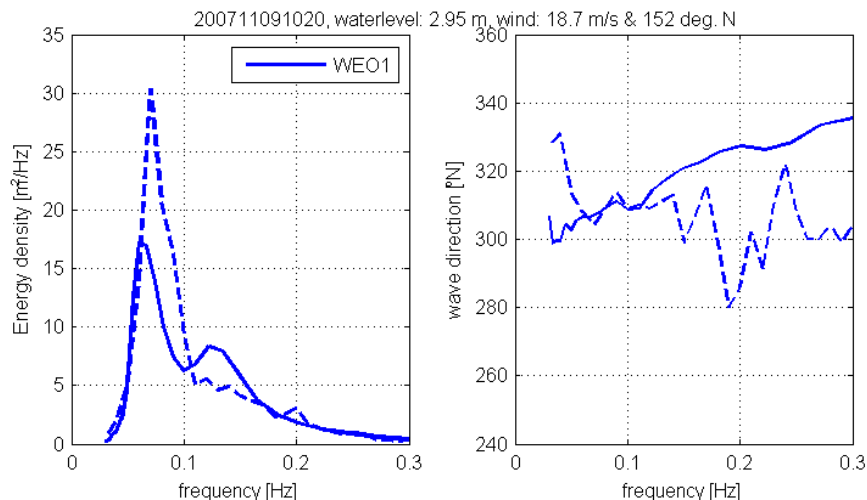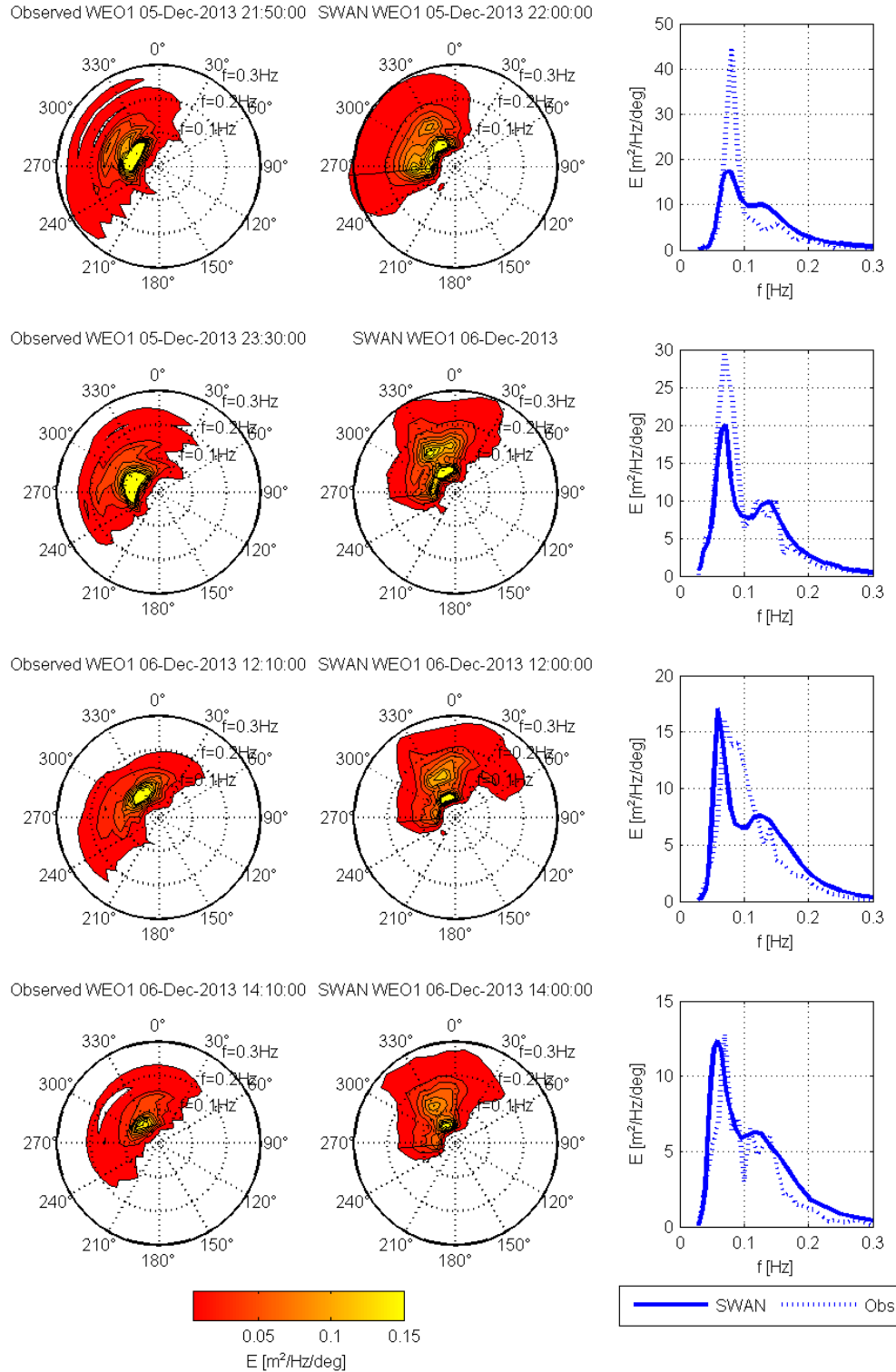

Figure D.5   1D spectrum and wave direction of WEO1 for 09-11-2007 10:20, SWAN results are shown with the solid lines, observations with the dashed lines.

Figure D.6 2D & 1D wave energy density spectra at WEO1 for hindcast moments 1) 5-12-2013 22:00, 2) 6-12-2013 00:00, 3) 6-12-2013 12:00 and 4) 6-12-2013 14:00; first column shows the observed 2D spectrum, second column the SWAN 2D spectrum and third column the 1D spectrum comparison (SWAN solid line, observed dashed line).
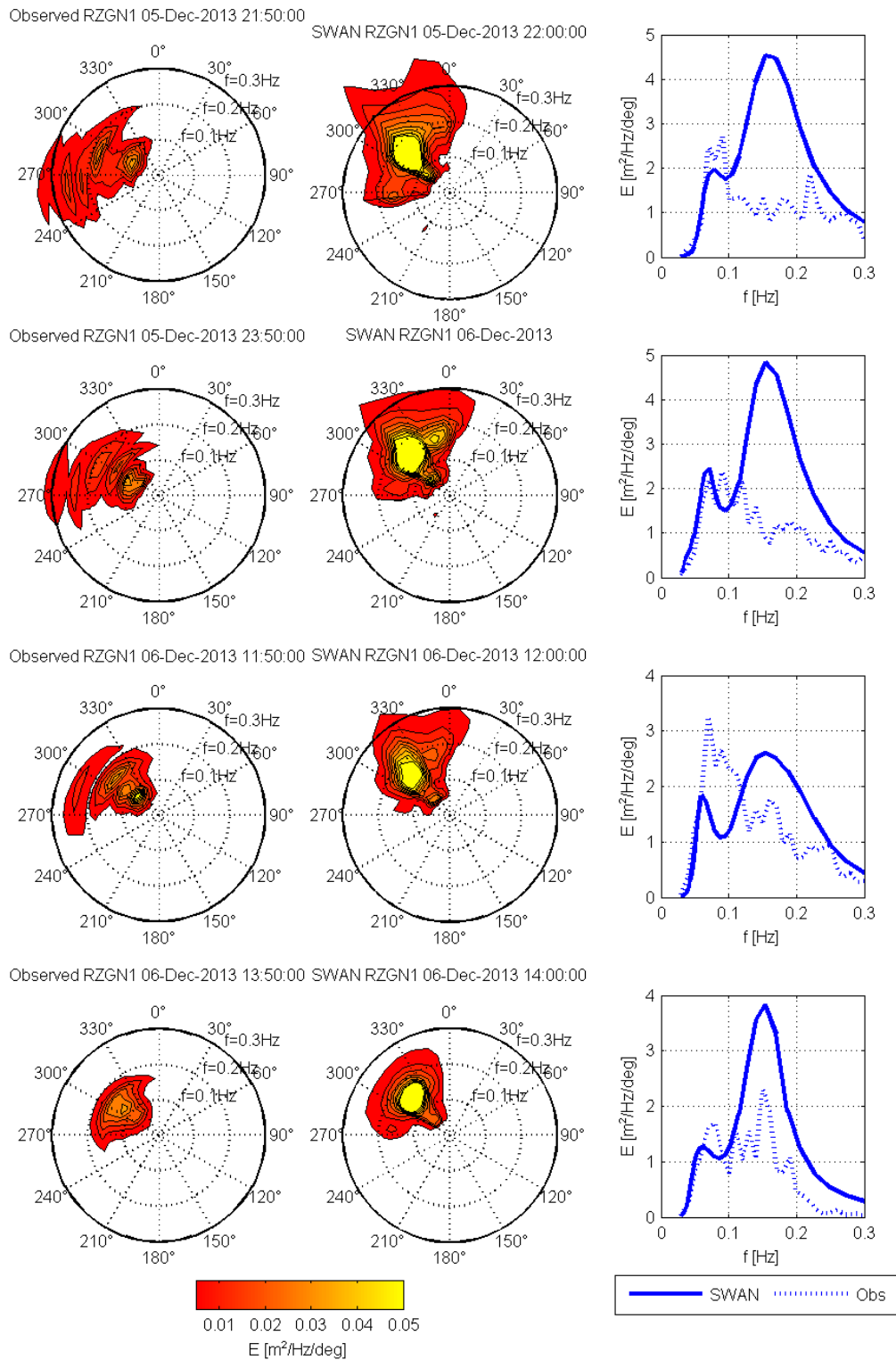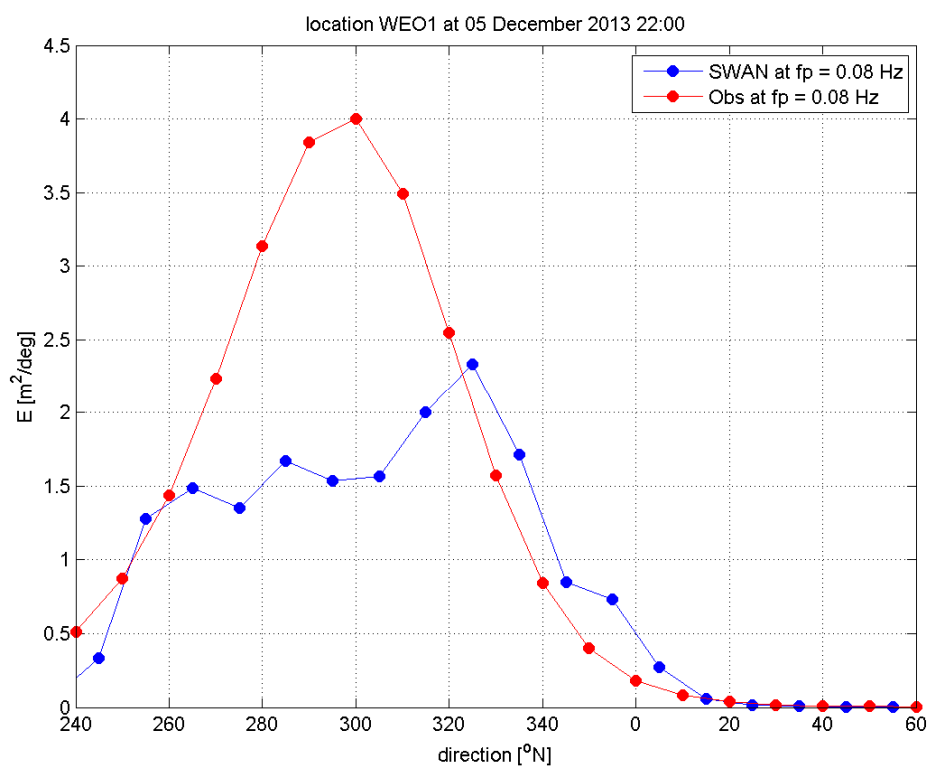
Figure D.7 2D & 1D wave energy density spectra at RZGN1 for hindcast moments 1) 5-12-2013 22:00, 2) 6-12-2013 00:00, 3) 6-12-2013 12:00 and 4) 6-12-2013 14:00; first column shows the observed 2D spectrum, second column the SWAN 2D spectrum and third column the 1D spectrum comparison (SWAN solid line, observed dashed line).

Figure D.8   Directional wave distribution at the low-frequency peak (f_p) for WEO1, hindcast moment 5-12-2013 22:00. SWAN results are shown in blue, observations in red.
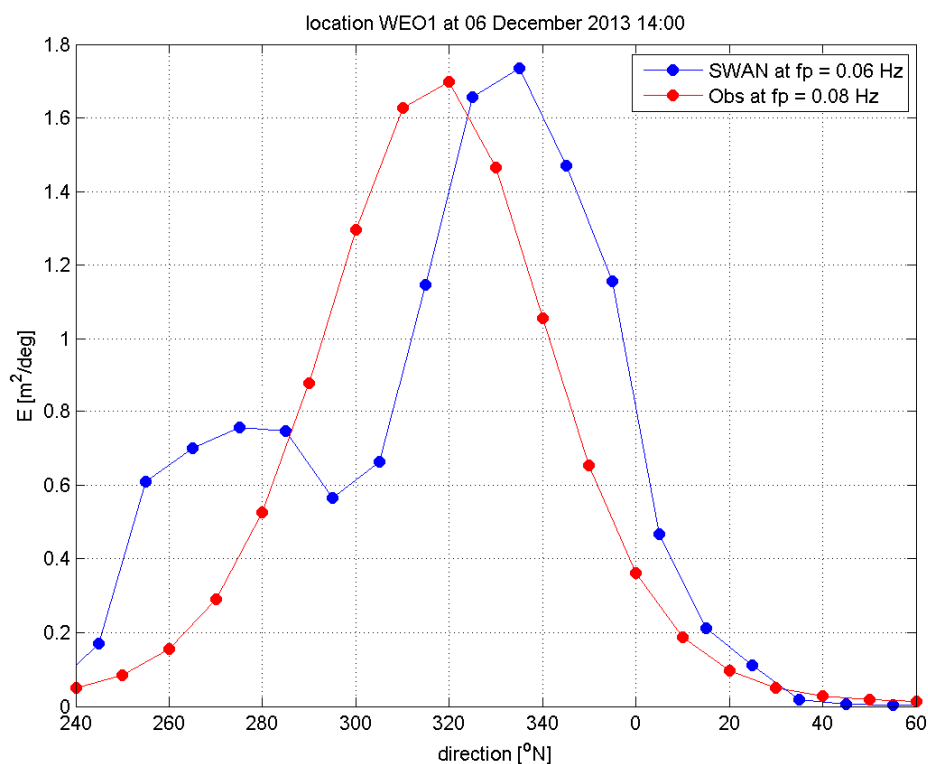

Figure D.9   Directional wave distribution at the low-frequency peak (f_p) for WEO1, hindcast moment 6-12-2013 14:00. SWAN results are shown in blue, observations in red.
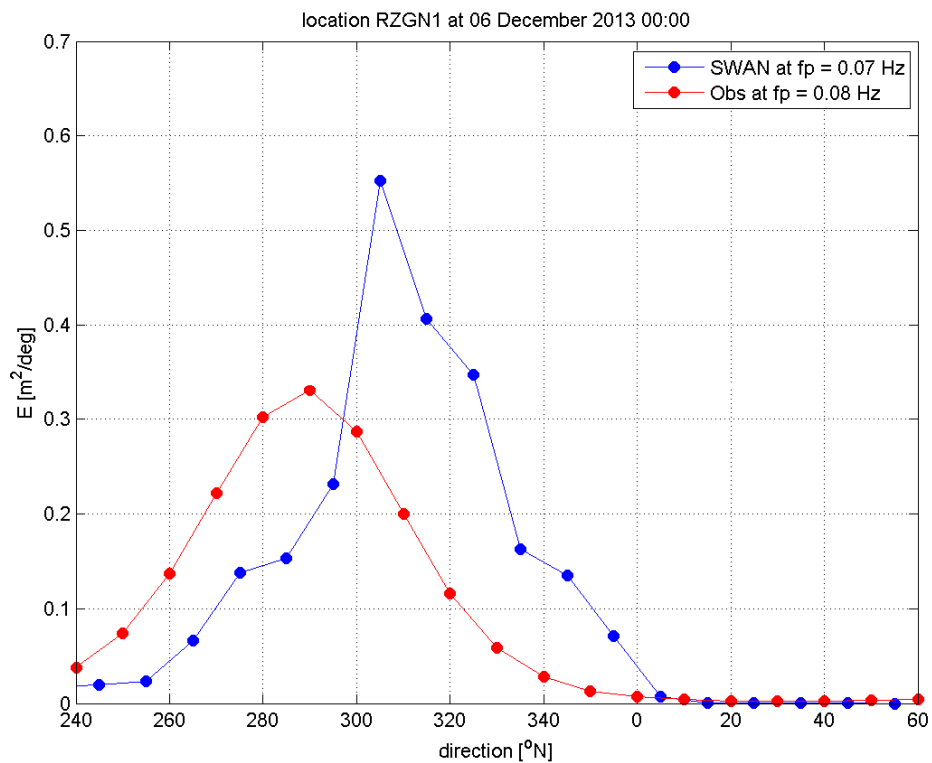
Figure D.10 Directional wave distribution at the low-frequency peak (f_p) for RZGN1, hindcast moment 6-12-2013 00:00. SWAN results are shown in blue, observations in red.
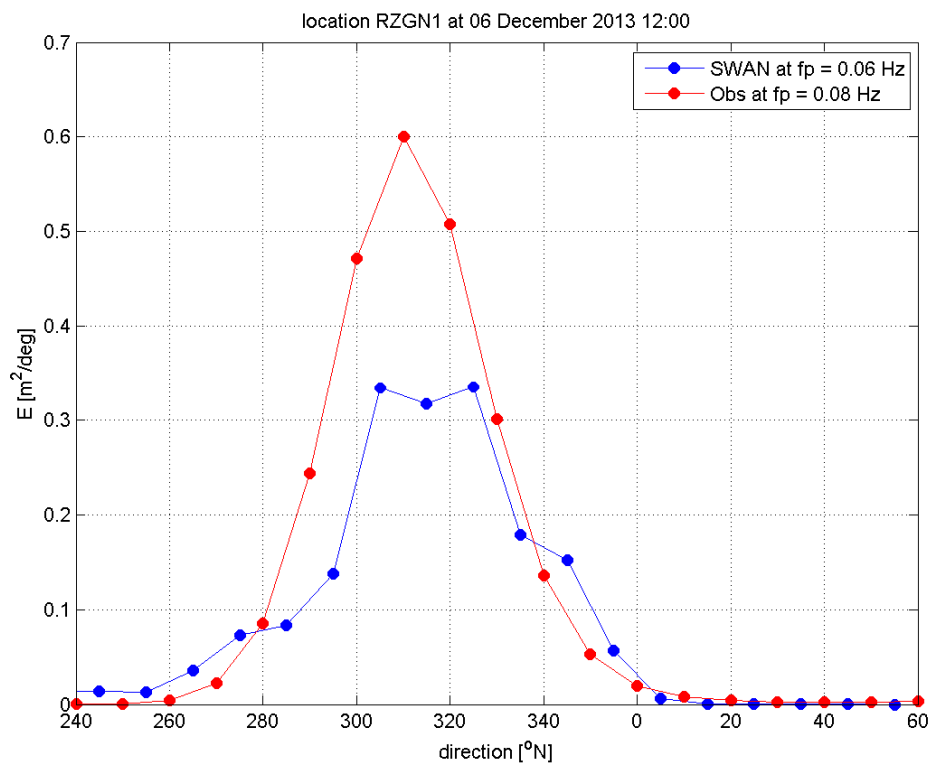

Figure D.11 Directional wave distribution at the low-frequency peak (f_p) for RZGN1, hindcast moment 6-12-2013 12:00. SWAN results are shown in blue, observations in red.